

**Data Acquisition and Data Analysis  
for the Gravitational-Wave Detector GEO 600**

Vom Fachbereich Physik  
der Universität Hannover  
zur Erlangung des Grades

**Doktor der Naturwissenschaften  
– Dr. rer. nat. –**

genehmigte Dissertation von

**Dipl.-Phys. Karsten Kötter**

geboren am 19. Juli 1973 in Hannover

2004

Referent: Prof. K. Danzmann  
Korreferent: Prof. M. Kock  
Tag der Promotion: 9. Februar 2004  
Druckdatum: 13. Februar 2004

## Zusammenfassung

Im frühen 20. Jahrhundert entwickelte Albert Einstein die Allgemeine Relativitätstheorie, die Newtons Beschreibung der Schwerkraft ablöste. Die Allgemeine Relativitätstheorie beschreibt Gravitationseffekte durch eine Krümmung der vierdimensionalen Raum-Zeit und sagt die Existenz von Gravitationswellen voraus. Diese Wellen sind Änderungen in der Geometrie der Raum-Zeit, die sich mit Lichtgeschwindigkeit ausbreiten. Der Gravitationswellendetektor GEO 600 ist Teil der weltweiten Bestrebungen, die erste direkte Messung von Gravitationswellen durchzuführen und damit den Grundstein für Gravitationswellenastronomie zu legen. Es besteht die berechtigte Annahme, dass die Messung der Gravitationswellenabstrahlung astrophysikalischer Quellen neue, faszinierende Einblicke in Astrophysik und Kosmologie geben wird und Informationen liefert, die durch Beobachtungen elektromagnetischer Wellen nicht zugänglich sind.

Diese Arbeit beschreibt die Planung, den Aufbau und die Charakterisierung des Datenerfassungssystems (DAQS) des GEO 600 Detektors. Die Hauptaufgabe dieses Systems ist das Aufzeichnen des Interferometerausgangssignals, das die differenzielle Armlängenänderung angibt. Aus diesen Daten wird der so genannte  $h(t)$ -Kanal erzeugt, der das kalibrierte Gravitationswellensignal enthält. Zusätzlich müssen eine Reihe von Diagnosekanälen und Umgebungsparameter gespeichert werden. Diese Daten ermöglichen es, die Empfindlichkeit des Detektors zu verbessern und Datensegmente auszusondern, in denen der extrem empfindliche  $h(t)$ -Kanal durch externe Störungen beeinflusst wurde. Es müssen hohe Anforderungen an die Datenintegrität, die zeitliche Stabilität des Digitalisierungsvorgangs und die Zuverlässigkeit des Systems erfüllt werden. Die Auswertung des  $h(t)$ -Kanals von GEO 600 gemeinsam mit Daten von anderen Detektoren verlangt, dass die Zeitmarken auf den einzelnen Datenströmen eine Abweichung von höchstens  $10 \mu\text{s}$  haben. Ausfälle oder Funktionsstörungen des DAQS führen zu einem Verlust von Betriebszeit des gesamten Detektors. Deshalb muss das DAQS zuverlässig und unterbrechungsfrei über Zeiträume von mehreren Wochen laufen. Erfahrungen der ersten Datenläufe zeigen, dass über mehr als 99% der Gesamtzeit erfolgreich Daten aufgezeichnet werden konnten.

Im zweiten Teil der Arbeit werden Analyseergebnisse der ersten von GEO 600 gelieferten wissenschaftlichen Daten gezeigt. Eine Methode wird präsentiert, die im  $h(t)$ -Kanal nach Transienten sucht, wie sie z. B. durch die Gravitationswellenabstrahlung während einer Supernova erwartet werden. Diese Methode kann durch externe Störungen verursachte Transienten erkennen und so die Zahl der weiter zu untersuchenden Ereignisse verringern. Im Gegensatz zu anderen Algorithmen erfordert die vorgestellte Methode keine Daten von Umgebungssensoren. Stattdessen wird die Verteilung der Signalleistung in den zwei Quadraturen des Interferometerausgangssignals gemessen und mit dem Wert verglichen, der für eine differenzielle Armlängenänderung erwartet wird.

Zusätzlich wurde die Genauigkeit der Zeitmarken auf den Daten des S1 Laufs analysiert. Mit Hilfe einer Monte-Carlo-Simulation wurde bestimmt, wie sich die gemessene Fluktuation der Zeitmarken auf die Bestimmung der Ankunftsrichtung eines Signals auswirkt, das von einem weltweiten Netzwerk bestehend aus vier bzw. sechs Detektoren registriert wird.

**Stichworte:** Gravitationswellendetektor, Datenerfassung, Datenanalyse



## Abstract

In the early 20<sup>th</sup> century Albert Einstein developed the theory of general relativity which superseded Newton's description of gravity. General relativity describes gravitational effects by a curvature of the four-dimensional space-time and predicts the existence of gravitational waves which are ripples in space-time propagating at the speed of light

The gravitational-wave detector GEO 600 is part of the worldwide effort to make the first direct measurement of gravitational waves and to lay the foundations for the field of gravitational wave astronomy. This involves mastering extreme technical challenges. Measuring gravitational waves emitted by astrophysical objects is expected to give fascinating new insights into astrophysics and cosmology by revealing information that is inaccessible to electro-magnetic observations.

This work describes the design, construction and testing of the GEO 600 data acquisition system (DAQS). The main task of this system is to record the data required to generate the  $h(t)$  channel. This channel contains the gravitational wave information measured by the GEO 600 instrument. In addition a number of diagnostic channels and environmental parameters need to be recorded. These data allows the performance of the detector to be monitored and gives us the possibility to veto data segments where the extremely sensitive  $h(t)$  channel was affected by external disturbances. The DAQS has to fulfill strict requirements in terms of data integrity and timing accuracy of the acquisition process. Merging the data set recorded at the GEO 600 site with data from other detectors demands that the individual data streams are time stamped to an accuracy of better than 10  $\mu$ s. Since the uptime of the DAQS limits the duty cycle of the whole instrument, the system needs to be highly reliable. The first data runs over periods of several weeks showed that the DAQS can work with a duty cycle above 99%.

In the second part of this work, data analysis results from the first scientific data recorded by GEO 600 are shown. A vetoing scheme for burst events seen in the  $h(t)$  channel is presented that can reduce the number of candidate events significantly. Unlike most other vetoing schemes the method does not require any environmental data. Instead the power distribution in the two quadratures of the interferometer output signal is measured and compared to the value expected for a differential arm length change as it would be caused by a gravitational wave.

In addition the timing accuracy of the DAQS during the first science run, S1, was analyzed. The effect of the measured timing jitter on the determination of the direction of arrival of a burst signal using time of arrival information from a world-wide network of detectors was estimated.

**Keywords:** gravitational-wave detector, data acquisition, data analysis



# Contents

<b>Zusammenfassung</b>	<b>i</b>
<b>Abstract</b>	<b>iii</b>
<b>Contents</b>	<b>v</b>
<b>List of figures</b>	<b>ix</b>
<b>List of tables</b>	<b>xiii</b>
<b>Glossary</b>	<b>xv</b>
<b>1. Gravitational Wave Detection</b>	<b>1</b>
1.1. Gravitational waves . . . . .	1
1.1.1. Introduction . . . . .	1
1.1.2. Theory . . . . .	2
1.1.3. Sources of gravitational waves and their detection . . . . .	5
1.1.3.1. Supernovae . . . . .	5
1.1.3.2. Inspiral binary systems . . . . .	6
1.1.3.3. Pulsars . . . . .	6
1.1.3.4. Stochastic gravitational wave background . . . . .	7
1.2. The gravitational-wave detector GEO 600 . . . . .	8
1.2.1. Overview . . . . .	8
1.2.2. Optical configuration . . . . .	8
1.2.3. Laser system . . . . .	9
1.2.4. Mode-cleaners . . . . .	9
1.2.5. Interferometer . . . . .	10
1.2.6. Environmental monitors . . . . .	11
<b>2. The Data Acquisition System of GEO 600</b>	<b>15</b>
2.1. Requirements . . . . .	15
2.1.1. Analog to digital conversion process . . . . .	16
2.1.1.1. Quantization noise . . . . .	16
2.1.1.2. Sampling rate . . . . .	17
2.1.2. Timing accuracy . . . . .	19
2.1.3. Data rate . . . . .	19

2.2.	System design . . . . .	19
2.2.1.	Overview . . . . .	19
2.2.2.	Acquiring the data . . . . .	21
2.2.2.1.	Data Collecting Units (DCUs) . . . . .	21
2.2.2.2.	LabVIEW system, ctrl_to_daq-VI . . . . .	27
2.2.3.	Processing the data . . . . .	27
2.2.4.	Automated monitoring . . . . .	29
2.2.5.	Configuring the system . . . . .	30
2.2.6.	Data format and storage . . . . .	32
2.2.7.	Data access . . . . .	33
2.2.7.1.	Raw data / LabVIEW oscilloscope-VI . . . . .	33
2.2.7.2.	Local frame files . . . . .	33
2.2.7.3.	Frame server . . . . .	34
2.2.7.4.	Accessing data in Matlab . . . . .	34
2.2.7.5.	DataViewer . . . . .	35
2.3.	Measurements . . . . .	37
2.3.1.	Timing accuracy of the sampling process . . . . .	37
2.3.1.1.	Checking the GPS second labels on the data segments . . . . .	37
2.3.1.2.	Measuring the residual offset and jitter against an external time reference . . . . .	38
2.3.1.3.	Timing across reboots . . . . .	40
2.3.1.4.	GPS frequency lock servo . . . . .	41
2.3.2.	Filtering . . . . .	42
2.3.3.	Noise level . . . . .	42
<b>3.</b>	<b>Data Analysis</b>	<b>47</b>
3.1.	Data runs . . . . .	47
3.1.1.	Engineering run 7 (E7) . . . . .	47
3.1.2.	Science run 1 (S1) . . . . .	47
3.1.2.1.	S1 timing accuracy . . . . .	48
3.2.	Angular resolution of a worldwide gravitational-wave detector network . . . . .	52
3.2.1.	Introduction . . . . .	52
3.2.2.	Theory . . . . .	52
3.2.3.	The algorithm . . . . .	54
3.2.4.	Results . . . . .	55
3.3.	Vetoing burst events with <i>PQMon</i> . . . . .	59
3.3.1.	Introduction . . . . .	59
3.3.2.	Vetoing burst events using <i>PQMon</i> . . . . .	59
3.3.2.1.	Concept of the <i>PQMon</i> algorithm . . . . .	59
3.3.2.2.	Transient detection . . . . .	60
3.3.2.3.	Measuring the power ratio $P_b/Q_b$ of a candidate burst event . . . . .	61
3.3.2.4.	Measuring the calibration line ratio $P_c/Q_c$ . . . . .	62
3.3.2.5.	Verifying the statistics . . . . .	64
3.3.3.	Results . . . . .	67
3.3.4.	Summary . . . . .	69



<b>A. The optical layout of GEO 600</b>	<b>71</b>
<b>B. Quantization noise</b>	<b>73</b>
<b>C. Digital filtering</b>	<b>75</b>
C.1. Frequency domain filtering . . . . .	75
C.2. Time domain filtering . . . . .	76
C.2.1. Finite Impulse Response (FIR) Filter . . . . .	78
C.2.2. Infinite Impulse Response (IIR) Filter . . . . .	78
<b>D. Active vibration-isolation</b>	<b>83</b>
<b>Bibliography</b>	<b>87</b>
<b>Acknowledgments</b>	<b>91</b>
<b>Curriculum vitae</b>	<b>93</b>
<b>Publications</b>	<b>95</b>



# List of figures

1.1. A gravitational wave affects the distance between test masses . . . . .	3
1.2. Detecting gravitational waves using a Michelson interferometer . . . . .	4
1.3. Optical configuration of GEO 600 . . . . .	9
1.4. Suspension of the interferometer optics . . . . .	11
1.5. Design sensitivity of GEO 600 . . . . .	12
1.6. Seismometer data measured during earthquake near Tuvalu . . . . .	12
1.7. Location of the environmental sensors . . . . .	13
2.1. Dynamic range limit due to amplitude quantization . . . . .	16
2.2. Pre-whitening . . . . .	17
2.3. Sampling in the time domain . . . . .	18
2.4. Adding frequency components due to aliasing . . . . .	18
2.5. Hardware setup of the GEO 600 DAQS . . . . .	20
2.6. Data flow in the GEO 600 DAQS . . . . .	22
2.7. Schematic of a Data Collecting Unit (DCU) . . . . .	23
2.8. Schematic of the <i>ICS110B</i> ADC board . . . . .	23
2.9. Schematic of the timing signals . . . . .	26
2.10. Timing signals measured on the GEO 600 DAQS . . . . .	26
2.11. <i>LabVIEW</i> virtual instrument <i>ctrl_to_daq</i> . . . . .	28
2.12. Schematic of the diagnostics system . . . . .	29
2.13. HTTP interface for configuring the DAQS . . . . .	31
2.14. <i>LabVIEW</i> <i>oscilloscope</i> virtual instrument . . . . .	34
2.15. Schematic of the <i>DataViewer</i> . . . . .	35
2.16. Screen shot of a plot generated with the <i>DataViewer</i> . . . . .	36
2.17. Test signal for checking the GPS second labels on the data . . . . .	37
2.18. Comparison of external Rb/GPS clock and the DAQS GPS clock . . . . .	38
2.19. Ramp signal for testing the DAQS timing accuracy . . . . .	38
2.20. Setup for determining the DAQS timing accuracy . . . . .	39
2.21. 24 h test of DAQS timing . . . . .	39
2.22. Histogram of the timing offsets taken over 24 hours . . . . .	39
2.23. Ramp signals produced by <i>HP33120A</i> signal generator . . . . .	40
2.24. Systematic offset of the timing test signal . . . . .	40
2.25. Mean timing offset versus injected ramp length . . . . .	41
2.26. Standard deviation of timing offset versus length of the ramp signal . . . . .	41
2.27. Timing residuals during hardware and software reboots of the DAQS . . . . .	42
2.28. Settling of the timing signal after a power cycle . . . . .	42

2.29. Anti-aliasing filter for decimating the data to 8192 Hz . . . . .	43
2.30. Anti-aliasing filter for decimating the data to 2048 Hz . . . . .	43
2.31. Anti-aliasing filter for decimating the data to 512 Hz . . . . .	43
2.32. Anti-aliasing filter for decimating the data to 4096 Hz . . . . .	43
2.33. Anti-aliasing filter for decimating the data to 1024 Hz . . . . .	43
2.34. Anti-aliasing filter for decimating the data to 256 Hz . . . . .	43
2.35. Anti-aliasing filter for decimating the data to 128 Hz . . . . .	44
2.36. Anti-aliasing filter for decimating the data to 64 Hz . . . . .	44
2.37. Checking the signal used to measure the noise floor . . . . .	45
2.38. Noise floor of <i>ICS110B</i> ADC using different pre-amplifier settings . . . . .	45
2.39. Noise floor of <i>VMIC</i> ADC . . . . .	46
3.1. Duty cycle of the GEO 600 detector during the S1 run . . . . .	48
3.2. Sensitivity Curve of GEO 600 during the S1 run. . . . .	49
3.3. Time-frequency plot of the $h(t)$ -channel during the S1 run. . . . .	49
3.4. Calibration signal used for the timing check of S1 data . . . . .	50
3.5. Timing residuals during the whole S1 run . . . . .	50
3.6. Close-up view of timing data when the system was in faulty state . . . . .	51
3.7. The effect of the phase-locking servo of the GPS card . . . . .	51
3.8. Timing residuals when DAQ system was in good state . . . . .	51
3.9. Calculating the direction of arrival from the time of arrival . . . . .	53
3.10. Direction of arrival reconstruction using data from 3 detectors . . . . .	54
3.11. Direction dependence of the error . . . . .	55
3.12. Direction dependence of the error . . . . .	55
3.13. Direction of arrival error estimation, 4 detectors, $\sigma = 63$ ns . . . . .	57
3.14. Direction of arrival error estimation, 6 detectors, $\sigma = 63$ ns . . . . .	57
3.15. Direction of arrival error estimation, 4 detectors, $\sigma = 6.3$ $\mu$ s . . . . .	58
3.16. Direction of arrival error estimation, 6 detectors, $\sigma = 6.3$ $\mu$ s . . . . .	58
3.17. In-phase and quadrature channels of GEO 600 . . . . .	60
3.18. Time domain windows used for the transient detection algorithm . . . . .	61
3.19. Measuring the noise floor and the calibration line signal . . . . .	63
3.20. Verifying the power and variance estimation method for a transient . . . . .	66
3.21. Verifying the power and variance estimation method for a calibration line . . . . .	66
3.22. Time evolution of the relative sensitivity $P_c/Q_c$ during the S1 run . . . . .	67
3.23. Distribution of transients during the S1 run . . . . .	68
3.24. Histogram of candidate burst events before and after the veto process . . . . .	68
3.25. Example of a vetoed event . . . . .	68
3.26. Example of a non-vetoed event . . . . .	68
A.1. Detailed GEO 600 optical layout . . . . .	72
B.1. Amplitude rounding in quantization process. . . . .	74
C.1. 6 <sup>th</sup> order Butterworth filter with cutoff frequency of $\omega = 1$ . . . . .	80
C.2. Comparison: Analog filter against digital filter from bilinear transform . . . . .	81

D.1. Schematic of the feedforward control system . . . . .	84
D.2. Plot of transfer function. . . . .	84
D.3. Schematic of the <i>MARK</i> geophone sensor . . . . .	85
D.4. Schematic of the piezo actuator . . . . .	85
D.5. Setup of the active vibration-isolation system . . . . .	86
D.6. Results obtained with the feedforward active vibration-isolation system . . . . .	86



## List of tables

3.1. Geographical location of gravitational-wave detectors . . . . .	56
C.1. Coefficients for 6 <sup>th</sup> Butterworth filter . . . . .	80
D.1. Transfer function used for feedforward system . . . . .	84





# Glossary

1PPS	One Pulse Per Second
ADC	Analog to Digital Converter
ASD	Amplitude Spectral Density
DAQ	Data Acquisition
DAQS	Data Acquisition System
DBMS	Database Management System
DCU	Data Collecting Unit
DFT	Discrete Fourier Transform
FIFO	First In, First Out
FTP	File Transfer Protocol
GPS	Global Positioning System
HTML	HyperText Markup Language
HTTP	HyperText Transport Protocol
IP	Internet Protocol
LabVIEW	Laboratory Virtual Instrument Engineering Workbench
lsb	least significant bit
PHP	PHP Hypertext Preprocessor
PSD	Power Spectral Density
RAID	Redundant Array of Inexpensive Disks
rms	root mean square
SNR	Signal-to-Noise Ratio
SQL	Structured Query Language
TCP	Transmission Control Protocol
TTL	Transistor-Transistor Logic
UPS	Uninterruptible Power Supply
UTC	Universal Coordinated Time
VI	Virtual Instrument (created in LabVIEW)
VME	VersaModule Eurocard
WGS	World Geodetic System



# Chapter 1.

## Gravitational Wave Detection

### 1.1. Gravitational waves

#### 1.1.1. Introduction

The existence of gravitational waves was first predicted by Albert Einstein in 1916. According to the linearized equations of Einstein's theory of general relativity, accelerated masses cause ripples in the space-time curvature that propagate at a finite speed. In 1957 it was inevitably proven by Bondi that these wave solutions of the mathematical equations are not only an artifact of the theory of general relativity but that the waves carry energy and thus can in principle be measured.

An indirect measurement of gravitational wave emission has already been successfully performed. Russell A. Hulse and Joseph H. Taylor monitored the orbital period of the binary pulsar PSR1913+16 [56]. By emitting gravitational wave radiation the system dissipates energy which leads to a decrease in the orbital period. After accounting for all other known effects that influence the orbital period the residual spin up rate on PSR1913+16 deviates by less than 0.5% from the expected value due to gravitational wave emission. For their work Hulse and Taylor were awarded the 1993 Nobel price.

However to date no direct measurement of gravitational wave radiation has been successful. This is due to the extreme technical challenges involved in measuring the miniscule effect of the waves. In any source of detectable gravitational wave radiation very large accelerations have to act on massive objects. This makes it infeasible to generate gravitational waves in the laboratory. By far the strongest contribution to the gravitational wave radiation present on earth is expected to originate from astrophysical sources like supernovae. But even for the strongest of these sources the resulting distortion of the space-time curvature is so small that the resulting change in distance between two points is only one part in  $10^{21}$ .

Efforts to detect gravitational waves were started in the 1960s. Joseph Weber designed the first gravitational wave bar detector. The basic concept is still used today in detectors like Allegro [41], AURIGA [17], EXPLORER [10] and NAUTILUS [11]: A gravitational wave passing through such a detector deposits energy into the resonance of a large metal cylinder contained in the apparatus and thereby excites the resonance. This can be detected by monitoring the vibrational motion of the cylinder using a low noise transducer.

In the 1970s a new concept for gravitational-wave detectors emerged: A Michelson type laser interferometer measuring the differential length of two perpendicular arms is sensitive to space-time distortions and can thus be used to detect gravitational waves. The arm length of these detectors needs to be in the kilometer scale in order to have a chance of making a detection. With GEO 600[19, 20, 58, 34] , LIGO [6, 51], VIRGO [14, 21] and TAMA [9] a number of gravitational wave laser interferometers with a promising sensitivity are available or will be in the near future. These instruments have a chance of making the first direct measurement of gravitational wave radiation.

### 1.1.2. Theory

The theory of general relativity describes the effects of gravitation by introducing a curved four-dimensional space-time. The curvature of the space-time determines the motion of masses. At the same time the mass distribution governs the curvature of the space-time.

The mass and energy distribution is described by the stress-energy tensor  $T_{\mu\nu}$  while the curvature of space-time is specified by the Einstein curvature tensor  $G_{\mu\nu}$ .

The fundamental relation between  $G_{\mu\nu}$  and  $T_{\mu\nu}$  is given by

$$T_{\mu\nu} = \frac{c^4}{8\pi G} G_{\mu\nu} \quad (1.1)$$

where  $c$  is the speed of light and  $G$  the gravitational constant.

The curvature can locally be described by the metric tensor  $g_{\mu\nu}$ . In the absence of energy the space-time is flat so that  $g_{\mu\nu}$  is given by the Minkowski metric

$$\eta_{\mu\nu} = \begin{pmatrix} -1 & 0 & 0 & 0 \\ 0 & 1 & 0 & 0 \\ 0 & 0 & 1 & 0 \\ 0 & 0 & 0 & 1 \end{pmatrix}. \quad (1.2)$$

In the weak field limit of small curvature the metric tensor can be written as a small deviation  $h_{\mu\nu}$  from the flat metric  $\eta_{\mu\nu}$ :

$$g_{\mu\nu} = \eta_{\mu\nu} + h_{\mu\nu} \quad (1.3)$$

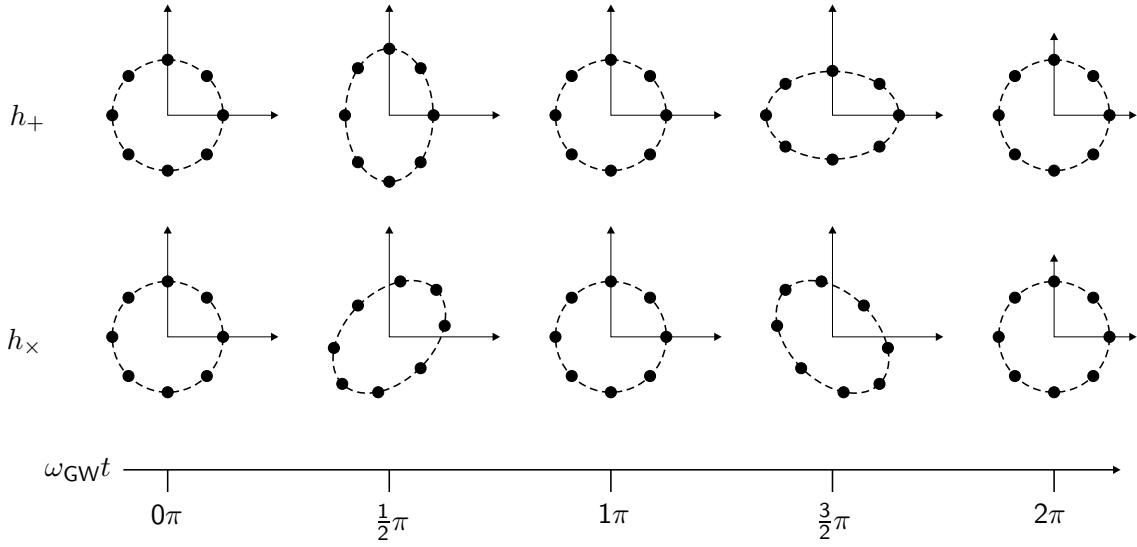


Figure 1.1.: A gravitational wave affects the distance between free falling test masses.

Using the *transverse traceless gauge* [42]  $h_{\mu\nu}$  has the form

$$h_{\mu\nu} = \begin{pmatrix} 0 & 0 & 0 & 0 \\ 0 & h_+ & h_\times & 0 \\ 0 & h_\times & -h_+ & 0 \\ 0 & 0 & 0 & 0 \end{pmatrix}. \quad (1.4)$$

The parameters  $h_+$  and  $h_\times$  represent the two polarization states of a gravitational wave. A gravitational wave at the angular frequency  $\omega_{\text{gw}}$  will give an oscillating contribution for  $h_+ = h_a \exp(\omega_{\text{gw}}t)$  and  $h_\times = h_b \exp(\omega_{\text{gw}}t)$ .

Gravitational waves do not contain moments lower than the quadrupole moment. Conservation laws for energy, momentum and angular momentum forbid the generation of gravitational wave monopole and dipole radiation [48]. The effect of a gravitational wave passing through a ring of test masses can be seen in figure 1.1 for the two polarizations. These test masses are free falling, i.e. no forces are exerted on them.

The changes in the distance between the test masses can be detected using a Michelson interferometer (see figure 1.2): At the input port laser light is sent to a beam splitter. The two emerging beams run along the two perpendicular arms, are reflected by the end mirrors and recombined at the beam splitter. At the output port the arm length difference can be measured by monitoring the interfering light fields coming from the two arms. A gravitational wave changes the optical path length of the arms and thus influences the output signal. In this setup the test masses need to be free falling only in the direction along the laser beam line. Thus the experiment can be carried out in a laboratory on earth using masses that are suspended as a pendulum.

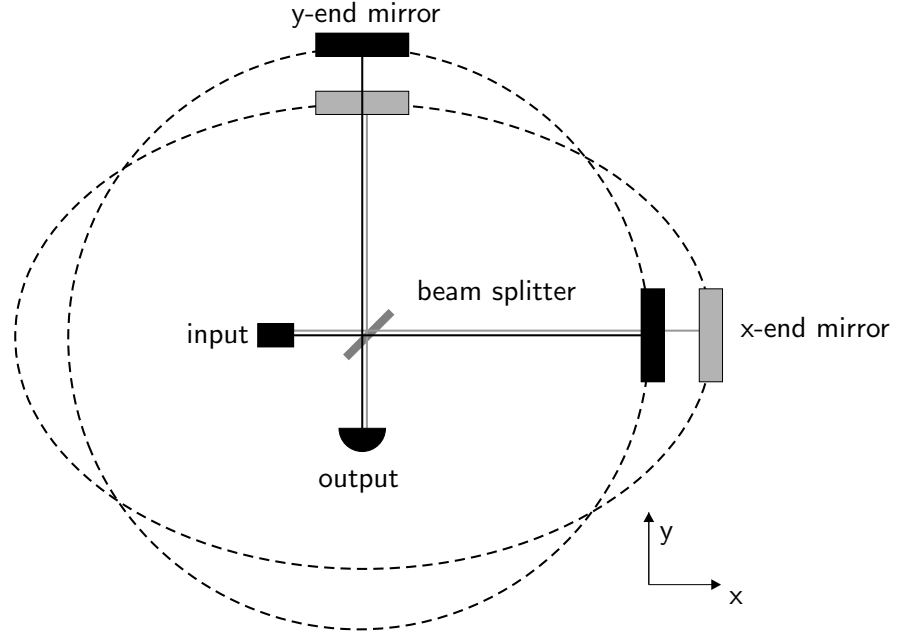


Figure 1.2.: Gravitational waves can be detected by measuring the differential arm length of a Michelson interferometer.

The effect of a gravitational wave on the output signal of an interferometer can be calculated by tracing the space-time intervals  $ds^2 = g_{\mu\nu}dx^\mu dx^\nu$  along the light path from the beam splitter to the end mirrors [48]. General relativity states that space-time coordinates along the propagation line of a light beam in vacuum are connected by space-time intervals  $ds$  of zero:

$$\begin{aligned} ds^2 &= g_{\mu\nu}dx^\mu dx^\nu = 0 \\ &= (\eta_{\mu\nu} + h_{\mu\nu}) dx^\mu dx^\nu \end{aligned} \quad (1.5)$$

The light travel times are obtained by integrating the interval  $dt$  from the time when the beam leaves the beam splitter ( $t = 0$ ) to the time when it arrives at the end mirror ( $t = t_L$ ) located at a distance  $L$  from the beam splitter. Terms of the order  $h_+^2$  and higher can be omitted in the calculation since in the weak field limit  $h_+ \ll 1$  holds. For the  $x$ -arm the squared space-time interval is

$$ds^2 = -c^2 dt^2 + (1 + h_+) dx^2 = 0 \quad (1.6)$$

which gives

$$dt = \frac{1}{c} \sqrt{1 + h_+} dx. \quad (1.7)$$

The resulting travel time for the light from the beam splitter to the x-end mirror is

$$\begin{aligned}\int_0^{t_L} dt &= \frac{1}{c} \int_0^L \sqrt{1+h_+} dx \\ &\approx \frac{1}{c} \int_0^L (1+h_+/2) dx \\ &= \frac{L}{c} (1+h_+/2).\end{aligned}\tag{1.8}$$

For the return trip the same value is obtained so that the optical round-trip time in the  $x$ -arm is  $\frac{2L}{c} (1+h_+/2)$ .

For the  $y$ -arm the calculation yields:

$$\begin{aligned}\int_0^{t_L} dt &= \frac{1}{c} \int_0^L \sqrt{1-h_+} dx \\ &\approx \frac{L}{c} (1-h_+/2)\end{aligned}\tag{1.9}$$

The resulting optical path length difference  $\Delta L_{pl}$  between the two arms is

$$\Delta L_{pl} = 2L(1+h_+/2) - 2L(1-h_+/2) = 2Lh_+.\tag{1.10}$$

which can be read out at the interferometer output port provided the instrument is sufficiently sensitive. The length change  $\Delta L$  of a single interferometer arm is

$$\Delta L = \frac{\Delta L_{pl}}{4} = \frac{L}{2} h_+.\tag{1.11}$$

### 1.1.3. Sources of gravitational waves and their detection

This section gives a brief overview of the most promising astrophysical sources of gravitational wave radiation. A detailed review on gravitational wave sources can be found in [18].

#### 1.1.3.1. Supernovae

Supernovae are expected to be an astrophysical source of gravitational wave burst signals. These signals have a very short duration containing only a few cycles of their main frequency component. A supernova is a stellar core collapse that occurs after the nuclear fuel of a star is

depleted and it is no longer supported by the release of nuclear energy. The gravitational waves emitted during the resulting collapse contain information about the non-spherical dynamics of the process. Depending on the mass of the star either a neutron star or a black hole is formed in the collapse. Detection of the emitted gravitational wave radiation would allow to determine the final state of the core.

In order to detect bursts in data from gravitational-wave detectors excess power algorithms are applied to the data. Advanced algorithms work both in the time and the frequency domain. They identify candidate events by looking for time stretches and frequency bands that contain more power than expected from the statistical properties of the data.

### 1.1.3.2. Inspiral binary systems

Binary systems that consist of neutron stars (NSs) or black holes (BHs) emit gravitational wave radiation as the two partners revolve around the common center of mass. The distance between the two objects will gradually decrease due to dissipation of energy so that they eventually merge. In the final phase of the coalescence the signal strength and rotational frequency increases rapidly. This chirp type signal runs through the detection band of earth bound gravitational-wave detectors. By modeling systems and calculating the expected waveforms matched filters can be generated that are optimized to find these waveforms in the detector data.

Measuring gravitational waves from binary systems would provide new astrophysical insights. The waves emitted during the merger of a BH/BH binary system reveal the dynamics of the process. In addition highly nonlinear oscillations of space-time occurring during the merger process and the vibrational ring down of the newly formed BH are expected to show up the the gravitational wave signature. For a BH/NS system a tidal disruption of the NS by the gravitational field of the BH companion is expected. Thus the resulting gravitational waves contain information about the NS structure and its equation of state.

### 1.1.3.3. Pulsars

Pulsars are spinning neutron stars which posses a strong magnetic field. The electrons accelerated in this field emit directional electromagnetic radiation. For the pulsars that are detectable from the earth the rotation axis and the magnetic field are oriented in a way that the beam of radiation sweeps across the earth during each rotation cycle. The resulting highly stable periodic pulse is detectable with a radio telescope. Theoretical models suggest that the solid crust of a neutron star can maintain a mass distribution that is not symmetric with respect to its rotation axis. This asymmetry would lead to the emission of gravitational waves.

The quadrupole component of the gravitational wave radiation is at twice the rotation frequency of the neutron star. Some pulsars observed in radio telescopes have a rotation period in the ms range so that the signal is in the detection band of current gravitational-wave detectors. The data gathered in the radio observations reveal parameters of the pulsar like the position in the sky and the expected gravitational wave signal frequency. This information



allows to predict the signal to a high accuracy. The position of the pulsar in the sky can be used to account for the Doppler shift of the signal due to the changing velocity of the earth relative to the source. After the Doppler shift correction the signal can be coherently integrated over months to increase the SNR.

Searching for pulsars in the time domain is done by demodulating the gravitational wave signal  $h(t)$  with the expected signal  $\tau(t)$ :

$$\text{SNR} = \frac{2}{T} \int_0^T h(t) \tau(t) dt \quad (1.12)$$

The timing accuracy of the recorded data is very important since a constant timing offset  $\delta t$  decreases the signal to noise ratio (SNR). For a pulsar emitting a signal at the frequency  $\omega$  and a constant timing offset of  $\delta t$  the fractional SNR is given by

$$\begin{aligned} \text{SNR}_{\delta t} &= \frac{2}{T} \int_0^T \sin(\omega t) \sin((\omega t + \delta t)) dt \\ &= \cos(\omega \delta t) \simeq 1 - \frac{1}{2}(\omega \delta t)^2 \end{aligned} \quad (1.13)$$

Using a value of  $\omega = 2\pi \times 1000$  Hz for the signal frequency a timing offset of  $\delta t = 10\mu\text{s}$  gives a value of 99.8% for the fractional SNR. This means that the SNR is 0.2% lower than it would be if the timing offset  $\delta t$  was zero.

#### 1.1.3.4. Stochastic gravitational wave background

Theoretical models of the early universe predict the existence of a stochastic gravitational wave background. This signal originates from vacuum fluctuations during the Planck era and was amplified by coupling to the background curvature of space-time. All plausible models predict a signal level that is below the instrumental noise of the current generation of gravitational wave detectors. This means the only feasible way of trying to detect the signal is to cross-correlate data from two or more instruments. If these detectors are separated by a large distance, most instrumental noise sources will be uncorrelated between the different sites. As the cross-correlation of two uncorrelated noise representations has an expectation value of zero, a small correlated component in the detector signals can be detected in the presence of much stronger uncorrelated noise.

## 1.2. The gravitational-wave detector GEO 600

### 1.2.1. Overview

The gravitational-wave detector GEO 600 [19, 58, 34] is a project that was constructed and is operated by a British-German collaboration. Construction of the detector was started in 1995 in Ruthe near Hannover, Germany. The arms of the GEO 600 interferometer are oriented in the direction  $334.1^\circ$  (NNW) and  $68.4^\circ$  (ENE) and have a physical length of 600 m each. The infrastructure at the detector site includes a central station and two end stations that accommodate the electronics and the optical setup. All interferometer optics are suspended in vacuum tanks at a pressure in the  $10^{-8}$  mbar range to avoid contamination, acoustic coupling, air-friction damping of the suspended mirrors and index of refraction fluctuations along the laser beam line. Protected by a covered trench, 600 m long vacuum tubes with a diameter of 60 cm connect the central vacuum cluster with the tanks in the end stations. Gate valves allow disconnection of the tubes from the rest of the vacuum system. Whenever it is required to open one of the vacuum tanks a clean environment is necessary to avoid any contamination of the high quality optics. Therefore the area around the tanks was separated from the rest of each building and turned into a class 1000 clean room. An additional tent can be moved over each tank to provide a class 100 environment.

In order to be able to backtrack external disturbances that show up in the output signal of the detector a system of sensors recording environmental data (seismic motion, magnetic fields, etc.) was installed at the GEO 600 site [52]. A data acquisition system (DAQS) [36] is in place to record up to 64 channels at a maximum sampling rate of 16 384 Hz and 64 additional channels at 512 Hz. The data is transferred to the final storage place via a 35 MBit/s radio link that connects the GEO 600 site to the Albert-Einstein-Institut in Hannover.

### 1.2.2. Optical configuration

The light source for the optical setup of GEO 600 is a 12 W Nd:YAG laser emitting at a wavelength of 1064 nm. Higher order spatial modes of the beam are rejected by two sequential mode-cleaners before the light is injected into the interferometer (figure 1.3). In addition the mode-cleaners are used to prestabilize the laser frequency. Both mode-cleaners are triangular cavities with a round-trip length of about 8 m. A power-recycling mirror in the input port of the interferometer increases the light power circulating in the interferometer. The effective arm length of GEO 600 is doubled by folding the optical path once, thus the light is passed through the arms twice before it is recombined at the beam splitter. A signal-recycling mirror in the output port of the interferometer allows tuning of the shot noise limited sensitivity. Higher order spatial modes contained in the output light will be filtered out by an output-mode-cleaner before the light is sent to the output-photo detector. GEO 600 uses the advanced optical technique of dual recycling [23, 30, 31, 32] which is the combination of power-recycling and signal-recycling. The resulting improvement in sensitivity can partially compensate for the performance penalty due to the relatively short arms of GEO 600 compared to other current generation gravitational-wave detectors ([51, 21]).

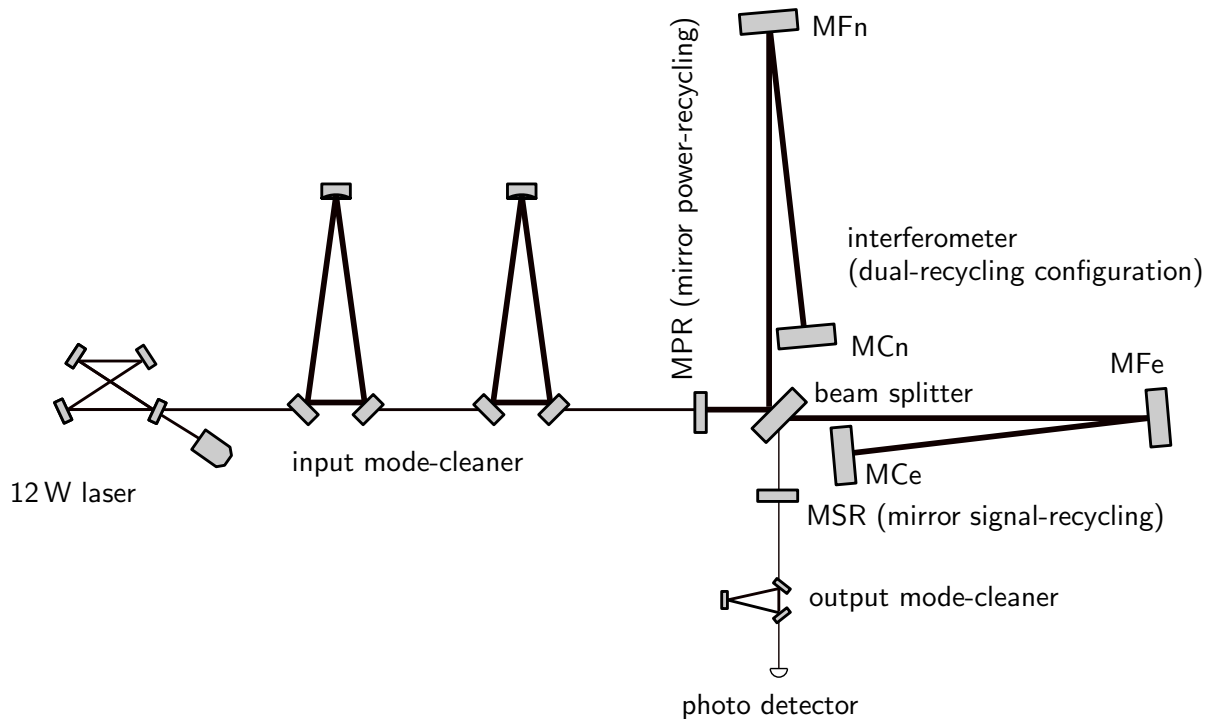


Figure 1.3.: Optical configuration of GEO 600.

### 1.2.3. Laser system

The GEO 600 laser system [15, 47, 57] was designed and built by the *Laser Zentrum Hannover* in cooperation with the *Institut für Atom- und Molekülphysik, Universität Hannover*. It employs an injection locking scheme [50] to generate a 12 W beam at a wavelength of 1064 nm: A low-power master laser beam at 0.8 W with high frequency and amplitude stability is injected into a bow tie slave-laser cavity. Two laser-diode pumped Nd:YAG rods serve as gain medium. The resonance frequency of the cavity is locked to the frequency of the master beam using a Pound-Drever-Hall [22] setup. This ensures that the high power beam emitted by the slave laser inherits the high frequency stability of the seed beam injected from the master laser. An additional intensity stabilization servo [49] ensures that the intensity noise of the complete laser system fulfills the requirements for GEO 600: At a frequency of 100 Hz the relative intensity noise needs to be below  $5 \times 10^{-8} \text{ Hz}^{-\frac{1}{2}}$ .

### 1.2.4. Mode-cleaners

Spatial modes other than  $\text{TEM}_{00}$  are substantially suppressed by passing the light from the laser system through two sequential triangular mode-cleaner cavities [25, 26]. This provides the required pointing stability of the beam. To isolate the mode-cleaner mirrors from the motion of the ground, a double pendulum suspension is employed: The mirrors are hanging from an intermediate mass which is in turn suspended from a support structure inside the

vacuum tanks. The motion of the intermediate mass is sensed against the support structure so that the relevant mechanical eigenmodes of the pendulum can be damped by magnet-coil actuators [55]. Orientation and position of the mirrors are controlled by an auto-alignment system [29]. This system measures the angle between the incoming laser beam and the axis of the cavity eigenmode. By continually adjusting the mirror orientation with a servo system a maximum throughput of light can be maintained.

### 1.2.5. Interferometer

The GEO 600 interferometer is designed to be most sensitive in the frequency band from 50 Hz to a few kHz. Figure 1.5 shows the design sensitivity of GEO 600 determined by the individual noise contributions: seismic noise, thermal noise of the suspension and the internal mirror modes [28], thermorefractive noise and shot noise for the detuned signal-recycling configuration [24].

The ambient seismic noise level at the GEO 600 site is eight orders of magnitude higher than the displacement noise specifications in the GEO 600 measurement band. The steep roll off of the seismic noise level is attained by suspending the beam splitter, the signal-recycling mirror and the mirrors in the arms of the interferometer as the lowest stages of triple pendulums [45], called main suspension (see figure 1.4). For the power-recycling mirror a double pendulum suspension is employed. The upper mass of each pendulum chain is damped at the resonance frequencies by six magnet-coil actuators attached to the support structure. The pendulum resonances of the lower masses are damped by dissipation of energy to the upper mass.

A reaction pendulum is situated 3 mm behind each of the pendulum chains that supports the end mirrors, the power-recycling mirror and the signal-recycling mirror. These allow exertion of control forces from a seismically isolated platform. For the end mirrors, forces can be applied to the two lower stages of the suspension. The intermediate masses have magnet-coil actuators while for the bottom stages electrostatic drives are employed. The reaction pendulum of the signal-recycling mirror and the power-recycling mirror provide magnet-coil actuators that can apply forces directly to the mirrors.

The servos for the suspension system, the mirror positions and the laser frequency are implemented as analog control loops. A digital interface [16] written in *LabVIEW* [70] allows configuration of some of the control loop parameters (e.g. gain settings).

GEO 600 is the first kilometer scale interferometer to use monolithic suspensions [25, 13, 27] for the beam splitter and the test masses in the interferometer arms to reduce the mirror motion in the measurement band due to thermal noise. Suspending the test masses from monolithically attached fibers minimizes the energy dissipation and allows  $Q$  values in excess of  $10^8$  for the pendulum resonance. A low dissipation suspension is required to obtain low internal thermal noise of the test masses.

Power recycling is employed to reduce the shot noise level. In the operation mode the interferometer is set to the dark fringe. This means that the arm length difference is adjusted so that the carrier light fields from the two arms cancel at the output port and the light is

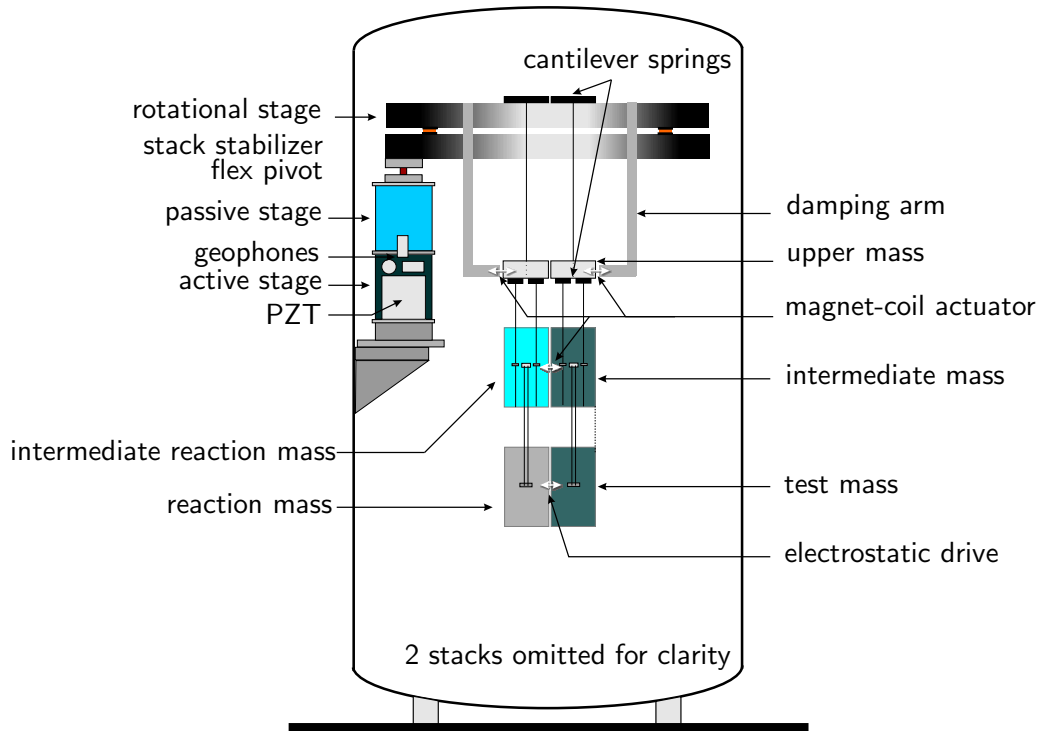


Figure 1.4.: Suspension of the interferometer end mirrors inside the vacuum tanks.

reflected back to the input port. In this state the interferometer, as seen from the laser, acts like a mirror so that a power-recycling cavity can be formed by adding the power-recycling mirror in the input port. The position of this mirror is controlled by a Pound-Drever-Hall loop that keeps the optical path length of the power-recycling cavity resonant with the laser wave length. This increases the light power circulating in the GEO 600 interferometer by a factor of approximately 300 and thus increases the shot noise limited signal-to-noise ratio. In addition the signal-recycling mirror is used to decrease the shot noise level in an adjustable frequency range by altering the storage time for the signal sidebands. The reflectivity of the signal-recycling mirror specifies the bandwidth while its microscopic position defines the central frequency.

### 1.2.6. Environmental monitors

The GEO 600 interferometer is designed to detect extremely small changes in the differential arm length defined by the position of the interferometer test masses (mirrors). A number of external disturbances acting on the detector can lead to mirror motion and thus mimic a gravitational wave signal. To track down couplings from the environment to the detector output signal, a system of environmental sensors (figure 1.7) is installed at the GEO 600 site.

Seismic motion of the ground is the most apparent source of excess mirror movement. A displacement of the suspension point will travel through the pendulum stages and change

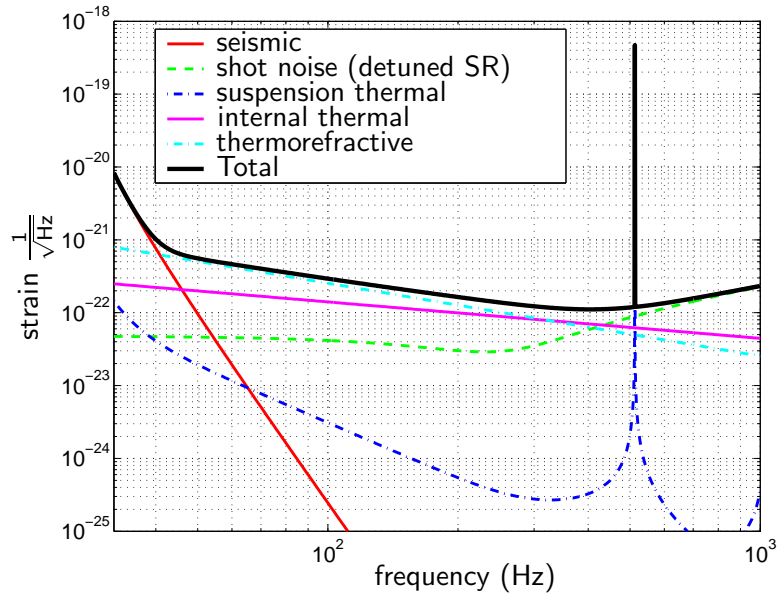


Figure 1.5.: Design sensitivity of GEO 600 in the detuned signal-recycling configuration (Transmittivity of SR mirror: 1%).

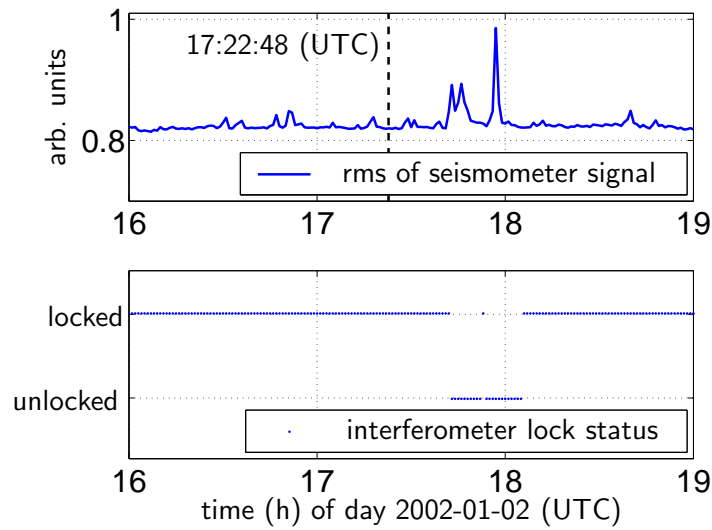


Figure 1.6.: Root-mean-square value of seismometer data measured during an earthquake of magnitude 7.2 in the South-West Pacific near Tuvalu, 16 000 km away from the GEO 600 site. The earthquake occurred at 17:22:48 (UTC). U.S. Geological Survey projected a travel time of about 20 min for the shock waves from the epicenter to Central Europe. The motion of this earthquake broke the lock of the GEO 600 interferometer during the E7 data run. This can be seen in the lower figure that shows data from the lock status channel of the interferometer with a resolution of one minute.

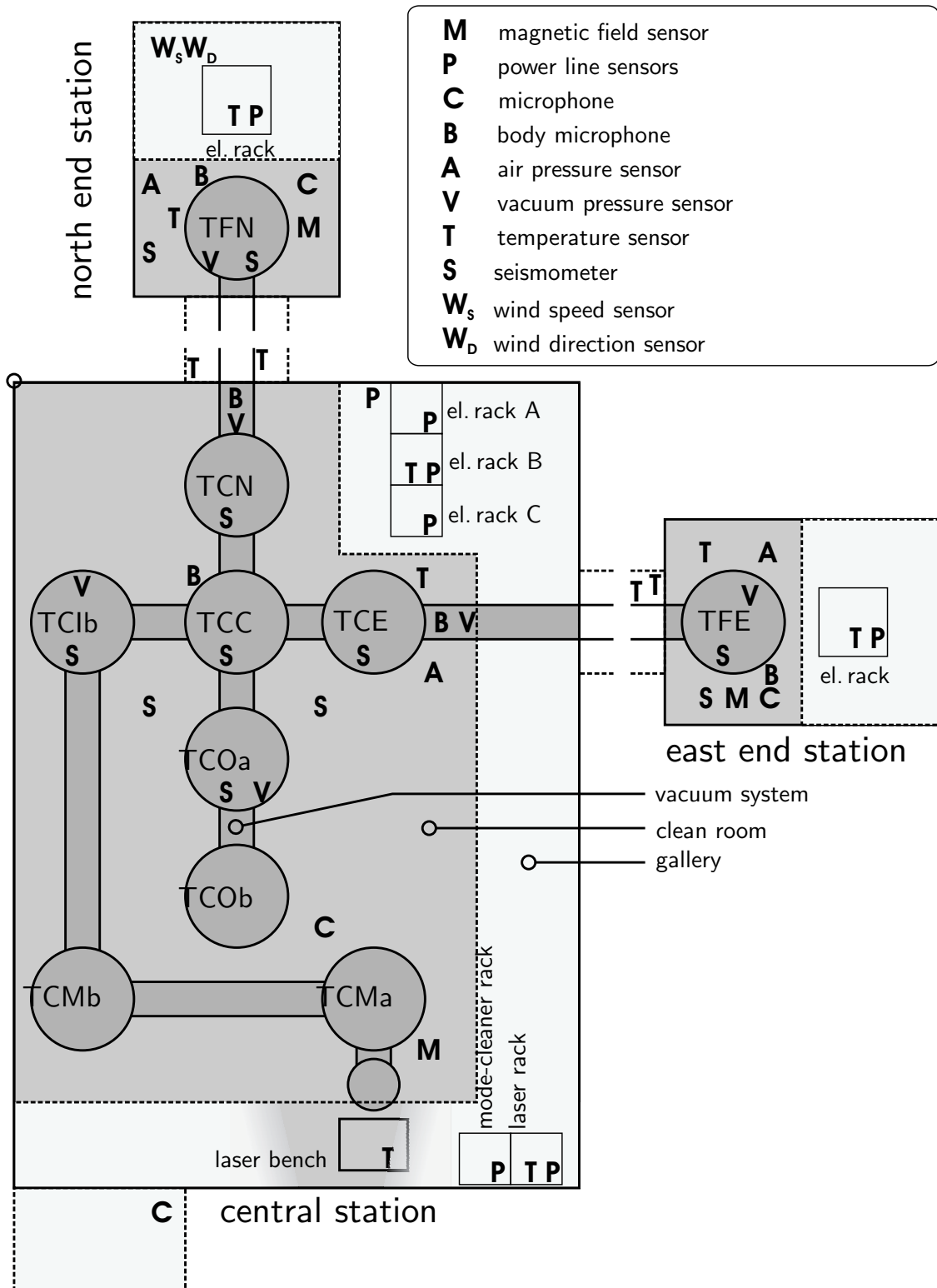


Figure 1.7.: Location of the environmental sensors.

the position of the mirror. In the measurement band of GEO 600 above 50 Hz the pendulum stages sufficiently suppress excitation coming from the suspension point. The major problem with seismic noise is the excitation of the mirror suspension resonances at about 1 Hz. This can lead to a significant increase in the root-mean-square motion of the mirror. A sensitive measurement of the differential arm length can only be performed as long as the interferometer is in the locked state, i.e. the proper position and orientation of all mirrors can be maintained by the control loops. Excess motion that leads to saturation in the loops can break the locked state of the interferometer.

Sources of seismic motion include earthquakes, which can create significant motion even if the epicenter is thousands of kilometers away (see figure 1.6). Other sources of seismic noise are high local wind speeds and ocean waves hitting the coastline. In addition there are a number of human-made noise sources, e.g. moving vehicles. To record these disturbances seismometers are installed on the floor of each building. Additional seismometers are installed in the support structures inside the vacuum tanks (figure 1.4). These sensors can measure directly the motion coming from the ground or the vacuum system that is traveling up to the suspension point of the mirror. Sensors for the wind speed and direction are mounted on the roof of the north end station to monitor the influence of wind-induced seismic motion. Disturbances coming from the vacuum chambers are recorded by body microphones attached to the vacuum cluster and microphones installed in the clean rooms allow tracking down sound coupling to the tanks.

Fluctuations in the magnetic field surrounding the vacuum tanks could couple to the mirrors and thus show up in the output signal. The magnetic actuators attached to the intermediate masses convert the magnetic field amplitude to displacement of the mirrors. In the central station and the two end stations magnetic field sensors are installed to record both slow drifts and transients in the magnetic field.

The electronic circuits controlling the mirror positions and reading out the signal from the output port are susceptible to glitches in the power supply. All electronics are fed from uninterruptible power supplies to prevent voltage transients on the power grid from coupling into the supply voltage. To monitor any variation in the voltage supplied by the uninterruptible power supplies sensors are installed in each unit.

Drifts in the alignment that influence the performance of the interferometer can be caused by temperature changes over the day or by changes in the ambient air pressure. Pressure sensors and a number of temperature sensors installed both inside and outside the buildings keep track of these parameters.

The data recorded from the different sensors allow determining coupling mechanisms of external disturbances to the gravitational wave channel and thus help to improve the sensitivity. In addition, the data provide a veto mechanism for events seen in the gravitational wave channel by looking at coincidences with external disturbances.



## Chapter 2.

# The Data Acquisition System of GEO 600

Gravitational-wave detectors like GEO 600 have to record data over periods of several months with as little interruption as possible to make the search for gravitational wave signals in the data easier. One such example are signals from continuous sources like pulsars that are expected to have a very low SNR. Therefore the signal needs to be integrated over an extended period to distinguish it from the noise background. Also, for the detection of single events like burst and inspirals, a very low downtime of the gravitational-wave detector is desirable. For a reliable detection of such a signal it needs to undergo a coincidence analysis that makes sure a signal with the same parameters (arrival time, amplitude, etc.) was seen in more than one detector. To obtain a considerable temporal overlap between the data stretches from different detectors, each individual detector has to achieve a high duty cycle over a long time. The need of a high duty cycle has been demonstrated in the analysis of data from gravitational wave bar detectors [12].

This means that every gravitational-wave detector needs a robust and reliable data acquisition system (DAQS) that can acquire data continuously over several months. In addition to the detector output signal, which contains the  $h(t)$  information, a number of additional signals need to be recorded. For the GEO 600 detector more than 100 auxiliary channels are recorded that are required for diagnostics and to monitor external disturbances on the detector. The DAQS digitizes all these analog voltage signals and stores them in a standardized format. In this chapter the requirements and the design of the GEO 600 DAQS is explained in detail. In addition the results of the measurements done to test the performance of the system are presented.

### 2.1. Requirements

The DAQS has to meet a number of requirements which will be laid out in the following sections. First of all one has to make sure that the noise introduced by the analog to digital conversion process does not limit the overall performance of the detector. In the detection band the noise contribution from the AD conversion has to be negligible. The DAQS will record data at a rate of about 1 MByte/s. All DAQS components have to be fast enough to process a continuous data stream at this rate. In addition the data need to be time stamped with a high accuracy. High reliability of the system is required to minimize the downtime of

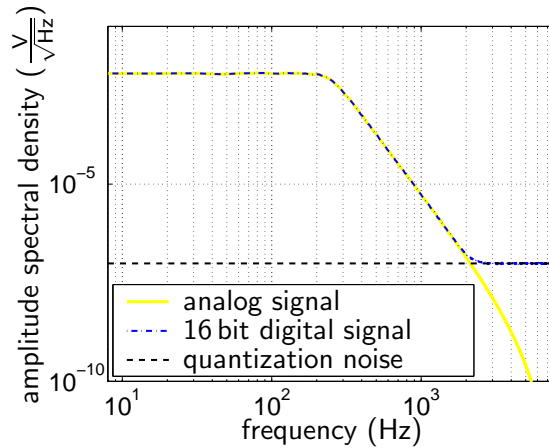


Figure 2.1.: Dynamic range limit due to amplitude quantization.

the GEO 600 instrument. These requirements are explained in more detail in the following sections.

### 2.1.1. Analog to digital conversion process

In order to store the GEO 600 data in digital form the analog signals produced by the electronics need to be passed through an analog to digital converter (ADC). The AD conversion process quantizes the signal both in amplitude and in time: the digital signal is represented by amplitude values that are taken from a finite set of  $2^n$  numbers, where  $n$  is the sampling resolution of the ADC. In addition the amplitude values are only defined for discrete points in time  $m \times t_s$ ,  $m \in \mathbb{N}$ , which are integer multiples of the sample time  $t_s$ . The quantization in amplitude introduces quantization noise and leads to a limited dynamic range of the digital signal. The quantization in time leads to a limited bandwidth of the signal. Sampling rate and the sampling resolution need to be chosen properly so that the DAQ process does not limit the sensitivity of the instrument.

#### 2.1.1.1. Quantization noise

The noise contribution that is contained in the digital signal due to the rounding of the amplitude value to the next discrete value depends on two parameters inherent to the ADC: The sampling resolution  $n$  (measured in bits) and the dynamic range  $U_{\text{dyn}}$ . The voltage difference  $U_{\text{lsb}}$  between two adjacent quantization steps is  $U_{\text{lsb}} = \frac{U_{\text{dyn}}}{2^n}$ . The amplitude spectral density (ASD) of the noise introduced by the AD conversion process is  $U_q = \frac{U_{\text{lsb}}}{\sqrt{6}f_s}$  (see appendix B for details). The analog signal to be recorded needs to be above this noise level in all frequency regions. Figure 2.1 illustrates the problem that can arise: The yellow curve shows the ASD of a signal with a dynamic range that is too large to be sampled with 16 bit resolution. Above 2 kHz the digital signal is dominated by quantization noise.

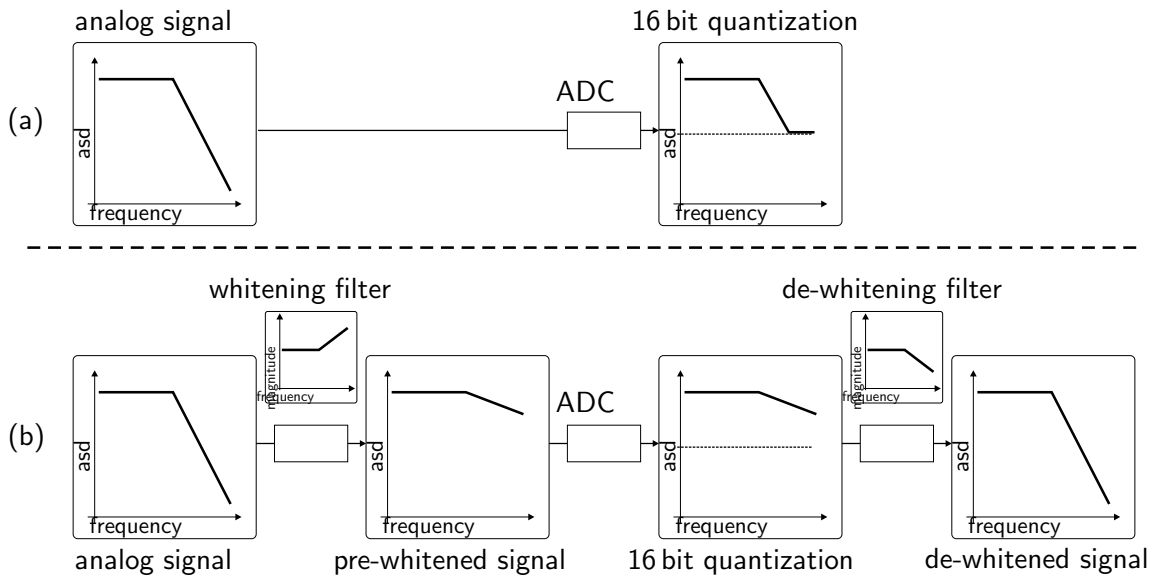


Figure 2.2.:

(a): When applying an analog signal directly to an AD converter quantization noise can dominate the digital signal at some frequencies.

(b): The problem can be avoided by pre-whitening the signal before the AD conversion.

Signals that have largely varying power over the recorded frequency range have to be “pre-whitened” before they are fed to the ADC. This means that the analog signal is passed through a “pre-whitening” filter that equalizes the amount of power in the different frequency bands of the signal. The smaller the dynamic range of the ADC the more complex is the filter that is required to bring all regions of the spectrum above the quantization noise level. After the sampling process, the data can be converted to a number format that has a larger dynamic range than the ADC so that the whitening process can be reverted by applying the de-whitening filter. The process of whitening and de-whitening a signal is illustrated in figure 2.2(b).

The ADCs employed in the GEO 600 DAQS have 16 bit resolution introducing quantization noise at a level of  $195 \frac{nV}{\sqrt{Hz}}$  when the ADC dynamic range is  $\pm 2V$ . A sampling resolution of 16 bit is large enough so that the required whitening filters can be built with simple transfer functions containing only a small number of poles and zeros.

### 2.1.1.2. Sampling rate

Sampling an analog signal at a rate of  $f_s$  limits the bandwidth to  $f_N = f_s/2$  which is called the Nyquist frequency. At the sampling points  $t_n = \frac{n}{f_s}$  any signal  $A_1$  with a frequency  $f_1 < f_N$  is indistinguishable from a signal  $A_2$  with the same amplitude at a frequency  $f_2 = f_1 + mf_s$

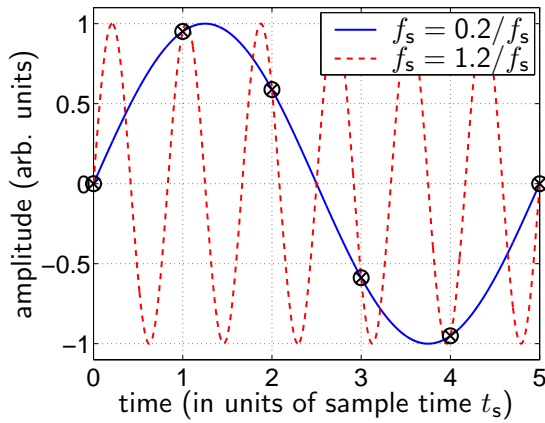


Figure 2.3.: Sampling in the time domain: At the sampling points a sinusoidal signal with a frequency below the Nyquist frequency (solid curve) is equal to a signal that is offset by  $f_s$  (dashed line).

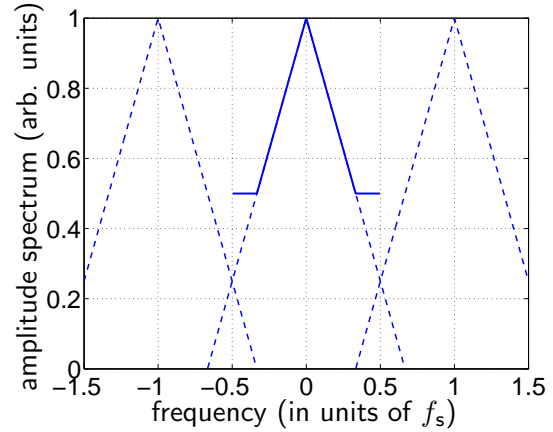


Figure 2.4.: Adding frequency components due to aliasing: The resulting spectrum (solid curve) after the AD conversion is the sum of the original spectrum (central dashed curve) and the spectra shifted by  $f_s$ .

that is offset from  $f_1$  by an integer multiple of  $f_s$ :

$$\begin{aligned}
 A_1(t_s) &= A \exp(i2\pi f_1 t_s) \\
 &= A \exp(i2\pi f_1 t_s) \underbrace{\exp\left(i2\pi f_s \frac{nm}{f_s}\right)}_1 \\
 &= A \exp(i2\pi f_1 t_s) \exp(i2\pi f_s m t_s) \\
 &= A \exp(i2\pi (f_1 + m f_s) t_s) = A_2(t_s)
 \end{aligned} \tag{2.1}$$

This is illustrated in figure 2.3 that shows two signals at  $0.2f_s$  and  $1.2f_s$ .

All signal components of the analog signal at frequencies  $f, f + f_s, f + 2f_s, \dots$  are added up in the spectrum of the digital representation of the signal. This effect is called “aliasing” and is illustrated in figure 2.4. The central dashed curve is the spectrum of an analog signal encompassed by the spectrum shifted by the sampling frequency. The solid line is the resulting spectrum of the digital signal which is the sum of the central curve and the spectra shifted by  $f_s$ . To avoid aliasing all frequency components higher than  $f_N$  need to be removed by a low-pass filter which is called an anti-aliasing filter.

For the DAQS a sampling frequency of 16 384 Hz was chosen. The effective bandwidth is reduced from the Nyquist frequency of 8 192 Hz to about 7 kHz due to the employed anti-aliasing filters. This is sufficiently high for the GEO 600  $h(t)$  signal which has a bandwidth of about 2 kHz. The sampling frequency was chosen to be a power of two so that the data

can be successively decimated by factors of two down to 1 Hz without ever obtaining samples that belong to two different GPS seconds.

### 2.1.2. Timing accuracy

The data recorded at the GEO 600 detector site will be exchanged with data analysis groups from other detectors. Once data streams recorded at different detector sites are merged into a common data set, accurate time stamping of the data becomes important. Only if each data stream has proper time stamps, can the data be aligned to a common time axis.

An example of a data analysis algorithm that requires data from more than one detector is the targeted search for pulsar signals. Using the gravitational wave channel in conjunction with the data from a radio telescope one can search for gravitational wave signals of pulsars that are visible by their electromagnetic emission in the radio telescope data.

It was shown in section 1.1.3.3 that an error in timestamping the data decreases the SNR in a time domain search for a known pulsar signal. A absolute timing offset of  $\leq 10 \mu\text{s}$  was demanded from the data analysis group involved in pulsar searches [7]. Also for resolving the direction of arrival of a gravitational wave burst signal a high accuracy of the timestamps is desirable as it is shown in section 3.2.

For the GEO 600 DAQS the aim is to limit the timing offset to less than  $10 \mu\text{s}$ . By shifting the data by an integer amount of samples the timing offset of the data can be reduced to a value between  $-30.5 \mu\text{s}$  and  $30.5 \mu\text{s}$ . The remaining timing offset will be recorded so it can be removed by shifting the data by a fraction of a sample time in case this is required for a specific search algorithm.

### 2.1.3. Data rate

The overall data rate for all channels recorded at the site is 1 MByte/s. This includes the signals from the interferometer, the mode cleaners, the laser system and the environmental sensors. In addition, some of the bandwidth is needed for the calibrated  $h(t)$  channel that is produced at the GEO 600 site from the interferometer signals. It is necessary that all computers involved in the DAQ process and all the links between the machines are fast enough to handle this data rate.

## 2.2. System design

### 2.2.1. Overview

The current DAQS is based on hardware of an earlier system that was developed before 2001. This system was built using the same hardware components that were being used for the DAQS of the LIGO detectors. The early system developed for GEO 600 showed a number of

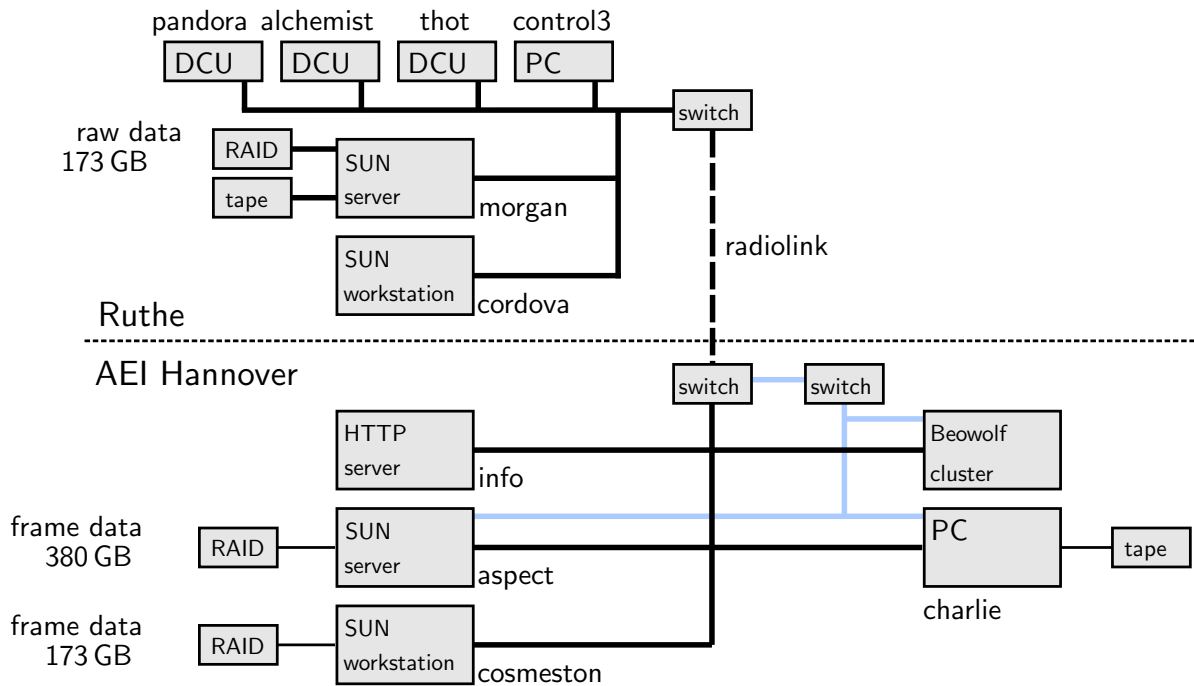


Figure 2.5.: Hardware setup of the GEO 600 DAQS.

problems. It was unreliable and any interaction with the system (e.g. reconfiguring channels) required deep knowledge of the system. To solve these problems, it was finally decided that a complete redesign of the system was necessary and desirable. The software needed to be rewritten from scratch and unreliable hardware components had to be replaced. Most of the components proved to be reliable so that they could be reused for the new system. An overview of the hardware employed in the current GEO 600 data acquisition system can be seen in figure 2.5.

A schematic of the software handling the data is shown in figure 2.6. Analog signals need to be recorded in the central station and in the two end stations. A VME crate which contains the hardware required for sampling and time stamping the data is installed in each of these buildings. These crates are called “data collecting units” (DCUs). The DCUs send the digitized data via a TCP/IP network to a central server called *morgan*. In addition, the data from the *LabVIEW* control system [16] is sent to this computer. On this machine basic processing of the incoming data is carried out: each channel can be filtered, decimated and reduced in resolution according to user defined settings. The settings are retrieved from a database server running on the same machine. The configuration of a channel can be changed using a database front end that is running on the HTTP server called *info*. This front end allows interaction with the database in a user-friendly way. After the data are processed on *morgan*, it is written to a local disk array that can hold approximately 2 days worth of data. The data are converted to the final data storage format by a program running on the server *aspect* in Hannover that has access to the data on the detector site via a radio link. This program converts the data to the *frame format* [64] that is a common data format used by the LIGO,

VIRGO and TAMA group. In Hannover, the most recent four days of data can be stored on the RAID disk connected to *aspect*. This data need to be forwarded to the final storage facilities in Cardiff and Berlin. For the transfer to Berlin, a network link via the Internet is used to copy the data. Since the network link from Hannover to Cardiff is too slow for a real-time transfer, the data need to be written to tapes and sent over to Cardiff by mail. These tasks are done by a machine called *charlie*. The data are compressed and checksums are generated that are written to the tapes together with the data. The tape drive automatically ejects and loads up to seven tapes that can store more than one day worth of data each. This reduces the required amount of human interaction with the system.

## 2.2.2. Acquiring the data

### 2.2.2.1. Data Collecting Units (DCUs)

Each data collecting unit contains a GPS receiver, a timing card, a processor board and an *ICS110B* ADC board. The DCU in the central station has an additional *VMIC* ADC board. A schematic of a DCU can be seen in figure 2.7.

**ICS110B AD converter boards** For sampling the analog signals produced by the GEO 600 detector, *ICS110B* [67] data acquisition boards are employed. Two different types of these boards are used: in the end stations 16 channel boards are installed while the central station DCU contains a 32-channel board. These *ICS110B* boards provide synchronous sampling on all of their channels which gives a better timing accuracy of the sampling process compared to a multiplexed system which uses a single ADC for sampling all channels. Multiplexing the signals introduces a delay between the sampling processes in individual channels and therefore degrades the timing accuracy.

All signals connected to the *ICS110B* are passed through an on-board signal conditioning unit. Its first stage is a differential receiver that rejects common-mode disturbances on the incoming signals. Then the input signals pass through an analog one-pole low pass filter with a corner frequency of 75 kHz. Using this simple filtering scheme is sufficient to prevent aliasing because the ADC used on the *ICS110B* board has built-in  $64\times$  oversampling: Set to an output sampling rate of  $f_{out}$  the AD converter samples the signal at a rate of  $f_{sr} = 64 \times f_{out}$  and then digitally low-pass-filters and decimates the signal to  $f_{out}$ . This means that the Nyquist frequency of the sampling process is 32 times higher than the output sampling rate. Therefore a single pole low pass filter is sufficient to suppress frequency components above the Nyquist frequency.

The *ICS110B* has a gate delay of approximately 37 samples. This means that there is some delay between a signal connected to one of its inputs and the sampled output data. The major portion of this gate delay (34 samples) arises from the digital filter used in the anti-aliasing process. The remainder of the measured delay is thought to arise from other clock delays in the circuits of the board. This gate delay is important for accurate time stamping of the data.

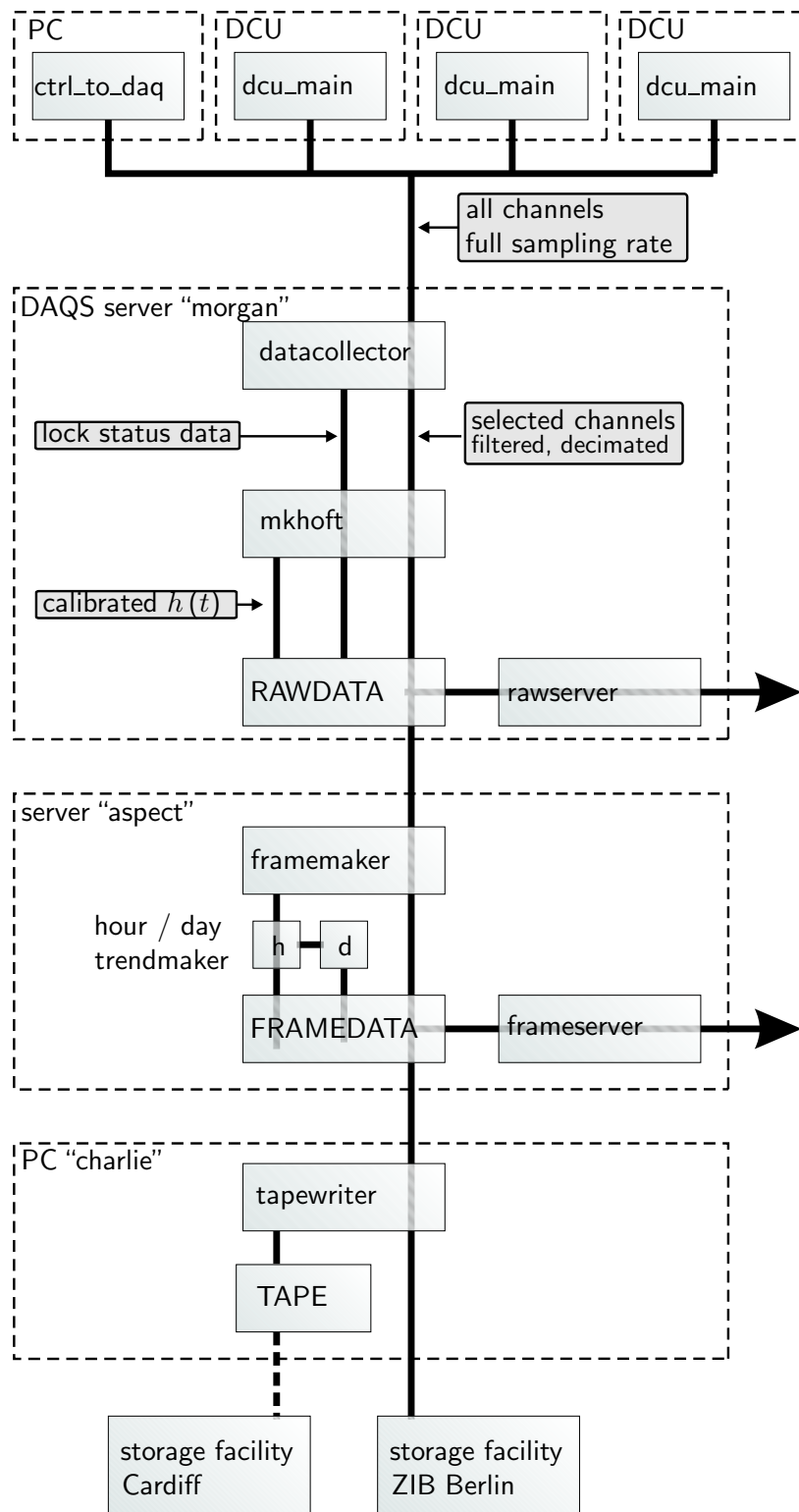


Figure 2.6.: Data flow in the GEO 600 DAQS.



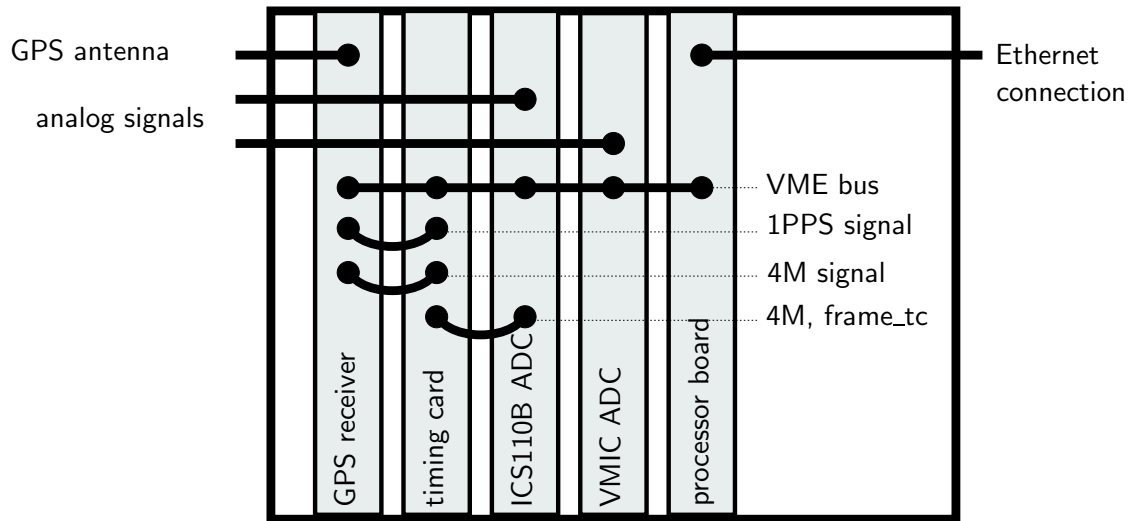


Figure 2.7.: Schematic of a Data Collecting Unit (DCU).

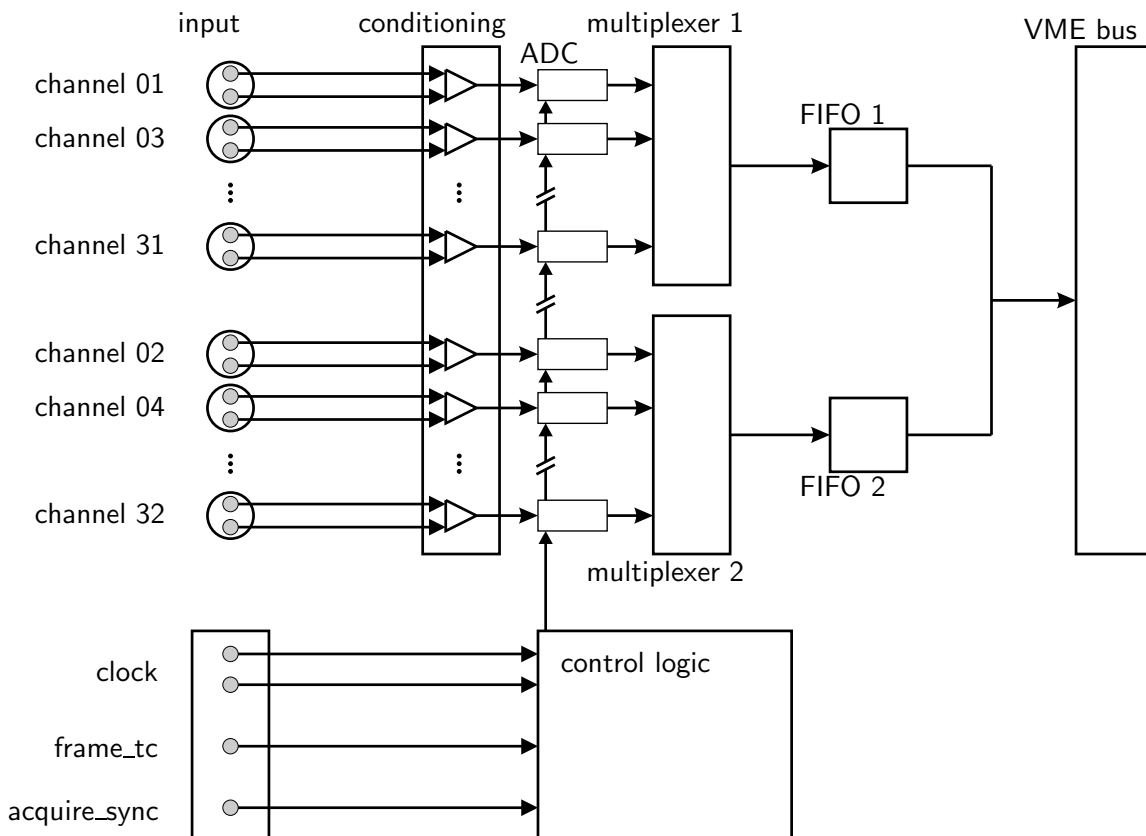


Figure 2.8.: Schematic of the *ICS110B* ADC board.

The software that controls the sampling process of the *ICS110B* removes the gate delay from the data by discarding the first 37 samples when the board is first initialized.

The signal conditioning unit contains software programmable preamplifiers. By sending a command to the VME interface of the *ICS110B*, the gain of these amplifiers can be set to values in the range from +20 dB to -8 dB. This makes it possible to connect input signals with a dynamic range from  $\pm 0.2$  V to  $\pm 8$  V while using the full dynamic range of the ADC which is  $\pm 2$  V.

From the conditioning unit the signal is fed to the ADCs. The *ICS100B* board employs *Crystal CS5397* integrated circuits from *Cirrus Logic* [61] to perform the AD conversion. The sampling process on each ADC is synchronized by a common sample clock signal that is generated by control logic. Figure 2.8 shows the data flow in the *ICS110B* board. The data coming from each individual ADC are combined using digital multiplexers. The data from the multiplexers are sent to two FIFO buffers that can store up to 256 KByte of data. Software running on a processor board can read out the contents of the buffers via the VMEbus.

The ADCs have a nominal resolution of 24 bit. Measurements showed that the noise floor imposed by the electronic front end limits the resolution to slightly more than 16 bit (see section 2.3.3). Therefore, it was decided to operate the *ICS110B* board in a mode where it discards the lower 8 bit of each sample and generates data at a resolution of 16 bit. In this mode, the data coming from the ADC are truncated to a 16 bit number before it is written to the FIFO buffers. This cuts the data rate by 50% in the subsequent systems that are handling the data because instead of storing one 24 bit number in a 32 bit data type, two samples of 16 bit length can be stored.

**VMIC VMIVME-3113a AD converter boards** A *VMIC VMIVME-3113a* [72] board is used in the central station DCU to record data from environmental monitors. Compared to the interferometer channels, the requirements for these channels are lower in terms of timing accuracy and resolution. The 64 channels are sampled using a multiplexed AD converter. The resulting timing uncertainty due to the multiplexing process is acceptable for these channels. The maximum sampling rate is 512 Hz and the sampling resolution is 12 bit stored in a 16 bit data structure. The input range of the ADC is  $\pm 10$  V. The board does not provide any oversampling or anti-alias filtering. Therefore all connected signals must be filtered to attenuate the frequency components above the Nyquist frequency of 256 Hz. This is done by connecting the signals through an external patch bay that contains electronic filters and amplifiers. The electronic circuits for the amplification are implemented on exchangeable modules. Modules with a gain of 2 and 5 exist that give a dynamic range of  $\pm 5$  V and  $\pm 2$  V respectively for the input signal.

**GPS receiver/ timing card** GEO 600 uses the time standard provided by the *Global Positioning System* (GPS) [66] as reference for the DAQS. The GPS time signal is derived from a set of atomic clocks on board a satellite constellation that are constantly monitored and adjusted and therefore provide a timing signal with a very high precision. A schematic of the GEO 600 timing hardware and the signals derived from the GPS are shown in figure 2.9.

The data coming from the ADCs are packaged into segments of one second length. The first sample of each segment has to be recorded at the start of a GPS second.

The required timing information is provided by a commercial *VME-SYNCCLOCK32* GPS card from *Brandywine Communications* [60]. This card receives and processes the signals from the GPS satellites. It generates a signal called 4M which is a square wave with a frequency of  $2^{22} = 4\,194\,304$  Hz. It is phase locked to the timing signal received from the GPS. An additional 1PPS signal (one pulse per second) marks the GPS second boundaries. A falling edge of the signal marks the beginning of a new GPS second. The *VME-SYNCCLOCK32* provides hardware registers, which can be accessed via the VME bus to read out the number of the current GPS second and the nanosecond count since the last second boundary.

The 4M and the 1PPS signal are fed into the timing card which is a custom made circuit board that generates the electronic signals to drive the *ICS110B* and the *VMIC* ADC boards. The *ICS110B* board is started by setting a signal line called `acquire_sync` from logic high to low. The *VMIC* board is started by applying the sampling clock. When initialized, the timing card does not generate the signals required to start the ADCs until it is set in the “armed” state by a software command. In this state, the card monitors the 1PPS signal from the GPS card. Once a falling edge indicates the beginning of a new GPS second the timing cards lowers the `acquire_sync` line of the *ICS110B* card and starts to send the sampling clock signal to the *VMIC* card. This process makes sure that the data acquisition on both ADC cards is started at the beginning of a GPS second.

For the sampling process, the *ICS110B* requires two signals that have to be derived from the 4M signal to keep the sampling clock phase locked to the GPS. The sampling clock input requires a square wave signal at 256 times the output sampling rate of 16 384 Hz. This signal at a frequency of 4 194 304 Hz can be taken directly from the 4M output of the GPS receiver. In addition, the *ICS110B* requires a signal called `frame_tc` that marks the start of a new output sample by a falling edge. This signal is generated in the timing card by dividing down the 4M signal in a way that the 1PPS falling edge indicating the start of a new GPS second coincides with a falling edge of the `frame_tc` signal (see figure 2.9 and 2.10).

The only signal required by the *VMIC* ADC card is a square wave with a frequency of  $2^{15} = 32\,768$  Hz which is applied to the sampling clock input of the board. This signal is generated by the timing card by dividing down the 4M signal and sending it to the sampling clock input via the VME backplane.

Since all signals used to drive the ADCs are derived from the 4M signal coming from the GPS card it is made sure that the sampling process does not drift with respect to the GPS time standard.

**Baja processor board and DCU software `dcu_main`** Each DCU contains a Baja processor card manufactured by *Artesyn* [59]. This card runs the software that controls the timing hardware, reads and packages the data from the ADCs and sends the data packets to the datacollector.

After the boot procedure of the hardware the *VxWorks* operating system is loaded from the

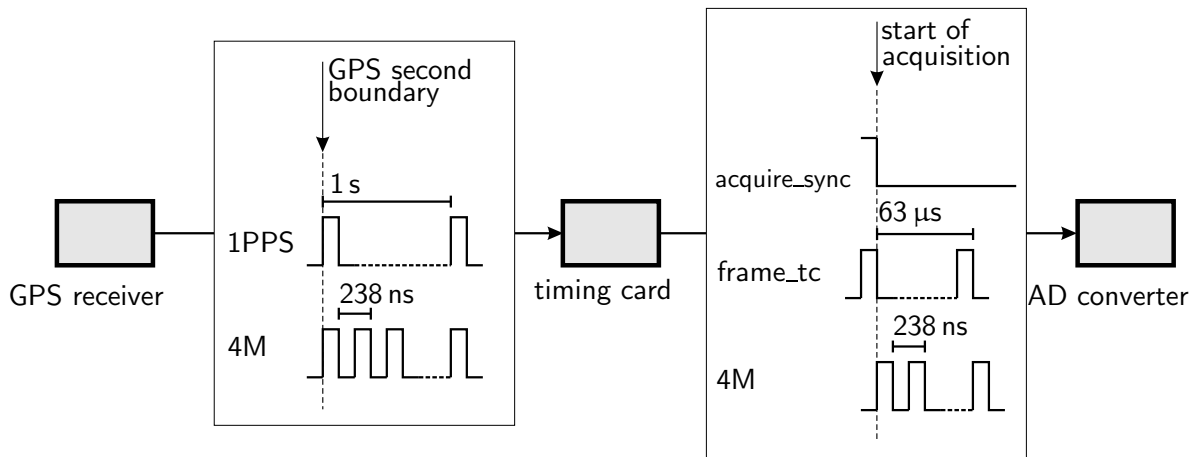


Figure 2.9.: Schematic of the signals controlling the timing of the AD conversion process.

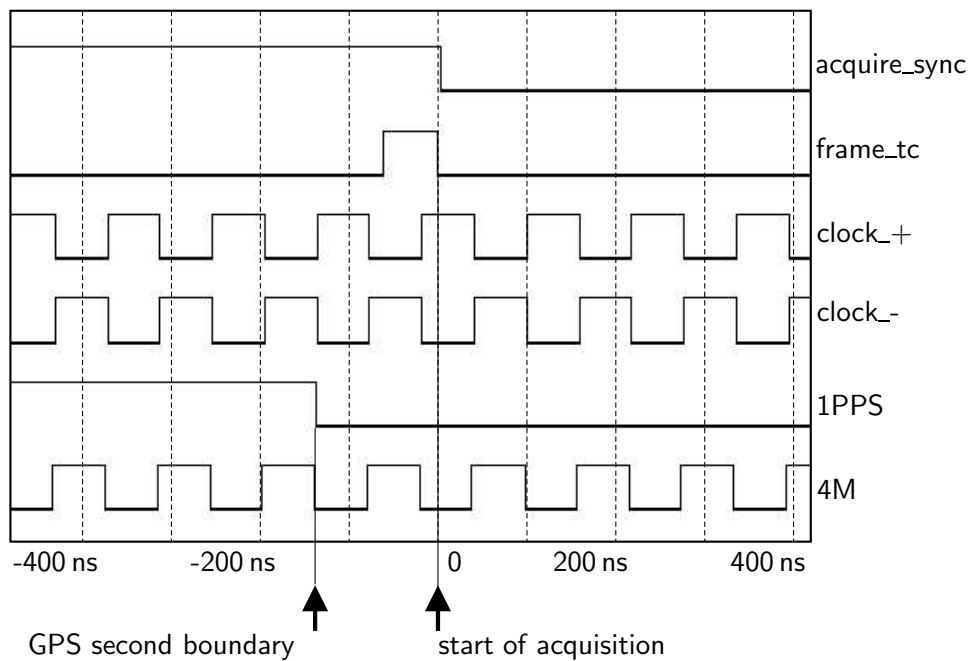


Figure 2.10.: Timing signals measured on the GEO 600 DAQS.

server *morgan*. In addition the card loads and executes the *dcu\_main* software. This program initializes all programmable preamplifiers of the *ICS110B* board with the values defined in the database (see section 2.2.5). The next step is to arm the timing card. In this state the card starts the data acquisition process on the next GPS second boundary indicated by the 1PPS signal coming from the GPS receiver. The internal buffers of the ADC boards containing the sampled data are read out by the *dcu\_main* program and the data are packaged in segments of one second. For each data segment the current GPS second is read from the hardware registers of the GPS receiver and added to the data packet. Each packet is then sent to the DAQS server via the TCP/IP network connection. The software creates a circular buffer in the on-board memory of the processor board that can hold up to 20 seconds of data. This buffer avoids data loss in case the network connection decelerates or is disconnected for a short time. As long as the transmission does not fall behind by more than 20 seconds no data are lost. The *dcu\_main* software starts a server task that listens to incoming connections from the DAQS server. By sending commands to the DCU the DAQS server can reconfigure the programmable preamplifiers during runtime.

#### 2.2.2.2. LabVIEW system, ctrl\_to\_daq-VI

The system controlling the position and alignment of the GEO 600 optics at low frequencies (<10 Hz) is implemented in *LabVIEW*. The various machines controlling the parameters of the system communicate with a *data socket server* on a central machine that has all parameters stored in a *common database*. These values contain important information about the state of the detector and need to be recorded. A *LabVIEW* virtual instrument (VI) called *ctrl\_to\_daq* is requesting the data from the *data socket server* once per second, packages up all available values and sends them to the *datacollector* software where the values are incorporated in the data stream. Generating an individual frame-file channel for each *LabVIEW* control signal would be very inefficient because of the low sampling rate and the large number of available signals. Therefore the more than 1000 signals coming from the *LabVIEW* system are combined into 39 DAQS channels. Figure 2.11 shows a screen-shot of the active *ctrl\_to\_daq*-VI.

#### 2.2.3. Processing the data

The DCUs and the *LabVIEW* *ctrl\_to\_daq*-VI send their data to the *SUN E250* server *morgan* for processing. This server runs the *datacollector* program that accepts network connections for transferring data. The DCUs send the sampled data of all channels at the full sampling rate of 16 384 Hz to this server. The *datacollector* retrieves the configuration of the DAQS from a database and processes the data according to the settings: The channels selected for recording are extracted from the data stream. In addition, low-pass filtering, decimation and reduction of the sampling resolution can be applied. For each channel a signal name is retrieved from the database and assigned to the data before they are written to the disk array connected to *morgan*. In this stage the data are still in a preliminary format and not in the frame format which is the final format used for storage and data exchange.

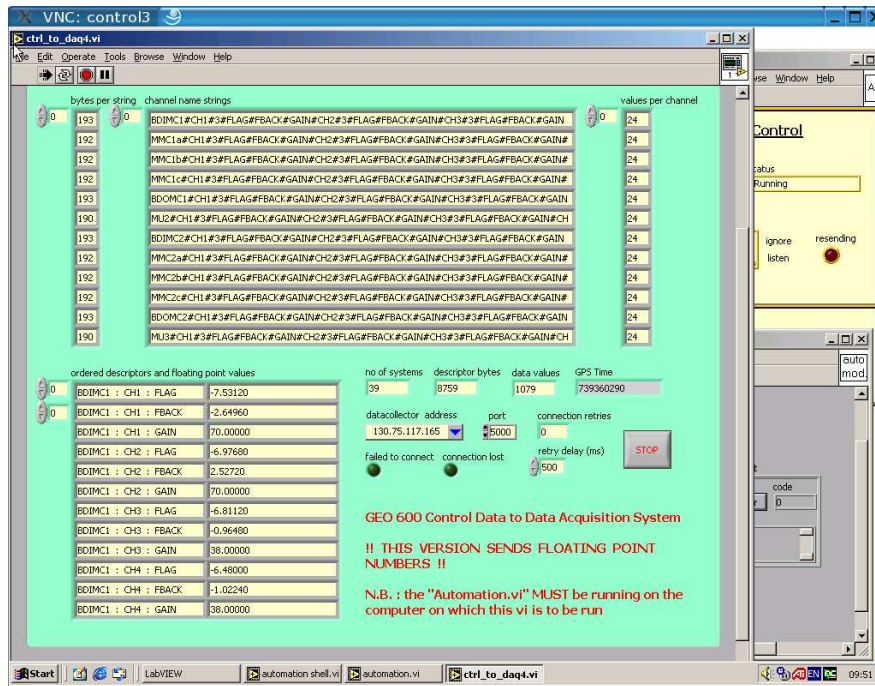


Figure 2.11.: The LabVIEW virtual instrument `ctrlL_to_daq` forwards the data from the LabVIEW control system to the DAQS.

The `datacollector` software analyses channels in the raw data in order to determine the lock status of the laser system, the mode cleaners and the interferometer. The four binary channels `G1:DER_LOCK_SL`, `G1:DER_LOCK_MC1`, `G1:DER_LOCK_MC2` and `G1:DER_LOCK_MID` at a sampling rate of 1 Hz are added to the data stream. A data value of 0 indicates that the corresponding system was unlocked during this second while a value of 1 represents a locked system for the full second. The channel `G1:PSL_SL_PWR-AMPL-OUTLP` is analyzed to determine whether the injection lock of the laser system is working. This channel measures the intensity of the laser beam that is injected into the first mode cleaner. In the unlocked state, the fluctuations of the laser power are much higher than in the locked state. If the standard deviation of the signal is above an adjustable threshold, the injection lock system is considered not to be working. For the lock status of the mode cleaners, the channels `G1:LSC_MC1_VIS` and `G1:LSC_MC2_VIS` are analyzed. These channels measure the visibility of the mode cleaner cavities, i.e. the amount of light from the incident beam that is reflected on the input mirror. In the locked status a large fraction (>90%) of the light is injected into the optical cavity. If the reflected light from a mode cleaner exceeds a given threshold, the mode cleaner is considered to be unlocked. The status of the interferometer can be obtained directly from the locking servo. The microcontroller that manages the locking procedure provides an electronic output that indicates the current lock status. This signal is recorded in the DAQS using the signal name `G1:LSC_MID_LS`. The `datacollector` reads this signal and generates the lock channel `G1:DER_LOCK_MID` from the data.

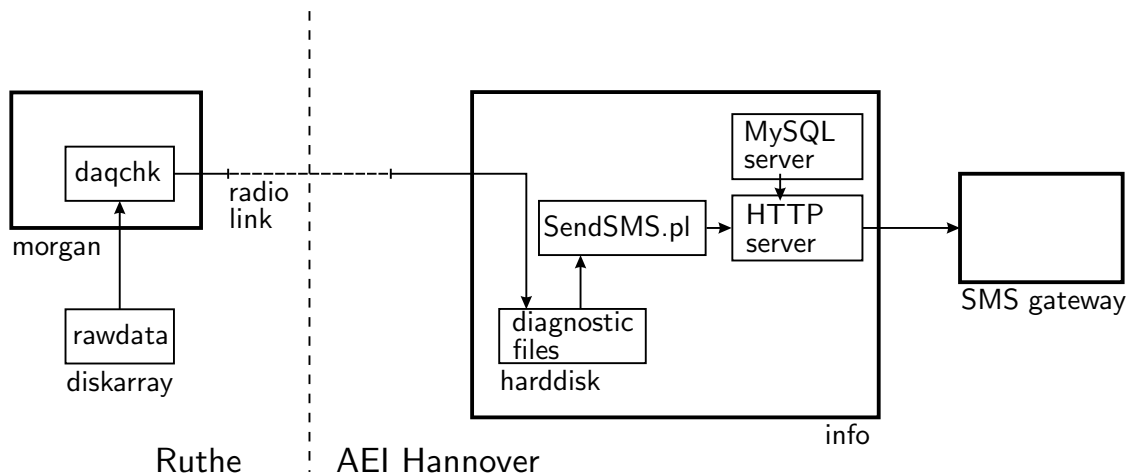


Figure 2.12.: Schematic of the diagnostics system.

The disk space of the hard disk array connected to *morgan* has a capacity of 170 GB and allows storage of about two days worth of data. Old data have to be constantly deleted to create space for the new data that are coming in. The database contains information about the date storage time that is read by the *datacollector*. While writing new data to the disk the software locates and erases data that is older than the maximum storage time. This ensures that the disk array never fills up.

Processing the output channel of the interferometer and generating a calibrated  $h(t)$  channel is done on *morgan* as well [33]. The software dedicated to this task is called *mkhoft*. The program reads the two output channels of the interferometer that contain the differential arm length change. These channels are called G1:LSC\_MID\_EP-P\_HP (P channel) and G1:LSC\_MID\_EP-Q\_HP (Q channel), which are the two quadratures of the interferometer output signal. These channels contain calibration lines that are generated by controlled motion of the east end mirror with a known amplitude at a number of frequencies. The calibration lines in these channels are measured and digital filters created that are applied to the P and Q channel. The filtered channels are then combined to the  $h(t)$  channel which is added to the raw data on the disk array.

#### 2.2.4. Automated monitoring

The GEO 600 DAQS includes self-monitoring that will notify operators about problems with the instrument. A schematic of the system is shown in figure. 2.12.

The program *daqchk* that is running on *morgan* scans the raw data files for selected channels specified in the configuration file "RAWDATA\_DIR/rawdata/log/daqchk\_config.txt". The rms value of each one-second-segment is calculated and compared to a lower and an upper threshold given in the configuration file. For each signal that is being monitored, a corresponding file is created on the machine *info* at the AEI Hannover. Every time a test is passed successfully the time stamp on the corresponding file is updated by the *daqchk* software.

When the test fails, an error message describing the reason for the failure is written to the file and the update of the time stamp is stopped at this point. The timestamps on the files are constantly monitored by a script running on the machine *info*. In case a time stamp falls behind the current time by more than two minutes the content of the file is read and passed to a PHP script of the web server running on the same machine. This script looks up the mobile phone numbers of the current operators of the detector from a local database. These numbers and the text read from the file are passed to a SMS gateway that sends the text to the cell phones of the operators. The system was designed to be robust against failures of the software and hardware. The operators would still be notified in case problems like a crash of the monitoring software occurred, the DAQS server *morgan* failed or the radio link between Ruthe and Hannover went down. As long as the machine *info* is running, the timestamps are being checked and the cell phone numbers of the operators to be notified can be retrieved from the local database.

This system is used to monitor the infrastructure at the site, the interferometer itself and the DAQS. The infrastructure channels being monitored are the voltage of the power grid feeding the uninterruptible power supplies in the central station, the temperature in the air-conditioned areas in the central and end stations and the pressure in the vacuum system. The lock status of the interferometer is checked and an alert is triggered in case it falls out of lock. To detect any problem with the DAQS the “RAWDATA\_DIR/rawdata/log/DCU\_NAME\_current.log” files are read by the *daqchk* software. They contain the GPS timestamps of the most recent data sent by each DCU. By comparing the timestamps with the current time it can be checked whether the data transfer from any of the DCUs has fallen behind. An alert is triggered in case a DCU is behind by more than its internal buffer-length which means that data are being lost. The timing of the acquisition process is checked by monitoring a signal from an external reference clock which is connected to the central station DCU. In addition each DCU records a test channel with a known DC voltage. The DAQS showed failure modes where the signals connected to the system appeared in the wrong channels. There was also a failure mode where the channels were contaminated with the additional noise. Both failure modes can be detected by monitoring the rms value of the DC test channel.

In summary, the self diagnostic system can detect a wide range of potential problems with the GEO 600 detector. By automatically notifying operators, the response time to these problems is minimized so that the down-time of the instrument is as low as possible.

### 2.2.5. Configuring the system

The configuration of the DAQS is stored in a MySQL database called *daqsql* kept on the machine *morgan*. By sending SQL commands to the database management system, configuration changes of the DAQS can be applied. Operators don't have to interact directly with the database which would require knowledge of SQL and of the internal structure of the database. Instead they can use a web browser to connect to an interface that is running on the HTTP server *info*. The interface is implemented as a set of PHP scripts that assemble the corresponding SQL statement from the user input and submit it to the database. All write operations to the database require the user to authenticate first by specifying a username and



Authentication OK - User: kbk (Karsten Koetter) connected from 130.75.117.55 Current UTC Time: 2003-10-15 14:48:11

**Current DAQS Configuration**

Navigation  
GEO600 Info Server - Home  
Access control  
Logout  
Change Your Password  
User Management  
GEO600 Self Diagnostics  
Assign Shifts  
Setup Monitoring  
Detector  
Set LockStatus Thresholds  
LockStatus / Statistics  
Current Detector Status  
Lookup Detector Status  
Setup  
Change Detector Status  
DAQ System  
Current DAQS Configuration  
Lookup DAQS Configuration  
Current DCU/ADC Setup  
DAQS Diagnostics  
Configure DAQ System  
Setup DAQS Hardware  
Data Storage Management  
Signals  
Show Signal List  
Lookup Signal Description  
Add Signal Description  
Add Signal Name  
Modify / Delete Signal  
Calibration  
Lookup Calibration Function  
Add Calibration Function  
Modify Calibration Function  
Mark Calibration Function Outdated  
Lookup IIR Time Domain Filter  
Add/Modify IIR Time Domain Filter  
Tools  
Time Conversion  
Environmental Monitor  
DataViewer

created by  
Karsten Koetter  
Karsten.Koetter@aei.mpg.de

Data rate

Data rate	Bytes/s
357,760	Bytes/s
2,962,080	bits/s
21,465,600	Bytes/min
30,810,464,000	Bytes/day

DAQS status at 2003-10-15 14:48:11 (UTC) - 750264504 (GPS)

DCU	ADC	Channel	last modified (UTC)	Rec	Signal	Sampling		LPF	Gain (dB)	Calibration		Connected By	Comment
						Rate (Hz)	Resolution (bit)			Sys	DWF		
alchemist	ICS - 32 channels	1	2003-06-24 15:19:25	On	G1.LSC_MID_EP-P	1024	16	Y	0	new	view	martin (Martin Hewitson)	FOR DETECTOR DIAGNOSTICS
alchemist	ICS - 32 channels	2	2003-08-11 11:30:32	On	G1.SEI_TCC_ST52x	512	16	Y	0	N/A	N/A	hrq (Hartmut Grote)	FOR DETECTOR DIAGNOSTICS
alchemist	ICS - 32 channels	3	2003-09-05 08:25:13	Off	-	-	-	-	-	-	-	hrq (Hartmut Grote)	Connected through A3 on attenuator patch panel.
alchemist	ICS - 32 channels	4	2003-03-04 13:36:42	On	G1.LSC_MIC_VIS	2048	16	N	-8	new	view	hrq (Hartmut Grote)	FOR DETECTOR DIAGNOSTICS
alchemist	ICS - 32 channels	5	2003-03-04 13:39:59	On	G1.LSC_PWR_E+N	2048	16	N	-8	N/A	N/A	hrq (Hartmut Grote)	FOR DETECTOR DIAGNOSTICS
alchemist	ICS - 32 channels	6	2003-03-04 13:41:06	On	G1.LSC_MID_VIS	2048	16	N	-8	new	view	hrq (Hartmut Grote)	FOR DETECTOR DIAGNOSTICS
alchemist	ICS - 32 channels	7	2003-09-25 18:19:03	On	G1.LSC_MID_FP-MCEI-MCNI	512	16	N	0	new	view	martin (Martin Hewitson)	FOR DETECTOR DIAGNOSTICS
alchemist	ICS - 32 channels	8	2003-03-04 13:54:02	On	G1.LSC_MID_FP-MCEI-MCN	2048	16	N	-8	new	view	hrq (Hartmut Grote)	for debugging detector
alchemist	ICS - 32 channels	9	2003-03-13 15:52:40	On	G1.LSC_SRC_EP-P	2048	16	N	0	N/A	N/A	hrq (Hartmut Grote)	debugging detector
alchemist	ICS - 32 channels	10	2003-03-04 13:57:43	On	G1.LSC_SRC_FP-MSR	2048	16	N	-8	N/A	N/A	hrq (Hartmut Grote)	debug detector
alchemist	ICS - 32 channels	11	2003-08-11 11:36:43	On	G1.SEI_TCC_ST52y	512	16	Y	0	N/A	N/A	hrq (Hartmut Grote)	debug detector
alchemist	ICS - 32 channels	12	2003-08-11 11:49:58	On	G1.SEI_TCC_ST52z	512	16	Y	0	N/A	N/A	hrq (Hartmut Grote)	debug detector
alchemist	ICS - 32 channels	13	2003-03-04 14:04:15	On	G1.LSC_MID_EP-debug	2048	16	N	-8	N/A	N/A	hrq (Hartmut Grote)	debug detector
alchemist	ICS - 32 channels	14	2003-10-01 15:52:43	On	G1.LSC_SR_FREQ-RAMP	2048	16	N	-8	N/A	N/A	hrq (Hartmut Grote)	used for 2f detector
alchemist	ICS - 32 channels		2003-10-06									bal (Harald)	

Figure 2.13.: HTTP interface for configuring the DAQS.

password. Several privilege levels can be specified for each user.

The interface can be used to submit any changes in the DAQS to the database. The basic setup of the system includes specifying the hardware configuration of the DCUs. Each ADC board can be used in any of the DCUs. The current configuration is retrieved from the database table *adc\_log* which can be updated via the interface. Configuring each individual channel the DCU is done by writing the settings into the *channel\_log* table. The current or any past configuration of the DCUs and the individual channels can be looked up in the database and shown on a HTML page. It is also possible to search the database for time stretches when specific signals were recorded in any of the channels. The storage time of both the raw data and the frame data is kept in the table *storage\_management*. This table is queried by the *datacollector* and the *framemaker* to to configure the automatic deletion of old raw data and frame files. The HTTP interface calculates and displays the maximum possible storage time from the current data rate and the disk size. This prevents the user from submitting settings to the database that would fill up the entire disk space with raw

data or frame files. The self-diagnostic software *daqchk* can be configured via the interface as well. The monitoring of each channel can be switched off and the telephone numbers can be selected that will be used for sending the SMS alert messages.

The HTTP server can also read the log files that are generated by the *datacollector*, the *framemaker* and the trendmakers. The diagnostic information contained in these files is presented as a HTML page shows the most recent timestamp of the data coming from the DCUs, the progress of the *framemaker* and the trend data makers and the files that log the error messages.

Additional information about the signals connected to the DAQS can be obtained by downloading signal description documents from the server. For each signal connected to the DAQS, a document describes the corresponding sensor and the characteristics of the signal. The interface can be used to upload, search and retrieve these documents.

The DAQS records signals from sensors that measure a variety of physical quantities (displacement, light power, magnetic field, etc.). Since the recorded signal is always a voltage, a calibration function is required to convert the signal into the physical quantity that was actually measured by the sensor. These calibration functions are also stored in the database *daqslog*. The table *calibration* contains the parameters of the calibration functions in the frequency domain. For each filter, a list of poles, zeros and a gain factor is stored. In addition, IIR filters can be added to the table *IIR\_filters*. These filters can be used for time domain filtering of the data. The HTTP interface can read text files generated by *LISO* [39] which is commonly used to create IIR filters from analog prototype filters. Sets of filter coefficients can be added for various sampling frequencies.

For accessing data directly from frame files the HTTP interface offers a convenient way of converting the GPS timestamps in the filenames to UTC time and vice versa.

The interface can also display graphs with both time and frequency domain data directly in the web browser. This is done with the *DataViewer* that is described in section 2.2.7.5.

## 2.2.6. Data format and storage

The final data format of the GEO 600 detector is called *frame format* [38]. This format is used throughout the whole gravitational wave community for data storage and handling. A *SUN E250* server in Hannover runs a software task called *framemaker*. This program is based on the C-version of the *FrameLibrary* [64] which is maintained by the VIRGO group. The *framemaker* program accesses the raw data stored on the GEO 600 site and converts them to frame files. Each file contains 60 one second frames. These files are written to a disk array in Hannover and stored in a hierarchical directory structure in the form YYYY/dayDDD/hourHH/G-R-GGGGGGGG-60.gwf. YYYY is the year, DDD is the day of the year, HH the hour of the day and GGGGGGGG the GPS second of the first second of data in the file. While writing files to the disk array the software takes care of erasing old data at the same time so that the disk never fills up. The storage time of a frame file is retrieved from the *daqslog* database once per minute.

In addition to the files written by the *framemaker*, two additional sets of frame files are generated. These files contain data at reduced sampling rates and are called *trend frame files*. The program *mkhourtrend* generates the *hour trend files*. For every channel, these files contain the minimum, maximum, average and rms value of each second. An hour trend file contains one hour worth of data broken down into 60 frames. The sampling rate of the contained data is 1 Hz. The software generating the *day trend files* is called *mkdaytrend*. The files contain the values mentioned above for each minute of data. Each file contains one day worth of data broken down into 24 frames. The sampling rate is 1/min.

Long term trends of a channel can be displayed very quickly using these files. Compared to the data at the full sampling rate, the volume is reduced by a factor of about 20 in the hour trend files and by an additional factor of 50 in the day trend files.

## 2.2.7. Data access

### 2.2.7.1. Raw data / LabVIEW oscilloscope-VI

The raw data server *mrawserver* running on the machine *morgan* gives access to the data almost in real-time. The server listens to incoming TCP/IP connections on port 8000. Client software can send commands to this port to request data from any of the recorded channels. The data are made available on the server less than two seconds after it was sampled. Up to one second of delay is introduced by the DCU waiting for a full second of data being collected by the ADC so that a one second data segment can be sent to the *datacollector* program. A maximum of one additional second is required to process the incoming data on the server and write the data to disk. Once the data are available on disk the log file indicating the most recent data segment is updated and the data can be retrieved from the raw data server.

One application that makes use of the raw data server is a virtual instrument called *oscilloscope* implemented in *LabVIEW*. As the name suggests the VI emulates the functionality of an oscilloscope and a spectrum analyzer. Data of up to four channels can be simultaneously displayed in the time or frequency domain. All basic functions of laboratory instruments are available in the virtual instrument. The functionality includes triggering, markers in the display and adjustable scaling of the time and amplitude axis. Figure 2.14 shows a screen shot of the *oscilloscope* VI.

### 2.2.7.2. Local frame files

The most basic way of accessing GEO 600 data is to read them from frame files that are present on a local disk. Most data analysis environments (Matlab, GEO++) can import data that are available as local frame files. For data analysis tools that process a large number of channels, this is a very efficient way to access data. The GEO 600 online data analysis running on the Hannover Beowulf cluster is getting the input data from frame files. A dedicated network link is used to copy all frame files from *aspect* to the local disk of the cluster.

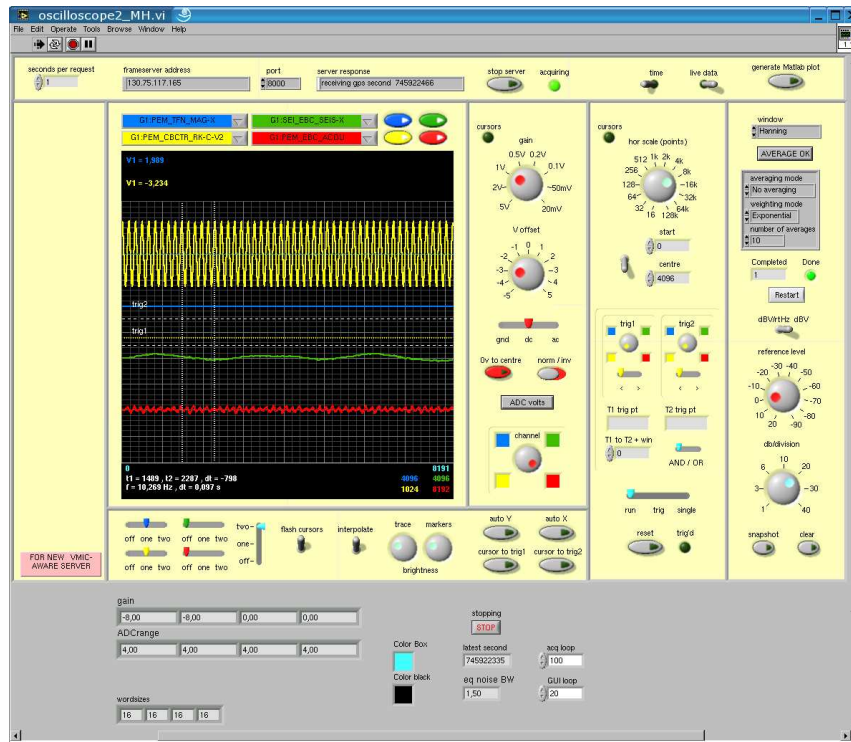


Figure 2.14.: LabVIEW oscilloscope virtual instrument for near real-time data access.

### 2.2.7.3. Frame server

For many data analysis tasks, only a small fraction of the channels included in a frame file is required. Therefore, it is inefficient to transfer the complete frame file to a local machine and then read only a small portion of the content. This problem was addressed by setting up a server program on *aspect*. This machine has access to the three most recent days of data stored on the local disk array. The server listens to incoming connections on a TCP/IP port in the range between 9000 and 9010. Client programs can connect to this port and request data from individual channels. The server can send data at the full sampling rate and both types of trend data. In addition, the time stamp of the latest available data segment can be requested and calibration information stored in the *daq slog* database can be sent. When a corresponding IIR calibration filter is available in the *daq slog* database, the frameserver can send data that are already calibrated.

A client program exists for Matlab (see section 2.2.7.4) and there is a HTML based *DataViewer* (section 2.2.7.5) for displaying data from the frame server.

### 2.2.7.4. Accessing data in Matlab

Matlab is a tool that is widely used in the analysis of GEO 600 data. Frame files stored on the local disk of a machine can be read in using the software *FrExtract* that is included in

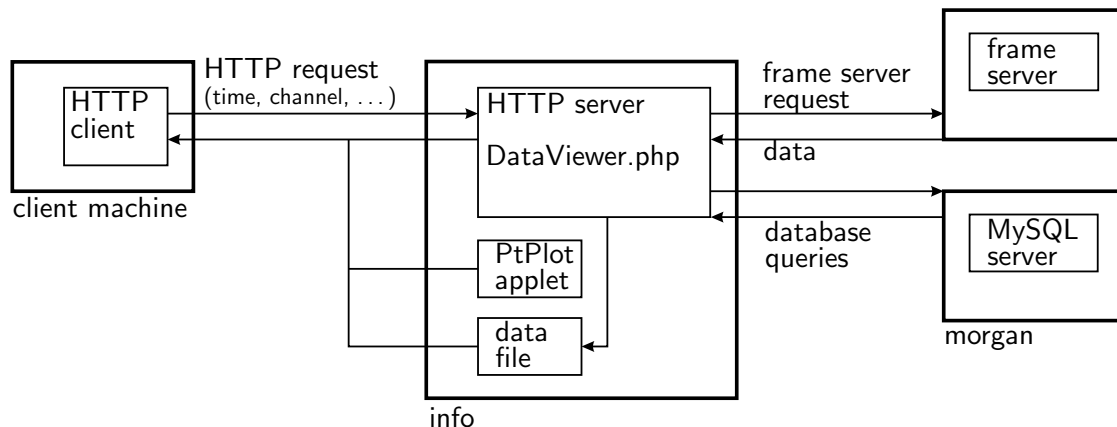


Figure 2.15.: Schematic of the *DataViewer* that allows to display GEO 600 data in a Web browser.

the *FrameLibrary*. Data from a frame server can be retrieved by invoking the client program *m2fserve* which is part of the *geotools* [74] package. In addition to data at the full sampling rate, the client can retrieve trend data and calibration information. Data from a raw data server can also be used in Matlab. This is done via the *m2dserv* client.

### 2.2.7.5. DataViewer

The *DataViewer* is a tool that allows plotting GEO 600 data in a web browser. For displaying a graph no additional software is required on the client machine. The *DataViewer* software is implemented as a PHP script on the HTTP server *info*. By requesting the URL <https://info.geo600.uni-hannover.de/GEOSstatus/DataViewer> a form is displayed where the desired plot parameters can be entered. All data streams (data at the full sampling rate, trend data and data from the *LabVIEW* control system) can be used for generating time domain plots. Data at the full sampling rate can also be displayed in the frequency domain with customizable frequency resolution, window functions and data averaging.

A schematic of the data flow between the web browser, the HTTP server and the frame server can be seen in figure 2.15. The *DataViewer* software retrieves the data from a frame server that can be specified by the user. Additional information about the signal is requested from the *daq slog* database. The data and the formatting options for the plot are written to a file that is accessible via the HTTP server. Visualization of the data on the client machine is done using a JAVA applet called *ptplot* provided by the Ptolemy Project [71]. The HTTP server sends a HTML document to the client containing a link to the JAVA applet and to the data file. The web browser loads the applet and the data from the HTTP server and displays a zoom-able plot of the data as it can be seen in figure 2.16.

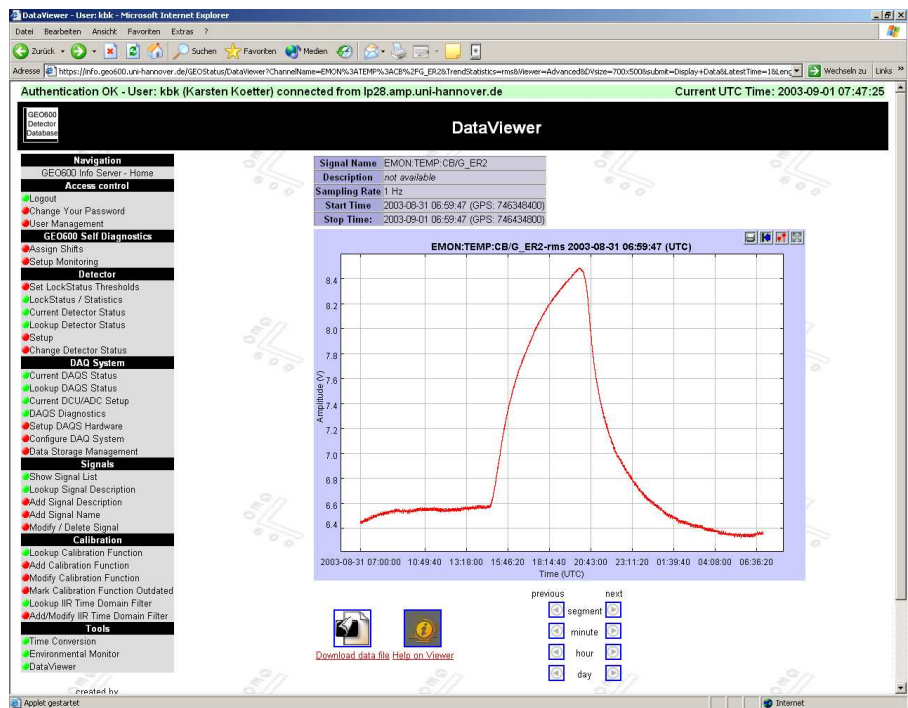


Figure 2.16.: Screen shot of a plot generated with the DataViewer.

## 2.3. Measurements

### 2.3.1. Timing accuracy of the sampling process

The following section describes the tests done for validating the timing accuracy of the sampling process. This test is important because a number of search algorithms for gravitational wave signals (coincidence analysis, targeted pulsar searches, etc.) rely on accurate time stamping of the data. Tests were done on the current system to measure the absolute timing offset and the timing jitter against an external reference clock. All measurements were done with the 37 sample gate delay (see section 2.2.2.1) of the *ICS110B* board removed by the software running on the DCU.

#### 2.3.1.1. Checking the GPS second labels on the data segments

The question of whether or not the data are correctly time-stamped on a one-second time scale was answered with a simple test: A signal (one cycle of a triangular wave at the start of each GPS second) was manually unplugged and re-plugged in the middle of a second using a DCF77 [62] clock as reference. It was then checked in the data whether the signal disappeared in the correct data segment. The result, given in figure 2.17, shows that the time stamps are correct, both for unplugging and re-plugging the signal.

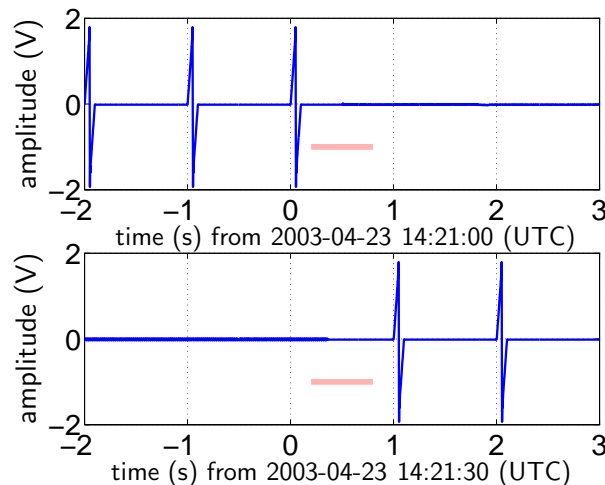


Figure 2.17.: The test signal was unplugged between 14:21:00 and 14:21:01 and re-plugged between 14:21:30 and 14:21:31. The plot shows this behavior as it appears in the data stream. The red segments (horizontal bars) represent the uncertainty in the time of unplugging and re-plugging the signal.

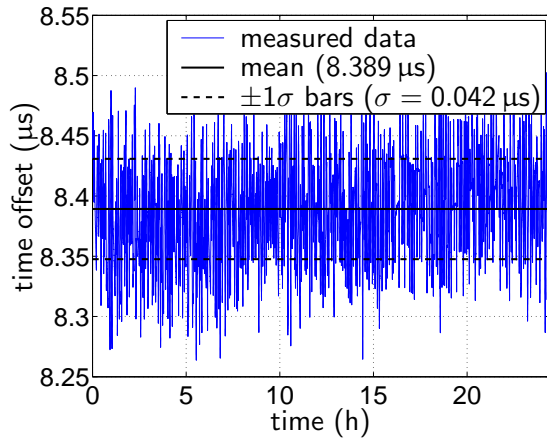


Figure 2.18.: Comparison of the 1PPS signals of the external Rb/GPS clock and the GPS clock of the DAQS over a period of 24h. On average the 1PPS from the external clock was  $8.389 \mu\text{s}$  late compared to the GPS clock of the DAQS.

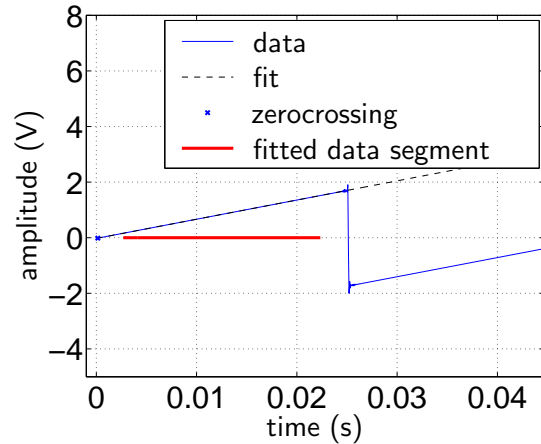


Figure 2.19.: The injected ramp as it appears in the data stream. Also shown is the linear fit (dashed line) that was made to the data segment marked by the red horizontal line.

### 2.3.1.2. Measuring the residual offset and jitter against an external time reference

In the experiments described below the timing of the sampling process was compared against an external timing unit consisting of a Rubidium atomic clock locked to a GPS receiver for long term stability. Like the GPS card used for the DAQS this device generates a 1PPS signal that marks the start of a GPS second.

The first step was to compare the external timing unit and the GPS clock of the DAQS directly. A *SR620* frequency counter was set up to measure the time difference between the 1PPS signals from the two clocks. The result of a measurement over 24 hours can be seen in figure 2.18. It shows that the 1PPS signal from the Rb/GPS clock was on average  $8.389 \mu\text{s}$  late compared to the signal from the GPS card of the DAQS. The standard deviation of the measured offset is  $42 \text{ ns}$ . Lacking a better timing standard than the GPS it was not possible to attribute the  $8.4 \mu\text{s}$  offset to one of the clocks. All further measurements are related to the GPS second boundary indicated by the DAQS GPS clock. The measurements done with the Rb/GPS clock were corrected for the  $8.4 \mu\text{s}$  deviation.

To test the timing accuracy of the DAQ system we injected a test signal into one of the DAQ channels. A schematic of the test setup is shown in figure 2.20. The external timing unit generated a trigger signal (1PPS) at the start of each GPS second. This signal was fed into an *HP33120A* signal generator that produced a digitally synthesized ramp with an amplitude of  $1.7 \text{ V}$  on each trigger event. The ramp signal was then injected into a DAQ channel. A linear fit was made to the ramp as it appears in the data. By calculating the intersection of the fitted line with the zero level of the signal, the start of the ramp indicating the GPS second boundary could be determined to a precision much better than the sampling interval. In figure



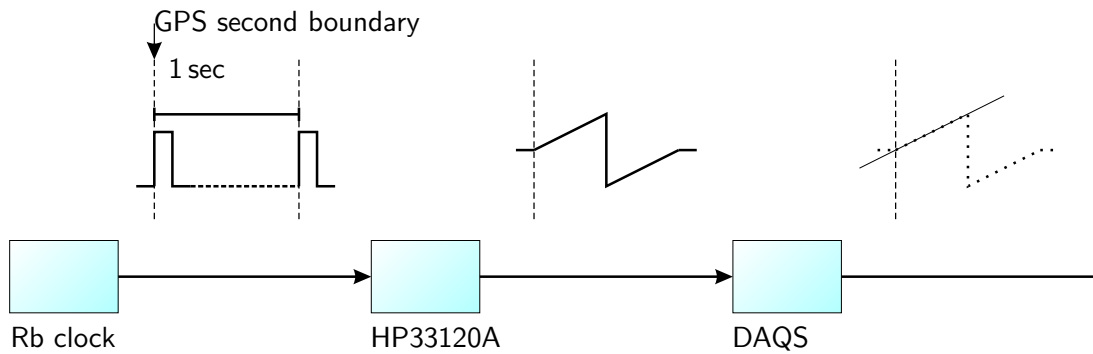


Figure 2.20.: Setup for determining the DAQS timing accuracy.

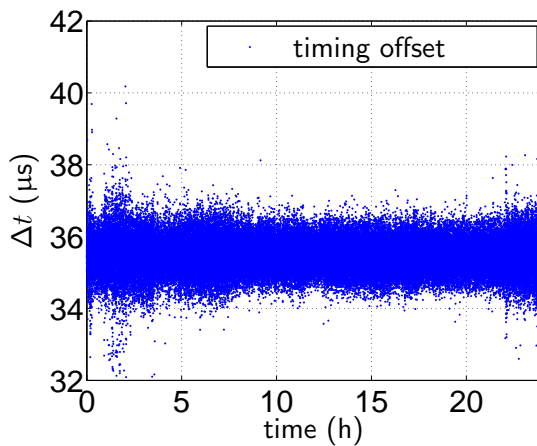


Figure 2.21.: A time series of the timing residuals of the current DAQ system taken over 24 hours in the good state. This is for an injected ramp length of 5 ms.

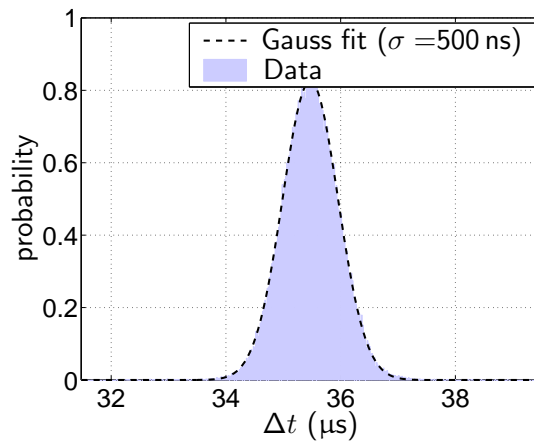


Figure 2.22.: A histogram of the timing offsets taken over 24 hours (5 ms ramp length). The mean is around 35  $\mu\text{s}$ , this is partly due to the measurement method.

2.19 the ramp signal recorded in the DAQS can be seen with the linear fit superimposed on the plot. Ideally the intersection point would be exactly at the beginning of each one-second data segment. However an offset  $\Delta t$  between the intersection point and the beginning of the data segment was observed. The values for the measured offset over a 24 h period is shown in figure 2.21. A histogram of the measured offset values can be seen in figure 2.22. For this experiment a ramp length of 5 ms was used. The distribution of the offsets is Gaussian with a standard deviation of 500 ns. The mean value was 35.5  $\mu\text{s}$  and all measured values lay between 29.6  $\mu\text{s}$  and 40.2  $\mu\text{s}$ .

We also observed that the measured offset and the jitter were both dependent on the length of the ramp signal that was used. Figures 2.23 and 2.24 show the first segment of the ramp signal for different ramp lengths. It can be seen that the zerocrossing of the line fitted to the ramp data have a systematic offset that grows with increasing ramp length. This is an artifact of the digital signal generator used for the experiment. A shorter, steeper ramp makes the

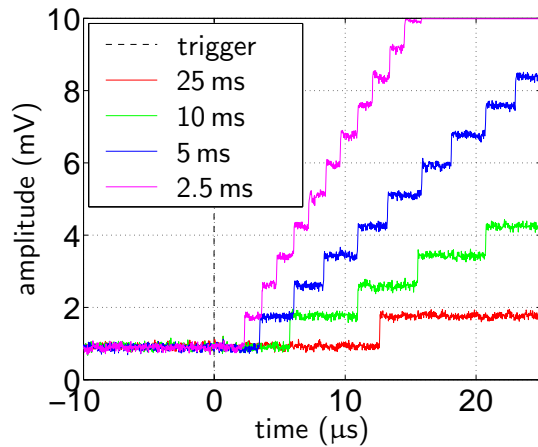


Figure 2.23.: Ramp signals produced by *HP33120A* signal generator. Due to the digital synthesis the signal looks like a staircase on the mV scale.

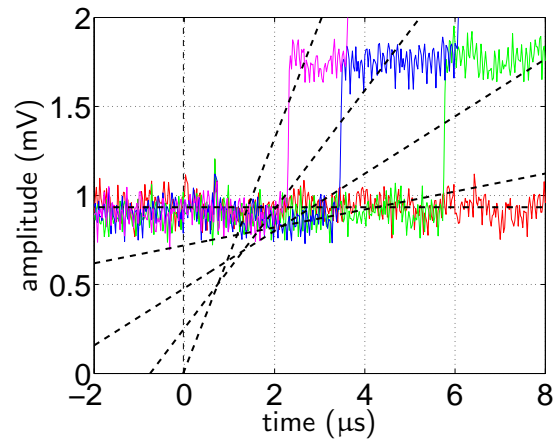


Figure 2.24.: Systematic offset of ramp start time is proportional to ramp length, trigger time is at  $t=0$

measurement less susceptible to errors due to amplitude noise leading to an error in the slope estimation: The steeper the ramp, the smaller the deviations of the measured zero crossing for small fluctuations about the mean slope of the ramp.

To separate the effects of our analysis from the timing offset and scatter inherent to the DAQ system, we repeated the above analysis with different ramp lengths. Figure 2.25 shows a plot of the mean measured offset versus injected ramp length. A linear fit to the data allows us to extrapolate the value for an infinitely short ramp. From the fit we determine the residual timing offset of the DAQ system to be  $15.89 \mu\text{s}$  with the initial 37 samples gate delay removed. The offset is smaller than half the sample time ( $\frac{1}{2} \frac{1}{16384 \text{ Hz}} \approx 30.5 \mu\text{s}$ ), and therefore cannot be decreased by shifting the data by an integer number of samples. Algorithms exist that can shift the data by a fraction of a sample so that this known and constant  $15.89 \mu\text{s}$  offset can be removed if required. This is not done by the DAQS software but left for posterior data conditioning.

Figure 2.26 shows a plot of the standard deviation of the offset measurements for each ramp length. Again we can extrapolate the value for an infinitely short ramp and see that the standard deviation  $\sigma$  in the measured offset due to timing fluctuations is  $\approx 63 \text{ ns}$ .

### 2.3.1.3. Timing across reboots

Figure 2.27 shows the timing offsets during a period when numerous hardware and software reboots have been performed for test purposes. The DAQS can be rebooted in two different ways. A hardware reboot (type I) means recycling the power to the full DAQ crate. A software reboot (type II) is performed using the interface software supplied with the processor board – here the processor board operating system is rebooted and the DAQ code is run from the

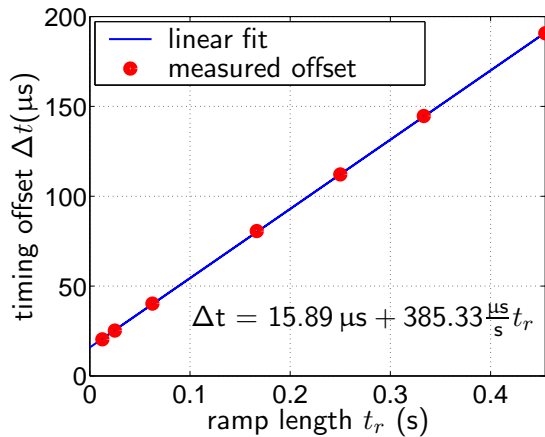


Figure 2.25.: A plot of mean measured offset versus injected ramp length. A linear fit to the data allows extrapolating the offset at zero ramp length.

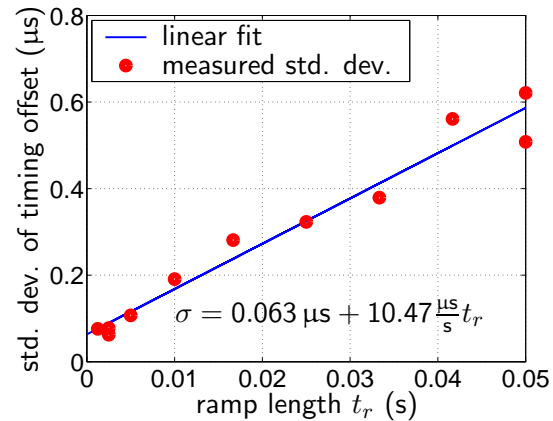


Figure 2.26.: A plot of the standard deviation  $\sigma$  of each set of 1500 offset measurements against the length of the ramp signal. A linear fit to the data allows to extrapolate the value of  $\sigma$  at zero ramp length.

start. During type II reboots, the power to the cards in the DAQ crate is maintained. The results presented in figure 2.27 show type I and type II reboots. The length of the injected ramp was 50 ms. Here we can see that a type II reboot causes a shift in the absolute timing offset of about 2300  $\mu\text{s}$ . This value corresponds to the gate delay (see section 3.3.1) of 37 samples inherent to the ADC board:  $\frac{37}{16384} \text{ s} \approx 2258 \mu\text{s}$ .

The FIFO interrupt handler of the *ICS110B* ADC board does not behave in the same way as after a hardware reboot. Data are read from the *ICS110B* on board FIFO every time the FIFO-half-full interrupt fires. After a software reboot, the routine that waits for a FIFO-half-full interrupt does not respond correctly on the first call of the function (although this is not the case on a hardware reboot). Calling the function a second time in the start-up procedure seems to work and there are no problems in all subsequent calls. Although this is not necessary on a hardware reboot, it has no adverse effects so the routine is now rewritten to include a second call to this function in the start up section of the code that removes the gate delay. This fixes the problems seen with type II reboots.

#### 2.3.1.4. GPS frequency lock servo

Figure 2.28 shows the timing offset after the DAQS hardware was power cycled. It turned out that the timing offset deviates by up to 3  $\mu\text{s}$  from the final value during the first ten minutes after the GPS card was powered up. This effect is caused by the servo on the card that phase locks the internal oscillator of the card to the GPS signal. It takes approximately ten minutes until the frequency of the internal oscillator settles at the final value.

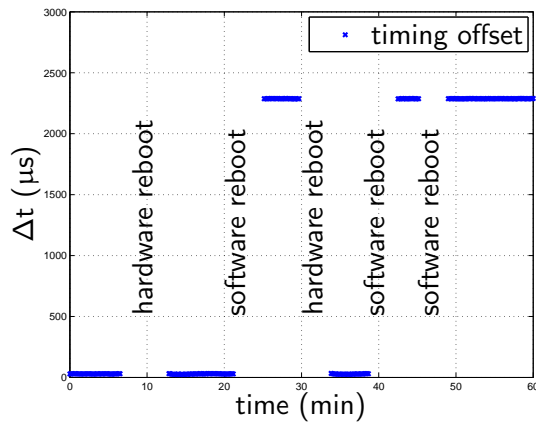


Figure 2.27.: A time series plot of the timing residuals during hardware (type I) and software (type II) reboots.

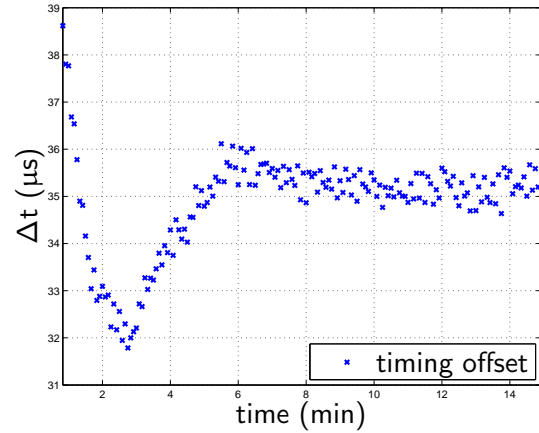


Figure 2.28.: After the GPS card is power cycled it takes about 10 minutes until the frequency of the output signal settles to its final value.

### 2.3.2. Filtering

The ADCs employed in the GEO 600 DAQS have fixed sampling rates of 16 384 Hz (*ICS110B* board) and 512 Hz (*VMIC* board). Many signals have a lower bandwidth than the Nyquist frequency of the ADC they are connected to. These signals can be decimated to a lower sampling rate  $f_{sr_d}$  by the *datacollector* software to save transmission bandwidth and storage capacity. As decimation factor all powers of two between 2 and 256 can be chosen.

Before the data are decimated it can be passed through a digital low pass filter. To avoid aliasing this is required for signals that have an unwanted frequency content above  $f_{sr_d}$ . The filter is a 6-pole Butterworth filter with a cut-off frequency at 30% of the target sampling rate  $f_{sr_d}$ . The performance of the digital filters were measured by connecting a white noise signal from a signal generator to two channels of the *ICS110B* board. One of the channels was set to the maximum sampling rate without any filter applied to the data. The other channel was passed through the digital low-pass filter, but decimation was switched off. The transfer function of the filter could be determined by dividing the complex spectra of both channels and taking the average. Figure 2.29 to 2.36 show the transfer functions of these filters. It can be seen that the filters for all decimation steps match the design shape of the transfer function. For the data from the *VMIC* board the same filters are being used to decimate data from 512 Hz down to sampling frequencies as low as 2 Hz.

### 2.3.3. Noise level

The following measurements were done to determine the noise floor of the DAQS. The *ICS110B* board employs CS5396 AD converter which have a nominal sampling resolution

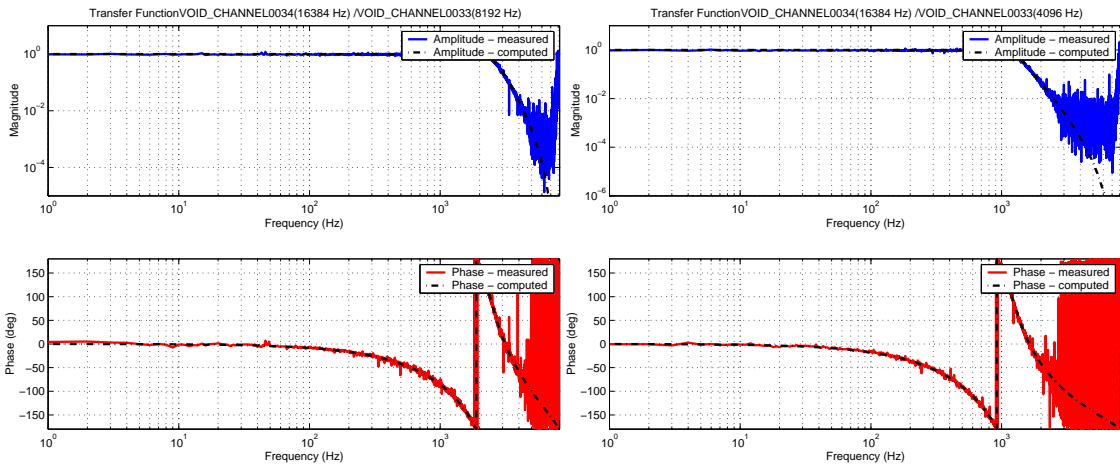


Figure 2.29.:  $f_{sr_d} = 8192$  Hz

Figure 2.32.:  $f_{sr_d} = 4096$  Hz

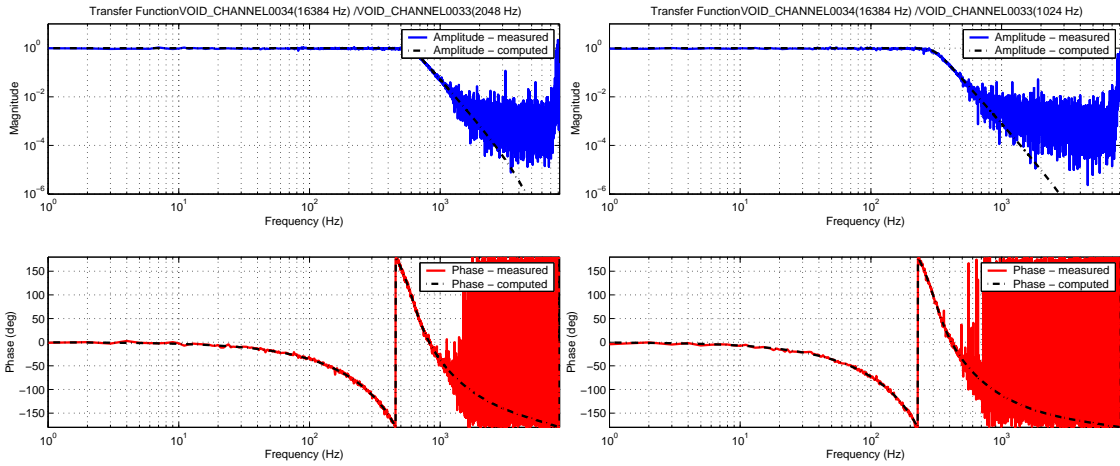


Figure 2.30.:  $f_{sr_d} = 2048$  Hz

Figure 2.33.:  $f_{sr_d} = 1024$  Hz

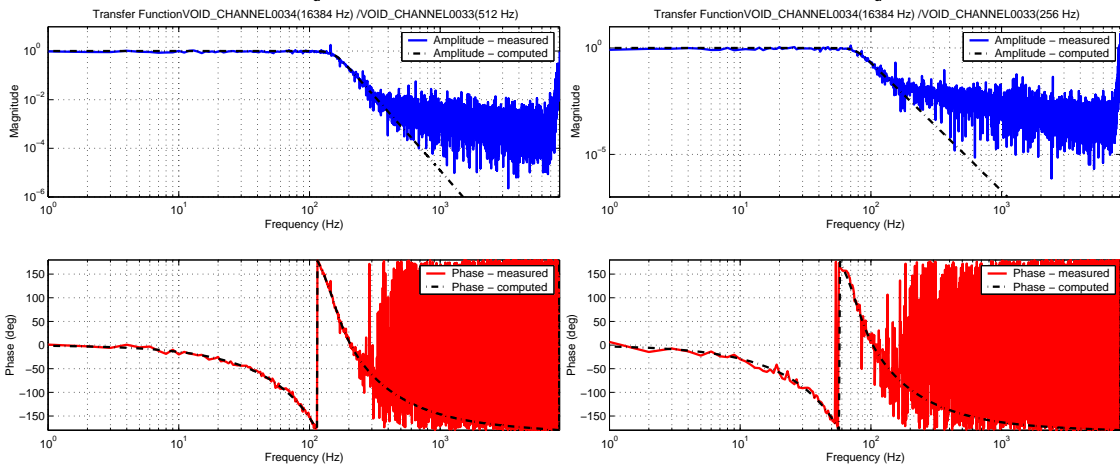


Figure 2.31.:  $f_{sr_d} = 512$  Hz

Figure 2.34.:  $f_{sr_d} = 256$  Hz

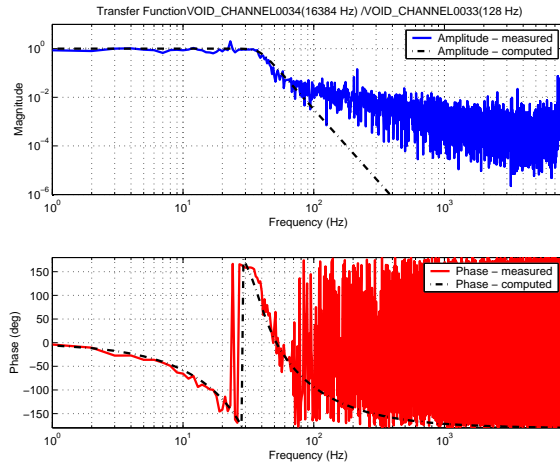


Figure 2.35.:  $f_{sr_d} = 128$  Hz

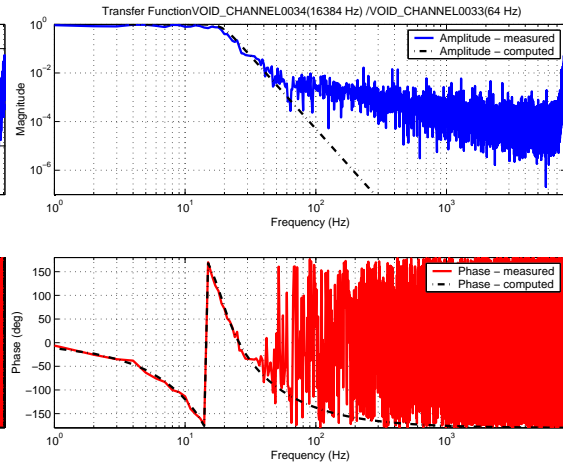


Figure 2.36.:  $f_{sr_d} = 64$  Hz

of 24 bit. The input signal range of the converter is  $\pm 2$  V so that the quantization steps are 238 nV. This leads to a quantization noise of  $\frac{238 \text{ nV}}{\sqrt{6 \times 16384 \text{ Hz}}} = 760 \frac{\text{pV}}{\sqrt{\text{Hz}}}$  (see section B) at a sampling rate of 16384 Hz. The expected noise level is higher than this limit because electronic noise will contribute to the overall noise level. The data sheet of the *CS5296* claims that the converter has a dynamic range of 120 dB which corresponds to 19.9 bit resolution.

Measuring the amplitude spectral density of the ADC output with the input pins connected to ground potential would not reveal all potential noise sources. For example, a non-linearity in the conversion process is not observed as long as no signal is connected to the input. Therefore, a sine wave with a frequency of 47 Hz and an amplitude of 25% of the dynamic range of the ADC was connected to the DAQS for the measurement. The black trace in figure 2.37 shows the measured amplitude spectral density of the signal as it appears in the data of an *ICS110B* channel. It can be seen that the noise floor is significantly higher than the 24 bit quantization noise level (blue trace). The noise cannot be attributed to the ADC without ruling out the possibility that the noise level observed was already present in the input signal. Therefore a low pass filter with 4 poles at 100 Hz was applied to the input signal in all following experiments. The red trace is the measured amplitude spectral density multiplied by the filter transfer function. This curve is an upper limit for the noise level of the filtered input signal. It can be seen that it is below the 24 bit quantization noise limit for frequencies above 100 Hz.

To check the influence of the programmable preamplifier stage on the noise level the measurement was carried out with three different gain settings. Figure 2.38 shows the measured amplitude spectral densities of the data when the filtered signal from the *HP33120A* was connected to the input. The measurement was repeated for different gain settings. The signal shown is the input referred noise, i.e. the numbers produced by the ADC were converted back to the corresponding voltage level at the input of the preamplifier.

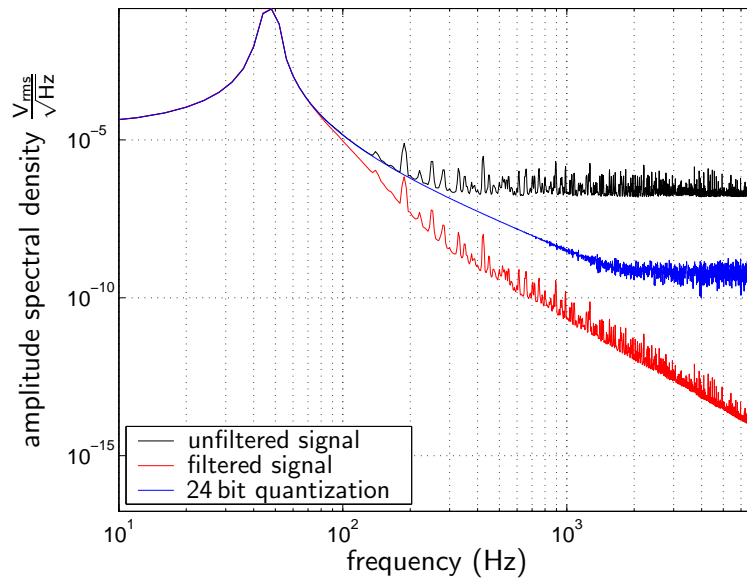
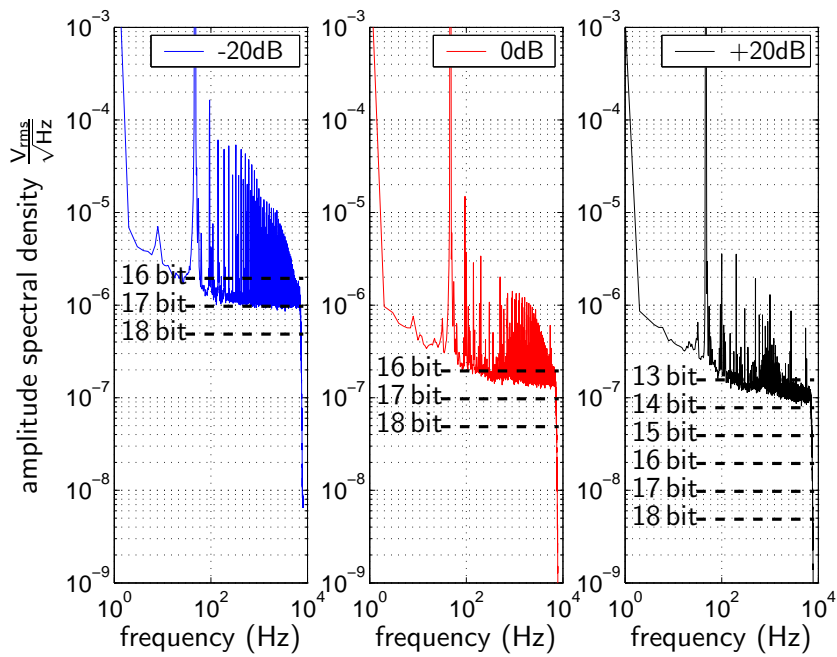


Figure 2.37.: Checking the signal used to measure the noise floor.

Figure 2.38.: Noise floor of *ICS110B* ADC using different pre-amplifier settings.

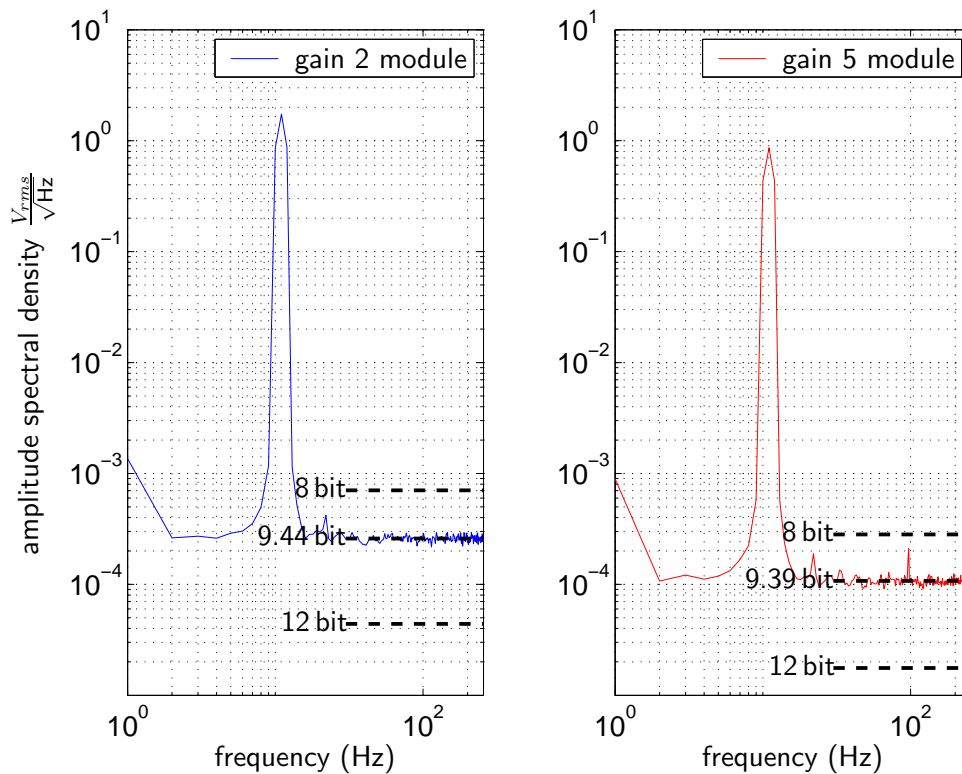


Figure 2.39.: Noise floor of VMIC ADC.

All measured values are above the limit of 19.9 bit given in the data sheet. Apparently there is excess noise coupled into the system. For the 0 dB setting ( $4 V_{pp}$  input range), the measured noise level corresponds to a noise floor generated by 16 bit quantization. Changing the preamplifier gain to -20 dB slightly improves the noise performance. It corresponds to quantization noise at 17 bit resolution. Setting the gain to +20 dB increases the noise level to less than 14 bit resolution. In summary the measurements showed that the programmable preamplifier should not be used to amplify an input signal since this will decrease the dynamic range of the digitized signal. When operated with a gain  $\leq 1$  the effective resolution of the digital signal is between 16 and 17 bit.

A similar measurement was performed for the VMIC ADC board that has a nominal sampling resolution of 12 bit. Because of the lower sampling rate of 512 Hz a sine wave with a frequency of only 11 Hz was used as input signal. The signal was connected to the patch bay that provides a selectable gain of either 2 or 5 for each of the channels. The noise level was measured for both possible gain settings. The data plotted in figure 2.39 show that the effective resolution is about 9.5 bit for any of the gain settings.



## Chapter 3.

# Data Analysis

### 3.1. Data runs

#### 3.1.1. Engineering run 7 (E7)

The first official data taking run of GEO 600 was coincident with the LIGO *engineering run 7* (E7) and took place from 2001-12-28 21:00:00 to 2002-01-14 21:00:00 (UTC). The duty cycle of the GEO 600 interferometer was about 75% counting only lock stretches longer than 10 minutes. In the final 24 hours 98% duty cycle was obtained. The longest lock stretch was 218 minutes. In this run data taking over long periods was successfully tested. The data acquired over this period could be used to test the GEO 600 data analysis tools like GEO++ [65].

#### 3.1.2. Science run 1 (S1)

The gravitational-wave detector GEO 600 recorded 17 days of data during the S1 data taking run from 2002-08-23 15:00:00 to 2002-09-09 15:00:00 (UTC) that was carried out in conjunction with GEO 600's LSC [68] partners from LIGO [5]. At that time, signal-recycling was not yet implemented in GEO 600 such that the interferometer was running in the power-recycling configuration only. The overall time of the run was reduced from 408 h to 401 h by maintenance periods that were scheduled once a day for a maximum time of one hour. From the remaining 401 h the interferometer was in the locked state for 396.03 h which corresponds to a duty cycle of 98.52%. Figure 3.1 shows the duty cycle plotted against the time of the run. In the lower graph the lock status of the interferometer is shown. In addition the maintenance periods are displayed.

A typical sensitivity curve of the GEO 600 instrument during the S1 run can be seen in figure 3.2. The power spectral density was calculated from 120 seconds of data taken from the last day of the run. A Hanning window was applied to the data. The narrow features at odd multiples of 244 Hz are injected calibration lines. The evolution of the strain channel during S1 can be seen in figure 3.3. Blue vertical lines indicate that the interferometer was out of lock. The plot was generated by taking a two-second long data segment from each hour of the run and generating a PSD from it. The data acquired during the S1 run by GEO 600 and LIGO were used to derive upper limits for the emission of gravitational wave by astronomical sources (see [1], [2], [3] and [4]).

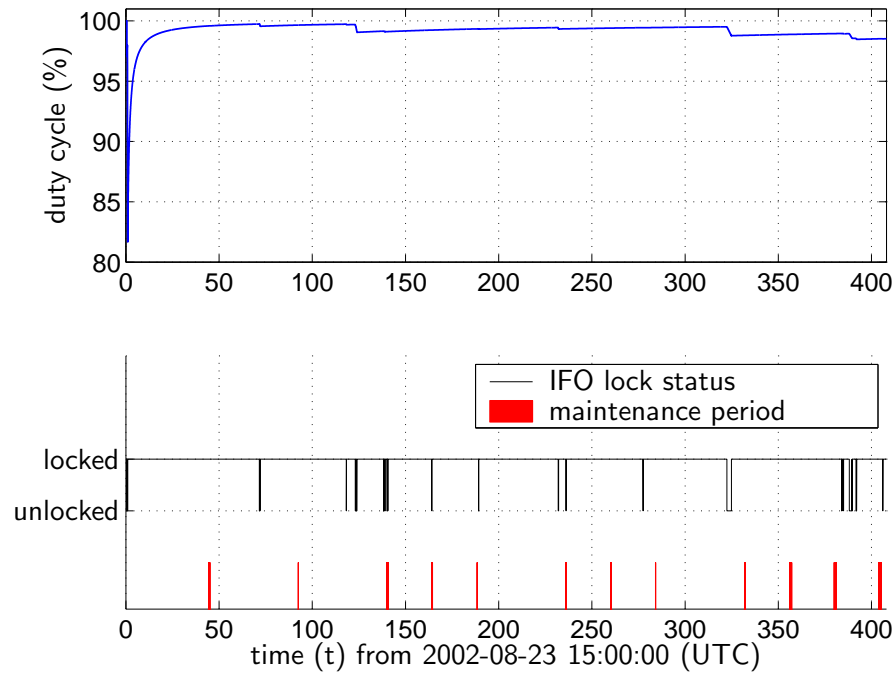


Figure 3.1.: Upper graph: Duty cycle of the GEO 600 detector during the S1 run.  
 Lower graph: lock status if the interferometer (black line). In addition maintenance periods are marked.

### 3.1.2.1. S1 timing accuracy

The tests of the DAQS timing accuracy described in section 2.3.1 were done after the S1 run was already completed. This test revealed two major problems. First of all the timestamping of the data is offset by  $2300\ \mu\text{s}$  after a software reboot of the DCU. In addition, timing fluctuations of a few microseconds were observed for a period of about ten minutes after power cycling the GPS card. All data recorded during the S1 run needed to be checked retrospectively for these problems. The ramp signal used for the tests described in section 2.3.1 was not available during the time of the S1 data run. To test the timing accuracy during that period we used a calibration signal [33]. The primary purpose of this signal was to provide information for converting the interferometer output signal into the  $h(t)$ -channel. The signal was suitable for the timing test because it was produced by an *HP33120A* generator that was frequency locked to the GPS/Rb timing unit described in the section 2.3.1 and the signal was recorded in the DAQS for the entire time of the S1 data run. This signal (see figure 3.4) was a square wave with a repetition rate of 244 Hz differentiated twice to give a set of spectral peaks. Figure 3.4 shows a close-up view of this signal. Also shown is a slope fitted to a particular part of the signal. This fit was performed once every 15 seconds for the whole of the S1 data. Any change in the timing offset could be detected by tracking the zero-crossing of the fitted line.

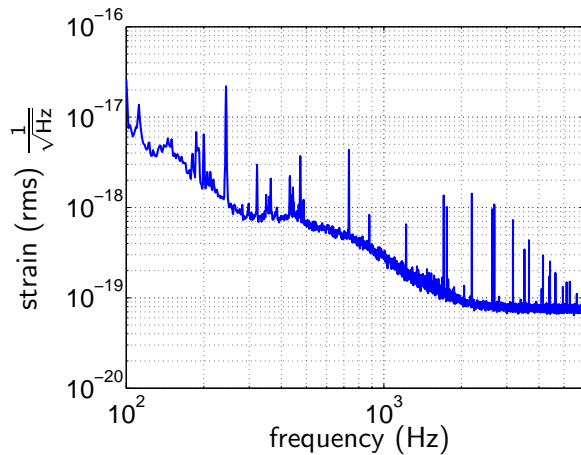


Figure 3.2.: Sensitivity Curve of GEO 600 during the S1 run.

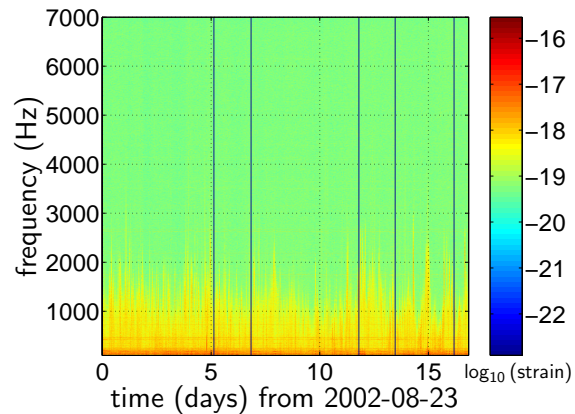


Figure 3.3.: Time-frequency plot of the  $h(t)$ -channel during the S1 run.

The upper graph of figure 3.5 shows the results of the analysis of all the S1 data. Two distinct variations in the measured zero crossings can be seen in this figure: two periods where the values differ significantly (by about  $2300\ \mu\text{s}$ ) and a general linear drift. The timing of the DAQS does not drift in time as we know from the tests presented in section 2.3.1. The linear drift of the zero crossing is caused by the signal generator producing the calibration signal. From the drift rate of the zero crossing it was calculated that the frequency of the signal is  $243.999\ 999\ 938\ \text{Hz}$  instead of the nominal value of  $244\ \text{Hz}$ .

Because the calibration signal is not related to absolute GPS time, we cannot derive any absolute timing information from it. The large offset of more than  $2000\ \mu\text{s}$  displayed in figure 3.5(a) showing the timing residuals for the entire S1 run is arbitrary—it just represents the point in the waveform that we chose to measure. This offset and the drift caused by the frequency offset of the signal generator was removed in figure 3.5(b) and subsequent plots.

From the previously described tests in section 2.3.1 we know that the timing offsets of the DAQ system are in the correct state after a hardware reboot. The two short periods where the measured zero crossing differs significantly represent times when the DAQ system was rebooted via the software interface. This type of rebooting was shown in section 2.3.1.3 to induce a state where the timing is offset by the gate delay of about  $2300\ \mu\text{s}$ . These times, namely 2002-08-23 15:00:00 to 2002-08-23 15:32:00 (UTC) and 2002-09-08 15:01:00 to 2002-09-08 15:06:00 (UTC) with an overall length of 37 minutes, are highlighted in figure 3.6.

Figure 3.8 shows the timing residuals of the system in the correct state in more detail. One can see steps in the measured timing offset of about  $10\ \mu\text{s}$  that occur roughly every 70 hours. The times when the steps occur coincide with the times when the data segment used for fitting the slope to the calibration signal has to be moved because the drift of the calibration signal has accumulated to the time of one sample. This can be seen in the lower graph of figure 3.8 where a plot of the boundaries of the data segment used for the fitting process is shown. Moving the boundaries of this segment by one sample changes the slope and thus

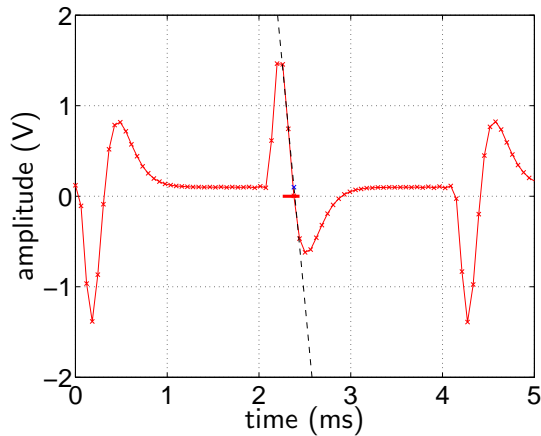


Figure 3.4.: A close-up view of the calibration signal injected throughout S1. Also shown is the line fit to the falling slope of the signal at a particular time.

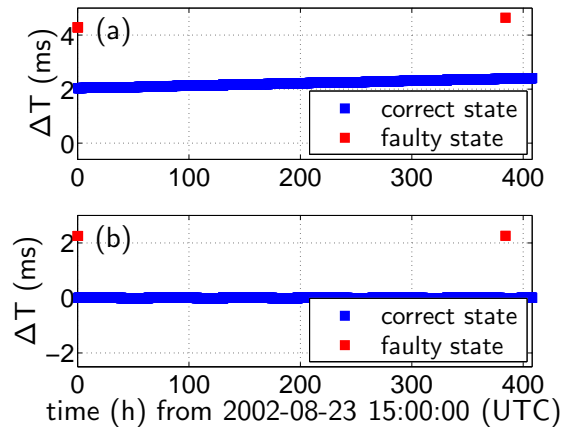


Figure 3.5.: (a): Time series showing the timing residuals for the whole S1 run. (b): timing residuals de-trended and offset removed. Values are around 0 ms in the correct state, values around 2.3 ms indicate the two occurrences of a faulty state of the system in the entire S1 run.

the zero-crossing of the fitted line, because the calibration signal used for the fitting process is only approximately linear. The slow drift of the measured offset between the steps is also due to the non-linearity of the data segments being used for fitting: the slope of the fitted line changes as the non-linear signal segment drifts with respect to the sampling times.

The upper graph of figure 3.8 shows also three small vertical glitches that occur at times when the DAQ system was hardware rebooted (i.e. power cycled). Figure 3.7 shows two of these segments in more detail. These glitches are caused by the servo of the GPS receiver as it was explained in section 2.3.1.4.

In summary, the analysis helped to discover 37 minutes of data that had an offset of about  $2300 \mu\text{s}$  in the timestamps and needed to be excluded from the data set going into gravitational wave search algorithms. Fluctuations in the time stamps of up to  $5 \mu\text{s}$  over a period of about 20 minutes were observed three times during the S1 run due to power cycling of the GPS receiver. The timestamps on the rest of the data proved to be accurate and so that the data could be used for analysis.

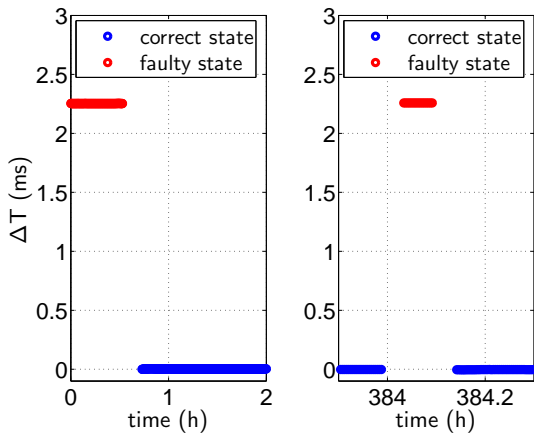


Figure 3.6.: Close-up view of the periods when the system was in the faulty state. Again, the data are de-trended and the offset removed. Note the different time scales in the two plots.

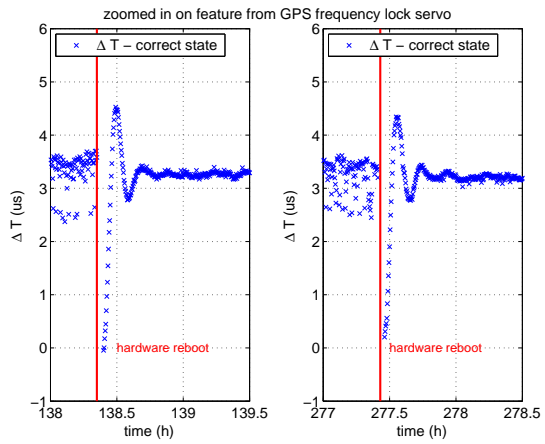


Figure 3.7.: The effect of the phase-locking servo of the GPS card on the timing accuracy of the DAQS. Prior to the hardware reboot, the DAQS was in a faulty state that manifests itself as additional noise on all channels. This can be seen in the larger scatter in the timing offset measurements.

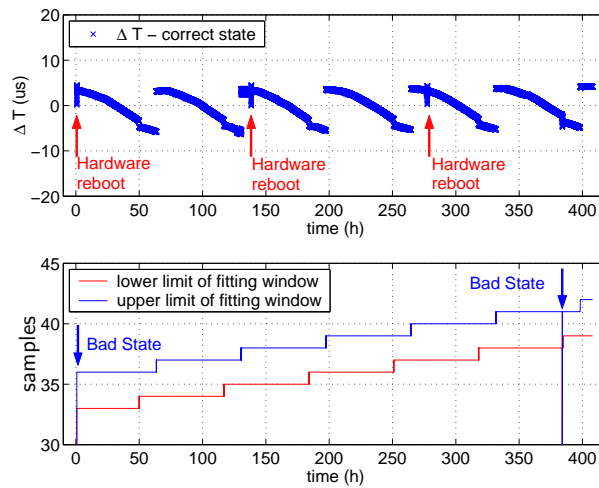


Figure 3.8.: Upper graph: timing residuals when DAQ system was in good state. Steps in the values are due to changes in the fitting parameters. The lower graph shows the times when the parameters of the fitting window (start and stop sample) were changed. The vertical lines in the lower graph are the times when the system was in the bad state.

## 3.2. Angular resolution of a worldwide gravitational-wave detector network

### 3.2.1. Introduction

Since a certain gravitational wave burst event can be observed by a global network of detectors, it is possible to determine the direction of arrival (DOA) of the signal by looking at the differences in the time of arrival (TOA) of the signal at each individual detector. By this method, it is possible to locate the position of the source in the sky with an accuracy that is dependant on the uncertainty in determining the time of arrival at each detector. Timing jitters in the individual DAQ systems contribute to this timing error. In this section, a numerical simulation is presented that shows the limit of the angular resolution of worldwide detector networks due to the timing jitter measured in the GEO 600 DAQS.

### 3.2.2. Theory

By measuring the time of arrival of a wave front arriving at a network of detectors the direction of arrival of the signal can be determined. The projection of the direction of arrival unit vector  $\mathbf{n}$  on the vector  $\mathbf{x}_j - \mathbf{x}_i$  connecting the detectors  $D_i$  and  $D_j$  is the distance that the wave front has to travel from  $D_i$  to  $D_j$ . This value has to be equal to the difference in the arrival times  $(t_i - t_j)$  multiplied with the propagation speed  $c$  of the wave:

$$(\mathbf{x}_i - \mathbf{x}_j) \cdot \mathbf{n} - (t_i - t_j) c = 0. \quad (3.1)$$

This is illustrated in figure 3.9 for two detectors in 2D-space. If more than two detectors are present in the network, equation 3.1 has to be true for all pairs  $(i, j)$  of detectors:

$$\sum_{i>j} ((\mathbf{x}_i - \mathbf{x}_j) \cdot \mathbf{n} - (t_i - t_j) c)^2 = 0 \quad (3.2)$$

For unambiguously determining the direction of arrival of a signal, data from at least four different detectors are required. In case the propagation speed of the signal is not known, the problem of finding the direction of arrival from the time of arrival of the signal at four detectors has one exact solution. If the propagation speed is fixed, the problem is over-constrained with time of arrival data from four detectors, while data from three detectors still leave two possible solutions for the direction of arrival. This is illustrated in figure 3.10. The gray surfaces are the planes of the incoming signal as they arrive at the detectors  $D_1$ ,  $D_2$  and  $D_3$ . The left figure shows one of the two solutions for the direction of arrival that matches the time of arrival  $t_1$ ,  $t_2$  and  $t_3$  measured at the individual detectors. By mirroring the direction of arrival vector on the plane defined by the location of the three detectors (white surface) another

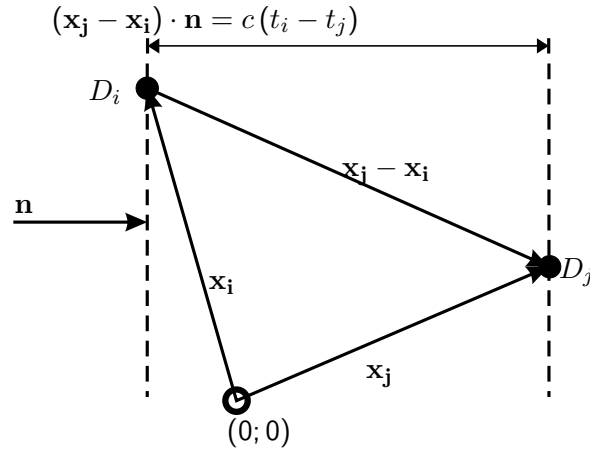


Figure 3.9.: Calculating the direction of arrival of a signal from the time of arrival data.

solution can be obtained that gives the same differences  $(t_1 - t_2)$ ,  $(t_1 - t_3)$  and  $(t_2 - t_3)$  of the arrival times. This solution is displayed on the right side of figure 3.10.

Adding an additional detector that lies outside the plane defined by the other three detectors will solve the problem of the ambiguity, but it will also overdetermine the problem. If the measurements of the time of arrival are not perfect but contain some measurement errors, then, in general, no solution for the direction of arrival can be found that matches exactly all measured time of arrival values. The best estimation of the direction of arrival gives time of arrival values  $t'_1, \dots, t'_k$  that have a minimal quadratic error  $\sum_{i>j}^k \left( (t_i - t_j) - (t'_i - t'_j) \right)^2$ . This solution can be found by applying a non-linear least-square-fit algorithm to the problem.

The uncertainty in this solution depends on the error in the time of arrival measurement. The error is also dependant on the orientation of the detectors compared to the incoming signal. This is illustrated in figure 3.11 and figure 3.12 for 2 detectors in a two-dimensional plane.

Figure 3.11 shows a signal impinging on two detectors ( $D_1, D_2$ ) oriented in a way that the connecting line  $\overline{D_1 D_2}$  between  $D_1$  and  $D_2$  is parallel to the incoming wave front (dashed line). In this case, the signal has the same travel distance to both detectors and arrives at the same time at  $D_1$  and  $D_2$ .

If the direction of the incoming wave is changed by an angle  $\phi$  (wave front indicated by dotted line) the signal has to travel a distance of  $d(\phi) = r \sin(\phi)$  further to detector  $D_1$  than to detector  $D_2$ . The difference in travel distance has changed from zero to  $\Delta d(\phi) = r \sin(\phi)$ . For small angles,  $\phi$ , this can be approximated by  $d(\phi) \approx r\phi$ . This corresponds to a time delay of

$$\Delta t \approx (r\phi) / c$$

where  $c$  is the propagation speed of the signal. It can be seen that the change in travel distance  $\Delta d$  and travel time  $\Delta t$  is linear in  $\phi$  for small angles.

The case where the plane of the incoming signal is perpendicular to  $\overline{D_1 D_2}$  is shown in figure 3.12. The signal has to travel a distance of  $r$  further to  $D_1$  than to  $D_2$ . If the direction

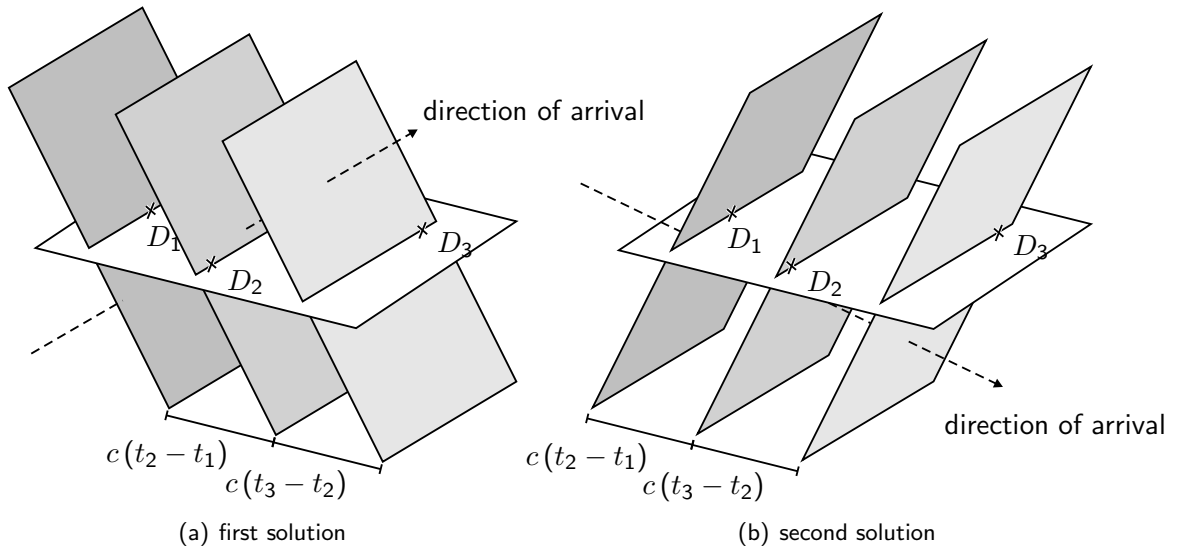


Figure 3.10.: Time of arrival data from 3 detectors leave two possible solutions for the direction of arrival of the signal. A direction of arrival matching the measured time of arrival can be mirrored on the plane spanned by the location of the detectors. The mirrored vector gives identical values for the relative time of arrival of the signal at  $D_1$ ,  $D_2$  and  $D_3$  and is therefore another valid solution.

of the incoming wave is changed by the angle  $\phi$  the difference in travel distance becomes  $d(\phi) = r \cos(\phi)$ . Compared to the case when the wavefront was perpendicular to  $\overline{D_1 D_2}$ , this is a change of  $\Delta d = r - d(\phi) = r - r \cos(\phi)$ . For small angles,  $\phi$ , the equation can be approximated by  $\Delta d \approx r - r(1 - \phi^2) = r\phi^2$ . The corresponding time delay is

$$\Delta t \approx (r\phi^2) / c$$

It can be seen that in this case  $\Delta d$  and  $\Delta t$  grow quadratically with  $\phi$ .

This means that the measurement of the direction of arrival from the time of arrival at  $D_1$  and  $D_2$  is more susceptible to errors in the relative arrival time  $\Delta t$  when the wave impinges perpendicular to  $\overline{D_1 D_2}$ . Because the direction  $\phi$  of the incoming wave changes the arrival time only in second order, the angle  $\phi$  can change by a larger amount without modifying the time of arrival significantly.

### 3.2.3. The algorithm

To determine the uncertainty in a direction of arrival estimation due to timing jitter from the GEO 600 DAQS, a Monte-Carlo simulation was implemented as a *Matlab* program. The software determines the resulting standard deviation  $\sigma_{\text{DOA}}$  of the direction of arrival estimation when the time of arrival information from the network of detectors has a timing error,  $\tau$ , that has a Gaussian distribution with a standard deviation of  $\sigma_\tau$ . The value of  $\sigma_{\text{DOA}}$  is



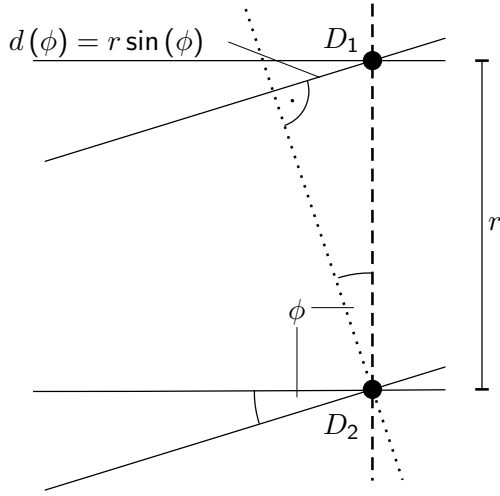


Figure 3.11.: Impinging Signal with the wave front parallel to  $\overline{D_1 D_2}$ . If the direction of arrival is changed by a small angle  $\phi$  the difference in travel time to  $D_1$  and  $D_2$  changes linearly with  $\phi$ .

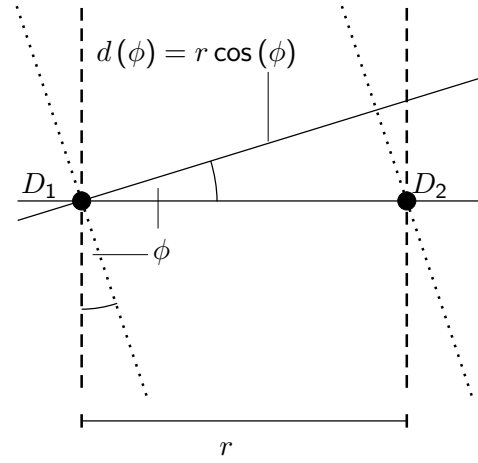


Figure 3.12.: Impinging Signal with the wave front perpendicular to  $\overline{D_1 D_2}$ . If the direction of arrival is changed by a small angle  $\phi$  the difference in travel time to  $D_1$  and  $D_2$  changes quadratically with  $\phi$ .

evaluated on a grid of  $v$  latitude values  $l_{\text{lat}}$  and  $w$  longitude values  $l_{\text{long}}$ . The calculated value  $\sigma_{\text{DOA}}(l_{\text{lat}}; l_{\text{long}}; \tau)$  gives the standard deviation of the direction of arrival estimation for a wave plane hitting the earth perpendicular at the point defined by  $(l_{\text{lat}}; l_{\text{long}})$ . To determine  $\sigma_{\text{DOA}}$ , the following steps are performed for each of the  $v \times w$  data points in the longitude/latitude grid.

- For each detector in the network the true time of arrival of the signal is calculated for a direction of arrival  $\mathbf{n}$  defined by  $(l_{\text{lat}}; l_{\text{long}})$ .
- Each time of arrival value is modified by adding a random timing jitter  $\tau$  that is taken from a Gaussian distribution with a standard deviation of  $\sigma_\tau$ .
- From the modified time of arrival values the best estimate for the direction of arrival is reconstructed by minimizing the quantity  $s^2 = \sum_{i>j} ((\mathbf{x}_i - \mathbf{x}_j) \cdot \mathbf{n} - (t_i - t_j)c)^2$ . This is done using the Nelder and Mead [43] algorithm for minimizing a multi-dimensional function.
- This procedure is repeated  $p$  times for the same  $(l_{\text{lat}}; l_{\text{long}})$  value so that the mean and the standard deviation can be calculated from the  $p$  different values.

### 3.2.4. Results

Given the timing jitter of 63 ns measured in the GEO 600 DAQS the resulting direction of arrival error can be seen in figure 3.13 and 3.14 for two different networks of detectors. The

geographical locations of the detector sites are listed in table 3.1.

detector	longitude	latitude
GEO 600	9.807° <i>E</i>	52.245° <i>N</i>
LLO	90.733° <i>W</i>	30.563° <i>N</i>
LHO	119.408° <i>W</i>	46.455° <i>N</i>
VIRGO	10.504° <i>E</i>	43.631° <i>N</i>
TAMA	139.539° <i>E</i>	35.674° <i>N</i>
ACIGA	115.900° <i>E</i>	31.350° <i>S</i>

Table 3.1.: Geographical location of the gravitational-wave detectors used in the Monte-Carlo simulation.

Plot 3.13 was generated using a network that included GEO 600, LLO (LIGO Livingstone Observatory), LHO (LIGO Hanford Observatory) and TAMA. In the top left corner the location of the detectors on the earth is indicated. It can be seen that  $\sigma_{\text{DOA}}$  has a strong dependence on the direction of the incoming signal. All four detectors of the network lie in a plane that is approximately parallel to the equatorial plane of the earth. As illustrated in figure 3.11 and 3.12 for the two-dimensional case the angular resolution of such a network is higher for a signal arriving perpendicular to the plane defined by the detectors. The data presented in figure 3.14 were generated with the VIRGO and ACIGA detectors added to the network. The error in the direction of arrival estimation depends much less on the direction of the incoming signal. This is because the network contains now the ACIGA detector that lies far outside the plane defined by the other detectors. In addition  $\sigma_{\text{DOA}}$  is getting smaller when the two detectors are added to the network.

For timing jitters in the ms range and below the error in the estimation of the direction of arrival scales linearly with  $\sigma_{\tau}$ . Figures 3.13 and 3.14 show data generated for a timing jitter of  $\sigma_{\tau} = 6.3$  ms which is 100 times larger than observed in the GEO 600 DAQS. The error in the direction of arrival estimation is increased by a factor of about 100 compared to the previous plots.

In summary the simulations have shown that for the two considered detector networks the timing jitter measured on the GEO 600 DAQS yields a  $\sigma_{\text{DOA}}$  value that is smaller than  $0.001^{\circ}$ .

3.2. Angular resolution of a worldwide gravitational-wave detector network

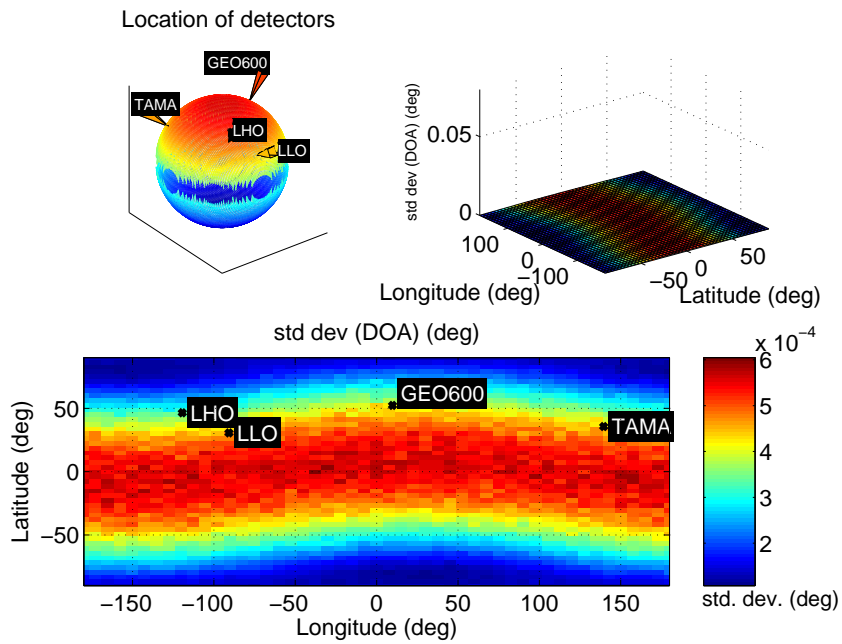


Figure 3.13.: Direction of arrival error estimation, 4 detectors, timing jitter:  $\sigma = 63$  ns

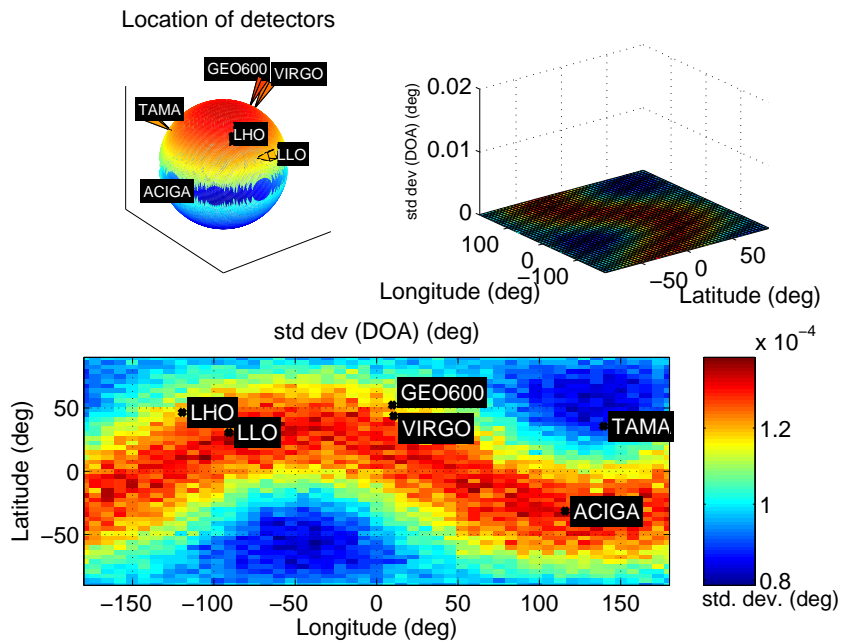


Figure 3.14.: Direction of arrival error estimation for 6 detectors, timing jitter:  $\sigma = 63$  ns

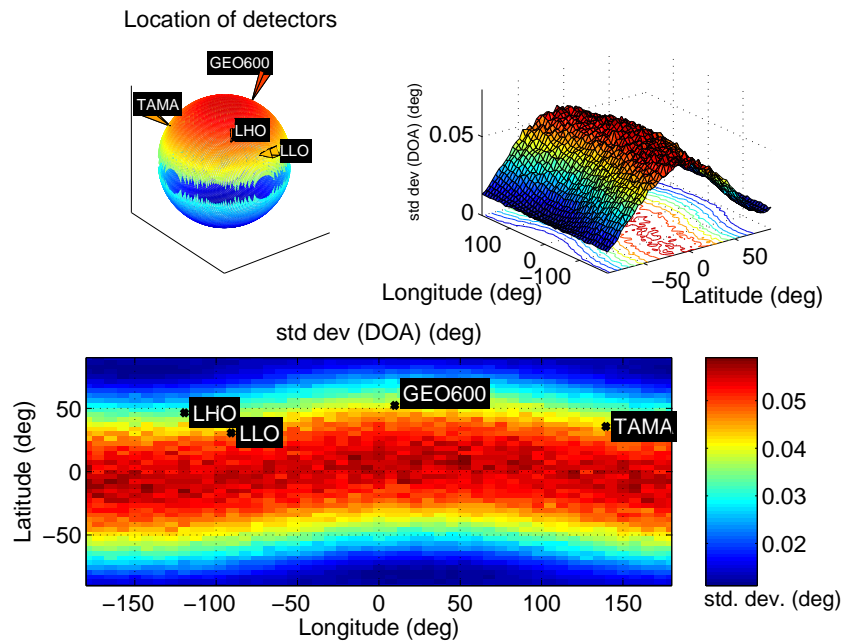


Figure 3.15.: Direction of arrival error estimation for 4 detectors, timing jitter:  $\sigma = 6.3 \mu\text{s}$

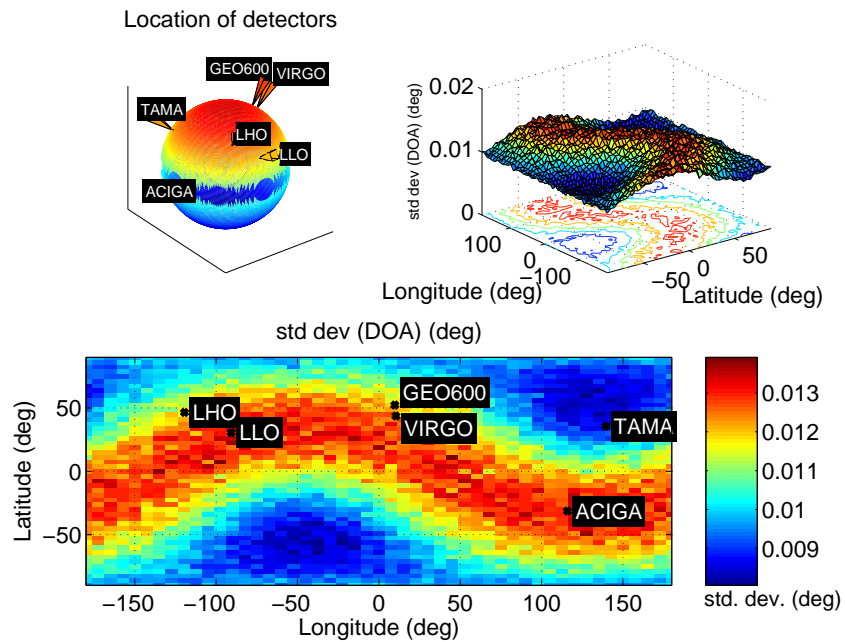


Figure 3.16.: Direction of arrival error estimation for 6 detectors, timing jitter:  $\sigma = 6.3 \mu\text{s}$

### 3.3. Vetoing burst events with PQMon

Data taken by GEO 600 during the science run S1 contain a large number of transients. In order to reduce the false alarm rate of burst gravitational wave search algorithms it is desirable to veto all those transients that are clearly not of gravitational wave origin. The “PQMon” scheme presented here vetoes transients by looking at the “in-phase” ( $P$ ) and “quadrature” ( $Q$ ) channels of the demodulated interferometer output signal. By taking advantage of the fact that the  $P$ -channel and the  $Q$ -channel have different sensitivities to gravitational wave burst events, this method can veto transients that have a power distribution different from the signature of a signal induced by a gravitational wave.

#### 3.3.1. Introduction

The search algorithms looking for gravitational wave burst events (e.g. *ExcessPower* [8] and *TFCLUSTERS* [53]) find a large number of candidate burst events because the  $h(t)$ -channel contains many transients that are most likely caused by environmental disturbances or instrumental noise. Therefore, it is desirable to develop veto strategies that will eliminate a large fraction of these spurious events.

While it is hoped that environmental monitors will ultimately play a large part in the vetoing of spurious events, it is also appropriate to develop vetoes that are based on differences of the interferometer responses to gravitational waves and to environmental triggers.

#### 3.3.2. Vetoing burst events using PQMon

##### 3.3.2.1. Concept of the PQMon algorithm

Figure 3.17 shows a simplified schematic of the GEO 600 optical setup during the S1 run. The laser light that is injected into the interferometer is frequency modulated by an electro-optical modulator (EOM) driven by a 14.9 MHz sine wave generator. By demodulating the signal coming from the output photo detector located at the output port of the interferometer, the in-phase ( $P$ ) and quadrature ( $Q$ ) channels are obtained.

A phase shifter is used to maximize the sensitivity to differential arm length changes of the  $P$ -channel. At the same time, it minimizes the sensitivity of the  $Q$ -channel. This adjustment of the demodulation phase is never perfect (e.g. due to slow drifts that can be seen in figure 3.22) so that the sensitivity of the  $Q$ -channel is not zero but much lower than the sensitivity of the  $P$ -channel. The information contained in these channels allows identification of transients that are not caused by a differential arm length change in the interferometer and therefore cannot be of gravitational wave origin:

The relative sensitivity of the  $P$ - and the  $Q$ -channel to differential arm length changes can be obtained by monitoring the power  $P_c$  and  $Q_c$  of the calibration lines in the respective channel. One can then look at a candidate burst event and determine the power  $P_b$  and  $Q_b$  in the

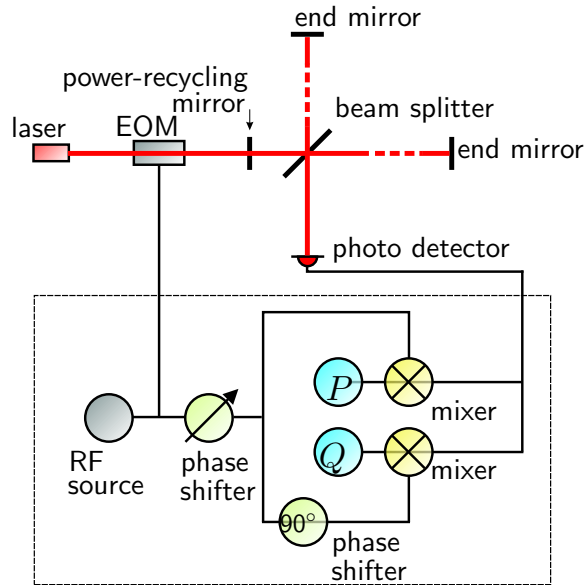


Figure 3.17.: In-phase and quadrature channels of GEO 600.

two channels during the time of the event. The ratio  $P_b/Q_b$  should be close to  $P_c/Q_c$  for an event induced by a gravitational wave.

In summary the *PQMon* algorithm performs the following steps:

- detect candidate burst event in the  $h(t)$ -channel
- check power distribution of candidate event in  $P$ - and  $Q$ -channel ( $P_b/Q_b$ )
- determine relative sensitivity to differential arm length changes of  $P$ -channel and  $Q$ -channel ( $P_c/Q_c$ ) by measuring the calibration signal
- compare  $P_b/Q_b$  and  $P_c/Q_c$  and decide whether to veto the event or not

### 3.3.2.2. Transient detection

For detection of transients in the data, a very simple algorithm is employed. Three adjacent time domain windows are moved along the data (see figure 3.18).

In order to detect a transient in window  $B$  the average power per sample (called  $\bar{B}$ ) is computed for this window that has a length of 10 samples ( $\cong 610 \mu\text{s}$ ). To get an estimation of the noise that is present in the data the average power per sample is also computed for the combination of windows  $A$  and  $C$  (called  $\bar{N}$ ). Each of these windows has a length of 45 samples ( $\cong 2.74 \text{ ms}$ ). The value  $\bar{B}/\bar{N}$  represents the signal to noise ratio (SNR) in power of the event in window  $B$ . When this SNR crosses a given threshold, the time at the center of window  $B$  is considered as the start of a transient. This value is recorded together with the maximum SNR and the time when the SNR drops below the threshold again which marks the end of the event.

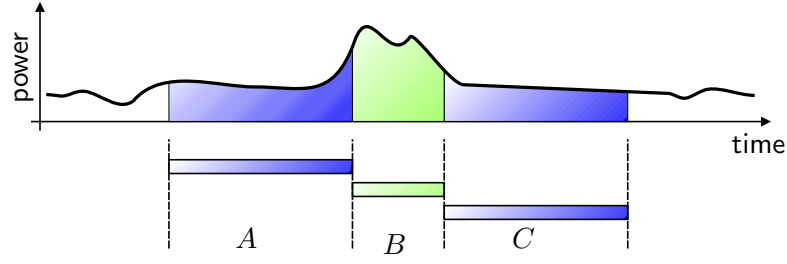


Figure 3.18.: Time domain windows used for the transient detection algorithm

### 3.3.2.3. Measuring the power ratio $P_b/Q_b$ of a candidate burst event

To obtain the power distribution in the  $P$ - and  $Q$ -channel for the transient, the same time domain windows (see figure 3.18) as for the transient detection were used. The windows are positioned so that the time of the peak of the candidate event is in the center of window  $B$ . As for the transient detection, the noise floor is estimated by averaging the power in windows  $A$  and  $C$ . This value is assumed to be the mean power of the underlying noise,  $\langle n^2 \rangle$ , in window  $B$ . In addition it is assumed that the noise has a Gaussian distribution, so that  $\text{var}(n^2) = 2\langle n^2 \rangle^2$ . The overall signal power  $S_{\text{winB}}^2$  in window  $B$  is obtained by measuring the overall power in each time domain bin,  $V_i^2$ , corrected for the noise contribution,  $\langle n^2 \rangle$  which gives the estimated signal power per time domain bin,  $\hat{S}_i^2$ :

$$\hat{S}_i^2 = V_i^2 - \langle n^2 \rangle. \quad (3.3)$$

The variance of this estimation is

$$\begin{aligned} \text{var}(\hat{S}_i^2) &= \text{var}(V^2 - \langle n^2 \rangle) \\ &= \text{var}(S_i^2 + 2S_i n + n^2 - \langle n^2 \rangle) \\ &= \text{var}(2S_i n + n^2) \\ &= \langle (2S_i n + n^2)^2 \rangle - \langle 2S_i n + n^2 \rangle^2 \\ &= \langle 4S_i^2 n^2 + 4S_i n^3 + n^4 - (2S_i \langle n \rangle)^2 + 4S_i \langle n \rangle \langle n^2 \rangle + \langle n^4 \rangle \rangle \\ &= 4S_i^2 \langle n^2 \rangle + \langle n^4 \rangle - \langle n^2 \rangle^2 \\ &= 4S_i^2 \langle n^2 \rangle + \text{var}(n^2) \\ &= 4S_i^2 \langle n^2 \rangle + 2\langle n^2 \rangle^2 \end{aligned} \quad (3.4)$$

The estimate for the overall signal power in window  $B$  is the sum of the signal power in all

of its time domain bins:

$$\hat{S}_{\text{winB}}^2 = \sum_i \hat{S}_i^2. \quad (3.5)$$

Under the assumption that the measurements of  $\hat{S}_i^2$  are uncorrelated the value of  $\hat{S}_{\text{winB}}^2$  has a variance of

$$\text{var}(\hat{S}_{\text{winB}}^2) = \sum_i \text{var}(\hat{S}_i^2). \quad (3.6)$$

Measuring the power and its variance in the central window in the channels  $P$  and  $Q$  gives the values for  $P_b$  and  $Q_b$  so that the ratio  $P_b/Q_b$  and the variance of  $P_b/Q_b$  can be determined.

#### 3.3.2.4. Measuring the calibration line ratio $P_c/Q_c$

To calibrate the output signal of the GEO 600 interferometer, a set of calibration lines is continuously injected into the instrument. This is done by moving the end mirrors in a controlled way at three different frequencies [33]. By comparing the response of the  $P$ - and the  $Q$ -channel to the calibration signal, the relative sensitivity of these channels can be determined.

By locking the calibration frequencies to the sample clock of the data acquisition system, we ensure that the calibration lines are not drifting with respect to the sampling frequency. Therefore all power of a line will show up in a single frequency bin,  $b_{\text{cal}}$ , in a power spectral density (PSD), provided the frequency resolution is chosen such that the calibration line is in the center of a frequency bin.

The overall power,  $V^2$ , measured in the calibration line frequency bin  $b_{\text{cal}}$  will be the sum of the power,  $S_c^2$ , originating from the calibration line and the power,  $n^2$ , due to noise.

To determine the contribution of the noise in  $b_{\text{cal}}$ , it is assumed that the noise can be modeled as Gaussian white noise in the time domain.

This means that the variance of the noise power,  $n^2$ , in a frequency bin can be determined from the average power,  $\eta^2$ , in that bin by

$$\text{var}(n^2) = \langle \eta^2 \rangle^2, \quad (3.7)$$

Measurement and averaging of the noise power per bin,  $\eta^2$ , is illustrated in figure 3.19. By measuring frequency bins around  $b_{\text{cal}}$  (bins in region  $I$  and  $II$ ) that do not contain power



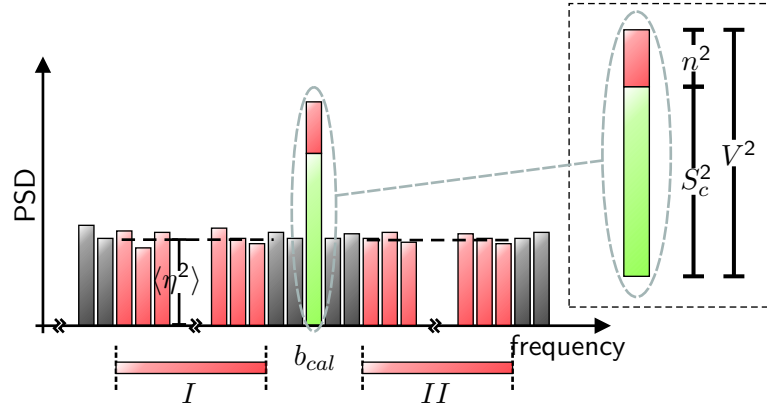


Figure 3.19.: Measuring the noise floor and the calibration line signal: the frequency bin  $b_{cal}$  contains the calibration line; windows  $I$  and  $II$  are used to determine the noise floor.

from the calibration signal, the average value,  $\langle \eta^2 \rangle$ , of the noise power in bin  $b_{cal}$  can be determined.

From the measurement of the overall power,  $V^2$ , in the calibration frequency bin one can get an estimation of the calibration signal power,  $\hat{S}_c^2$ , by subtracting the average noise power  $\langle \eta^2 \rangle$ :

$$\hat{S}_c^2 = V^2 - \langle \eta^2 \rangle. \quad (3.8)$$

Using equation 3.7 it can be shown that the variance of  $\hat{S}_c^2$  is given by:

$$\begin{aligned} \text{var}(\hat{S}_c^2) &= \text{var}(V^2 - \langle \eta^2 \rangle) \\ &= \text{var}(S_c^2 + S_c n + S_c n^* + n n^* - \langle \eta^2 \rangle) \\ &= \text{var}(S_c n + S_c n^* + n n^*) \\ &= \text{var}(2S_c \Re(n) + n n^*) \\ &= \langle (2S_c \Re(n) + n n^*) (2S_c \Re(n) + n n^*)^* \rangle \\ &\quad - \langle 2S_c \Re(n) + n n^* \rangle \langle (2S_c \Re(n) + n n^*)^* \rangle \\ &= \langle 4S_c^2 \Re^2(n) + 4S_c \Re(n) n n^* + (n n^*)^2 \rangle \\ &\quad - (2S_c \langle \Re(n) \rangle)^2 + 4S_c \langle \Re(n) \rangle \langle n n^* \rangle + \langle n n^* \rangle^2 \\ &= 4S_c^2 \langle \Re^2(n) \rangle + \langle (n n^*)^2 \rangle - \langle n n^* \rangle^2 \\ &= 2S_c^2 \langle n^2 \rangle + \text{var}(n^2) \\ &= 2S_c^2 \langle \eta^2 \rangle + \langle \eta^2 \rangle^2 \end{aligned} \quad (3.9)$$

By averaging the power spectral density  $N$  times, the variance is decreased by the factor  $1/N$ :

$$\text{var}(\hat{S}_c^2) = (2\hat{S}_c^2\langle\eta^2\rangle + \langle\eta^2\rangle^2) / N. \quad (3.10)$$

The ratio  $R_{cal_i}$  for each calibration line is calculated by

$$R_{cal_i} = P_{c_i} / Q_{c_i} \quad (3.11)$$

where  $P_{c_i}$  and  $Q_{c_i}$  are the measured powers of the  $i^{th}$  calibration line frequency in the  $P$ - and  $Q$ -channel respectively. The variance of the the value  $R_{cal_i}$  is called  $\sigma_{R_{cal_i}}$ .

For the optical configuration of GEO 600 used during the S1 run, the relative sensitivity to differential arm length change of the  $P$ - and the  $Q$ -channel is frequency independent. Therefore, the values  $R_{cal_i}$  for the three calibration lines are equivalent and the three individual measurements can easily be combined to an overall value with a smaller variance than that of each individual measurement. The combined value of  $R_{cal} = P_c / Q_c$  can be calculated by a weighted sum of the individual measurements,

$$R_{cal} = \frac{\sum_i R_{cal_i} \sigma_{R_{cal_i}}^{-2}}{\sum_i \sigma_{R_{cal_i}}^{-2}}. \quad (3.12)$$

The resulting variance of this value is

$$\sigma_{R_{cal}}^2 = \frac{1}{\sum_i \sigma_{R_{cal_i}}^{-2}}. \quad (3.13)$$

### 3.3.2.5. Verifying the statistics

The procedures for getting the power and variance of a transient (described in section 3.3.2.3) and the calibration lines (described in section 3.3.2.4) were verified by implementing the algorithms in Matlab and running it on data which give known results.

Figure 3.20 shows the results for the transient measurement: 5000 data segments were generated containing a transient with random noise added on top of it. One representation of such a segment is shown in 3.20(a). For each segment the estimate of the power,  $\hat{S}_{winB}^2$ , and its variance,  $\text{var}(\hat{S}_{winB}^2)$ , were computed with the method described in section 3.3.2.3. In figure 3.20(b) the estimated values of  $\hat{S}_{winB}^2$  are plotted (crosses). It can be seen that the know value of the transient power (solid line) is identical within the statistical fluctuations to the mean estimated power of  $\hat{S}_{winB}^2$  (dashed line). A similar plot for the variance is shown

in figure 3.20(c). The variance of the 5000 individual measurements of  $\hat{S}_{\text{winB}}^2$  (solid line) is identical within the statistical fluctuations to the mean estimated variance using the method described above.

Figure 3.21 shows the results for the calibration line measurement: Again 5000 data segments were generated containing a calibration line at 244 Hz with random noise added on top of it. One representation of such a segment is shown in the top plot. For each segment the estimate of the power  $\hat{S}_c^2$  and its variance  $\text{var}(\hat{S}_c^2)$  were computed with the method described in section 3.3.2.4. In the middle graph the estimated values of  $\hat{S}_c^2$  are plotted (crosses). It can be seen that the know value of the calibration line power (solid line) is identical within the statistical fluctuations to the mean estimated power of  $\hat{S}_c^2$  (dashed line). The lower graph shows that the variance of the 5000 individual measurements of  $\hat{S}_c^2$  (solid line) is identical within the statistical fluctuations to the mean estimated variance using the method described above.

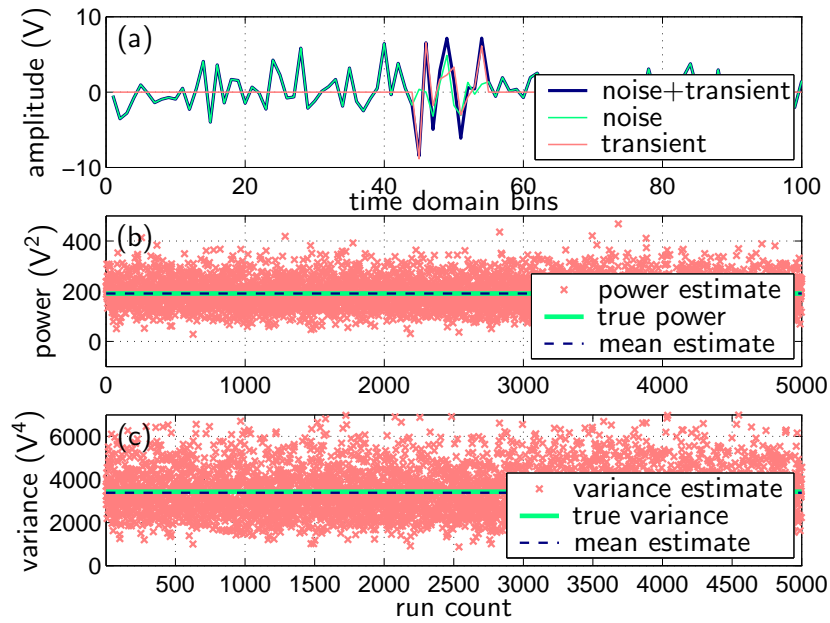


Figure 3.20.: Verifying the method for estimating the power of a transient and determining the variance of the estimate. Using synthesized data the known values (solid lines) for power and variance can be compared to the values given by the estimation process (dashed lines).

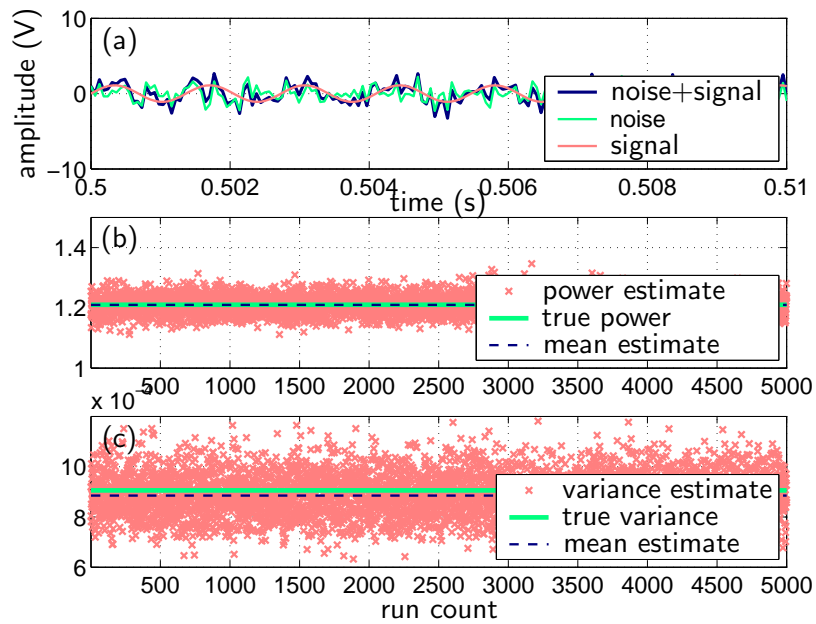


Figure 3.21.: Verifying the method for estimating the power of the calibration lines and determining the variance of the estimate. Using synthesized data the known values (solid lines) for power and variance can be compared to the values given by the estimation process (dashed lines).

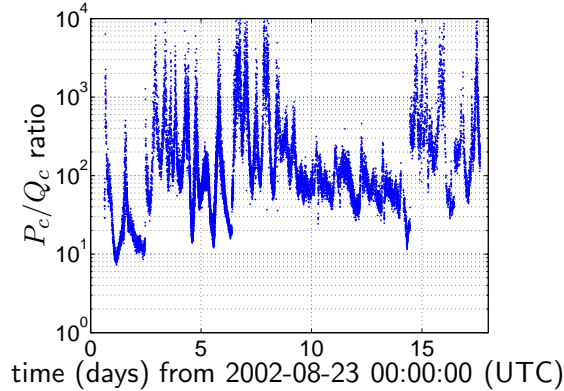


Figure 3.22.: Time evolution of the relative sensitivity  $P_c/Q_c$  during the S1 run.

### 3.3.3. Results

The following graphs show results that were obtained from GEO 600 data recorded during the S1 run that took place from 2002-08-23 15:00:00 to 2002-09-09 15:00:00 (UTC). For more than 98% of the time, the detector was producing valid data that could be used for analysis by *PQMon*.

The algorithm was implemented as a data analysis monitor written in *GEO++* [65] which is a C++ class library designed to process interferometer data. The monitor was run on data from the  $P$ - and the  $Q$ -channel. Before the algorithm was applied, the data were pre-whitened to equalize the amount of power in different frequency bands. For the transient detection algorithm, the whitened  $P$ -channel data are more suitable than the  $h(t)$ -channel data. The  $h(t)$ -channel has almost all of its power in the low frequency band so that events at high frequencies do not contribute enough signal power to trigger a detection. In general, using the  $P$ -channel for transient detection is equivalent to using the  $h(t)$ -channel which can be derived from the  $P$ -channel by linear filtering and therefore contains the same transients.

For the measurement of  $P_c/Q_c$  and  $P_b/Q_b$  whitened data were used as well. The whitening filters for the  $P$ - and the  $Q$ -channels were identical so that the results of both the  $P_c/Q_c$  and the  $P_b/Q_b$  measurement are not affected by the whitening process.

The transient detection algorithm was set up with a window length of 45 samples ( $\cong 2.74ms$ ) each for segments  $A$  and  $B$  and a length of 10 samples ( $\cong 610\mu s$ ) for window  $C$  (see figure 3.18). Measuring the  $P_b/Q_b$  value was done using the same window sizes as for the transient detection. The  $P_c/Q_c$  measurement was carried out with windows  $I$  and  $II$  (shown in figure 3.19) set to 20 bins starting 10 bins away from the calibration line frequency. For the vetoing decision, error bars of  $\pm 2\sigma$  were taken around both the  $P_c/Q_c$  and the  $P_b/Q_b$  measurement. This means that a candidate burst event was considered not to be of gravitational wave origin in the case that the intervals  $[P_c/Q_c - 2\sigma_c; P_c/Q_c + 2\sigma_c]$  and  $[P_b/Q_b - 2\sigma_b; P_b/Q_b + 2\sigma_b]$  did not overlap. The transient detection algorithm found a total number of 24801 events with a SNR greater than 3 during the S1 run. For 10105 of those events the values of  $P_c/Q_c$  and  $P_b/Q_b$  were so far apart that the event could be vetoed.

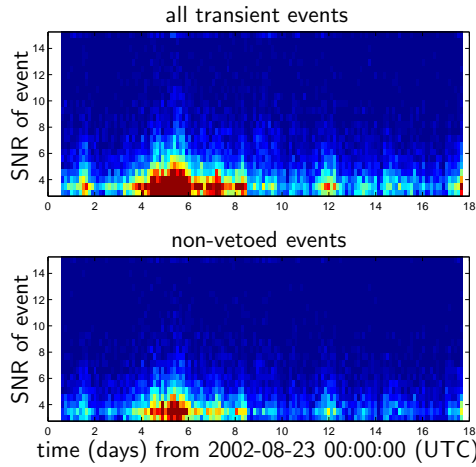


Figure 3.23.: Distribution of transients during the S1 run.

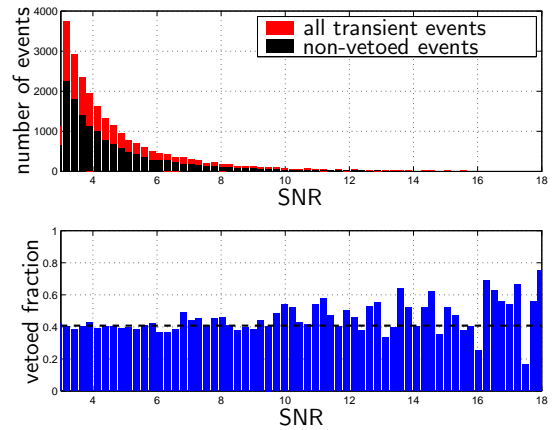


Figure 3.24.: Histogram of candidate burst events before and after the veto process.

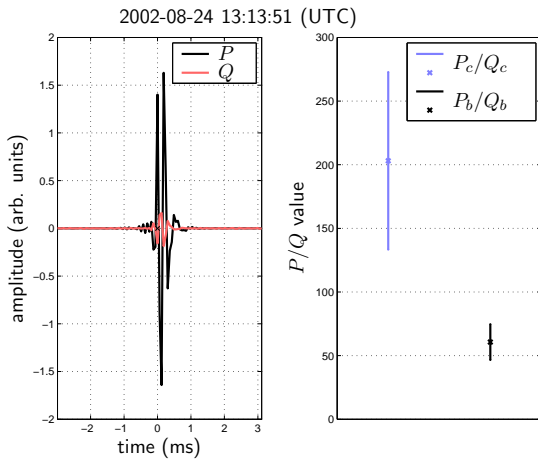


Figure 3.25.: Example of a vetoed event.

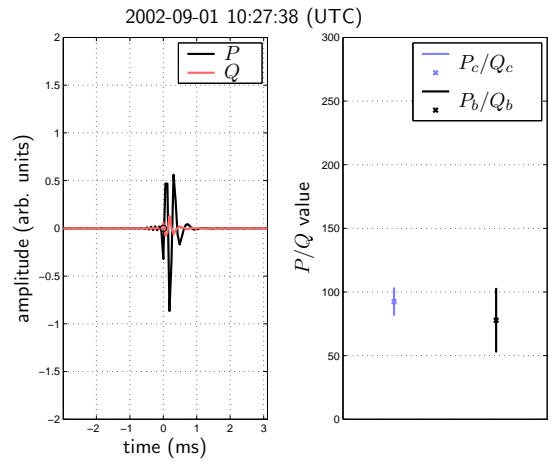


Figure 3.26.: Example of a non-vetoed event.

The evolution of the  $P_c/Q_c$  value over time can be seen in figure 3.22. The ratio is much greater than 1 most of the time. Transient events caused by environmental disturbances are expected to act similarly on both the  $P$ - and  $Q$ -channels (e.g. electronic pickup). Therefore, these events should be vetoed efficiently during all the periods where  $P_c/Q_c$  is significantly different from 1.

The upper graph in figure 3.23 shows the distribution of all detected events broken down into time and SNR bins. The lower graph shows the same plot for the remaining events after the  $PQMon$  veto was applied. In figure 3.24, a histogram of the SNR of the detected transients before and after the vetoing process is displayed. In the lower plot of the figure the vetoed fraction of the events is shown. It can be seen that the efficiency of the vetoing algorithm does not show any particular dependence on the SNR of the transient. The fraction of events vetoed is about 40.7% using the error bars stated above.

Figures 3.25 and 3.26 show two examples of transients that occurred during the S1 run. The left side of figure 3.25 shows the time series of an event that could be vetoed. On the right side the measured values of  $P_c/Q_c$  and  $P_b/Q_b$  including the respective error bars of size  $\pm 2\sigma_c$  and  $\pm 2\sigma_b$  are displayed: The value of  $P_b/Q_b$  of a gravitational wave induced event predicted by the calibration line measurement is above 200, while the transient showed only a  $P_b/Q_b$  value of only about 60. Looking at the error bars, one can see that this is sufficiently far away from the expected value (error bars do not overlap) for the event to be vetoed.

Figure 3.26 shows an event that could not be vetoed. The measured value for  $P_b/Q_b$  of about 78 is close enough to the expected value of about 92 for an event induced by a gravitational wave that the error bars of the two measurements overlap.

#### 3.3.4. Summary

It could be shown that by applying the *PQMon* algorithm it was possible to reduce the number of candidate burst events by roughly 40%. The vetoed events showed a power distribution in the  $P$ - and  $Q$ -channel that was significantly different from the values expected for a differential arm length change in the interferometer.





## **Appendix A.**

### **The optical layout of GEO 600**

# GEO 600 optical layout

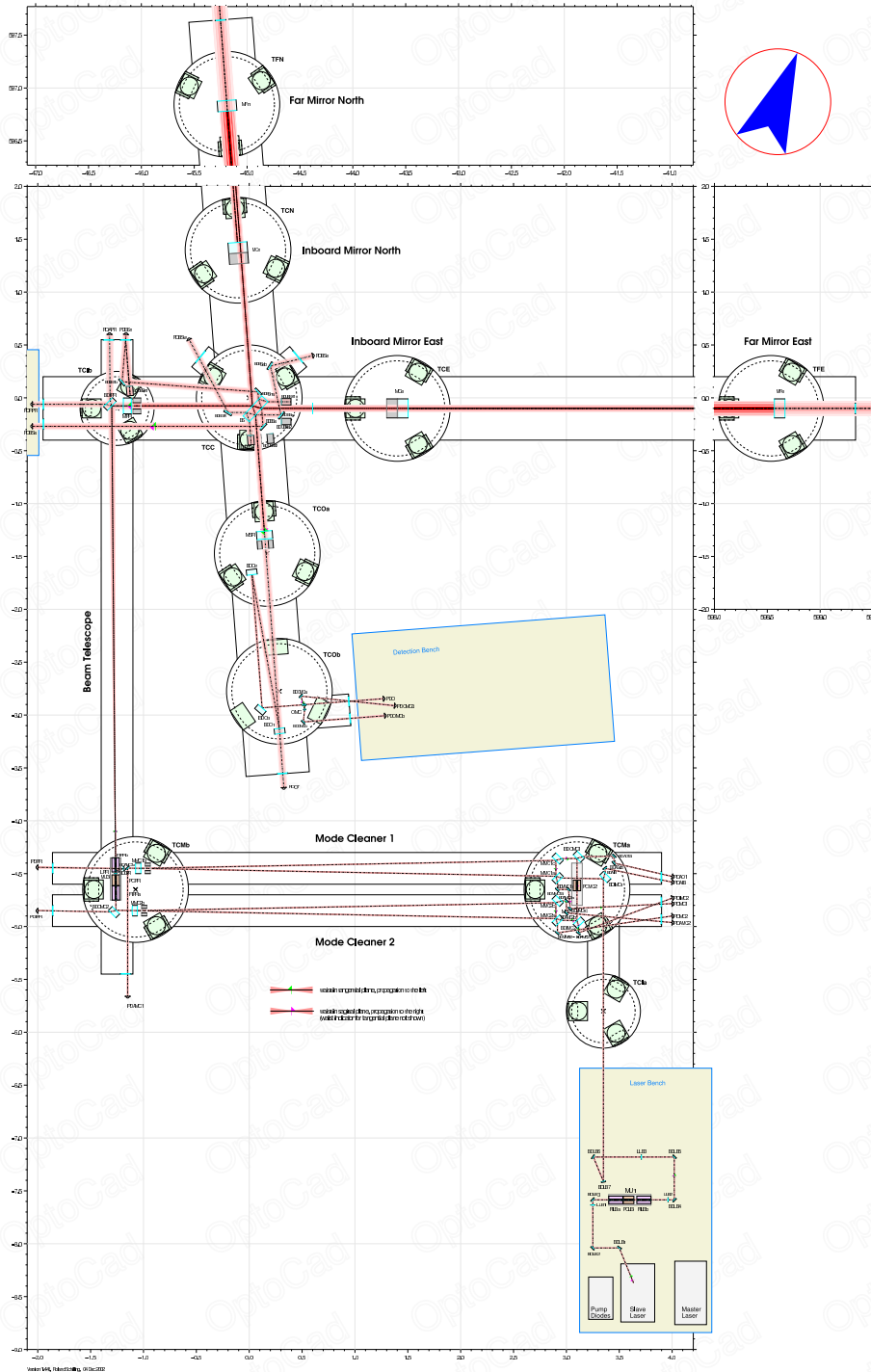


Figure A.1.: Detailed GEO 600 optical layout, created by Roland Schilling.

## Appendix B.

### Quantization noise

Converting an analog signal to a digital representation inevitably adds noise to the signal. This noise is caused by the amplitude quantization that is done in the AD conversion.

The amount of noise added depends on the dynamic range  $U_{pp}$ , the resolution of the analog to digital converter (ADC) and the sampling frequency. The dynamic range is the difference between the maximum and minimum voltage that can be converted to the ADC without causing overflow or underflow. The resolution of the ADC specifies the number of discrete values that the output of the ADC can have. An ADC with a resolution of  $n$  bits can produce  $2^n$  different output values. The voltage difference corresponding to one quantization step is given by

$$U_{\text{lsb}} = \frac{U_{pp}}{2^n}. \quad (\text{B.1})$$

The value  $U_{\text{lsb}}$  corresponds to one step of the least significant bit (lsb) of the binary number generated by the ADC.

In the AD conversion process the input values are rounded to the nearest quantization step. This is shown in figure B.1. Since the quantization steps are spaced at  $U_{\text{lsb}}$  the rounding process changes the amplitude by a value  $U_r$  between  $-U_{\text{lsb}}/2$  and  $U_{\text{lsb}}/2$ . If the quantization errors are stochastically distributed (this is true for most real signals, but not, e.g., for a pure sine-wave that is harmonically related to  $f_s$ ), then the rms error is given by

$$\begin{aligned} U_{q\text{rms}}^2 &= \frac{1}{U_{\text{lsb}}} \int_{-U_{\text{lsb}}/2}^{U_{\text{lsb}}/2} U_r^2 dU_r \\ &= \frac{1}{U_{\text{lsb}}} \frac{1}{3} \frac{U_{\text{lsb}}^3}{4} \\ &= \frac{1}{12} U_{\text{lsb}}^2. \end{aligned} \quad (\text{B.2})$$

The noise power is distributed over a bandwidth of  $f_{\text{Nyquist}} = f_s/2$ . This yields a power

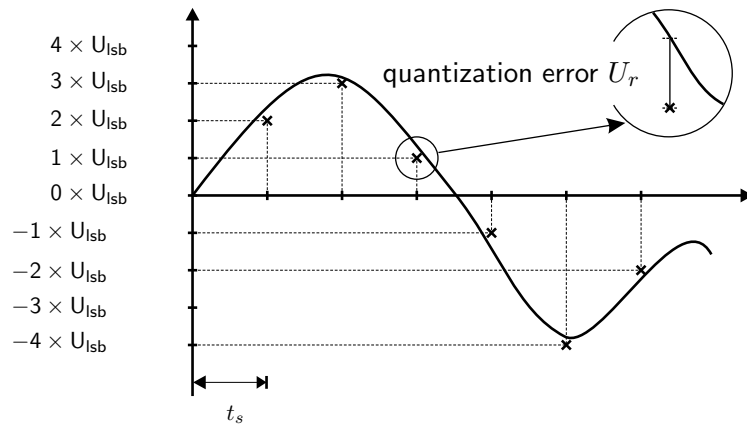


Figure B.1.: Amplitude rounding in quantization process.

spectral density of

$$P_{q_{rms}} = \frac{1}{12} U_{lsb}^2 \frac{1}{f_s/2} = \frac{U_{lsb}^2}{6f_s} \quad (\text{B.3})$$

and an amplitude spectral density of

$$A_{q_{rms}} = \frac{U_{lsb}}{\sqrt{6f_s}} \quad (\text{B.4})$$

# Appendix C.

## Digital filtering

Digital filtering transforms an equidistant input time series  $x_i$  into an output series  $y_i$  so that

$$H(f) = \frac{Y(f)}{X(f)}. \quad (\text{C.1})$$

$H(f)$  is the transfer function of the filter and  $X(f)$ ,  $Y(f)$  are the Discrete Fourier Transforms (DFTs) of the time series  $x(t_i)$ ,  $y(t_i)$ .

Two different approaches exist for applying a filter to data in a digital format: filtering can be done either in the frequency domain or in the time domain.

### C.1. Frequency domain filtering

Solving equation C.1 for  $Y$  shows that the DFT of the output time series can be obtained by multiplying the DFT of the input time series,  $X(f)$ , by the transfer function  $H(f)$  of the filter:

$$Y(f) = X(f) \times H(f) \quad (\text{C.2})$$

The output time series  $y$  can be obtained by applying an *inverse Discrete Fourier Transform* (IDFT) algorithm to  $Y$ . In summary the output  $y(t)$  can be obtained from the input  $x(t)$  by

$$y = \text{IDFT}(\text{DFT}(x) \times H). \quad (\text{C.3})$$

Filtering in the frequency domain is a straight-forward approach. The algorithm requires only the input data and the filter transfer function. The transfer function  $H$  of the filter can have an arbitrary frequency dependence. In case a Fast Fourier Transform (FFT) (e.g. [63]) algorithm is used for calculating the DFT the computational effort is  $O(n \log(n))$ . This

means that the effort grows  $\propto n \log(n)$  with  $n$  being the number of data points fed into the algorithm. All input data must be available when the filtering is performed. If the data are being processed in segments, artifacts ("jumps") will occur at the segment boundaries. This fact makes the DFT method unsuitable for realtime processing

## C.2. Time domain filtering

Filtering in the time domain directly processes the input time series and yields the output time series. Each sample  $y_j$  of the output time series  $y$  is obtained by multiplying the current and the previous  $M$  input samples  $x_{j-M}$  to  $x_j$  with a set of coefficients  $c_0$  to  $c_M$ . The previous  $N$  output samples  $y_{j-N}$  to  $y_{j-1}$  are multiplied with coefficients  $d_1$  to  $d_N$ . Summing up all these products gives the output sample  $y_j$ :

$$y_j = \sum_{k=0}^M c_k x_{j-k} + \sum_{l=1}^N d_l y_{j-l} \quad (\text{C.4})$$

The frequency response of this filter can be calculated using the z-transform: The z-transform of a signal  $h_n$  is defined as

$$H(z) = \sum_{n=-\infty}^{\infty} h(n) z^{-n}. \quad (\text{C.5})$$

The complex variable  $z$  can be expressed as  $z = r \exp(i\omega)$ . For the special case of  $r = 1$  the z-transform simplifies to the Fourier transform:

$$H(i\omega) = \sum_{n=-\infty}^{\infty} h(n) \exp(-i\omega n). \quad (\text{C.6})$$

The variable  $\omega$  is the normalized frequency where  $\omega = 2\pi$  corresponds to the sampling frequency  $f_s$ .

Time-shifting a sequence  $a_n$  by one sample is equivalent to multiplying the z-transform  $A(z)$  by  $z^{-1}$ : Given that  $b_n = a_{n-1}$  is the time shifted version of  $a_n$  the corresponding z-transform

$B(z)$  is obtained from  $A(z)$  by

$$\begin{aligned}
 B(z) &= \sum_{n=-\infty}^{\infty} b_n z^{-n} = \sum_{n=-\infty}^{\infty} a_{n-1} z^{-n} \\
 &= \sum_{m=-\infty}^{\infty} a_m z^{-(m+1)} \quad (m = n - 1) \\
 &= \sum_{m=-\infty}^{\infty} a_m z^{-m} z^{-1} \\
 &= A(z) z^{-1}
 \end{aligned} \tag{C.7}$$

The z transform of equation C.4 is

$$\begin{aligned}
 Y(z) &= c_0 X_j(z) + c_1 X_{j-1}(z) + \dots + c_M X_{j-M}(z) + \\
 &\quad d_1 Y_{j-1}(z) + d_2 Y_{j-2}(z) + \dots + d_N Y_{j-N}(z)
 \end{aligned} \tag{C.8}$$

Using the time shift properties of the z-transform given in equation C.7 this can be converted to

$$Y(z) = X(z) \sum_{k=0}^M c_k z^{-k} + Y(z) \sum_{l=1}^N d_l z^{-l}. \tag{C.9}$$

The z-domain transfer function  $H(z) = \frac{Y(z)}{X(z)}$  is

$$H(z) = \frac{Y(z)}{X(z)} = \frac{\sum_{k=0}^M c_k z^{-k}}{1 - \sum_{l=1}^N d_l z^{-l}}. \tag{C.10}$$

Substituting  $z = \exp(i\omega)$  gives the frequency response

$$H(i\omega) = \frac{Y(i\omega)}{X(i\omega)} = \frac{\sum_{k=0}^M c_k \exp(-i\omega k)}{1 - \sum_{l=1}^N d_l \exp(-i\omega l)}. \tag{C.11}$$

Compared to the frequency domain approach the time domain method has the advantage that it is suitable for real time applications. For every additional input sample  $x_i$  that becomes available a new output sample  $y_i$  can be calculated immediately. The computational effort for time domain filtering grows linearly with the number  $n$  of samples fed into the algorithm ( $O(n)$ ) compared to  $O(n \log(n))$  for the frequency domain filter.

Digital time domain filter are categorized into two groups: finite impulse response (FIR) filters and infinite impulse response (IIR) filters.

### C.2.1. Finite Impulse Response (FIR) Filter

Finite impulse response filters are a special case of equation C.4 where no past output samples are used to calculate the current filter output and thus all  $d_j$  coefficients are equal to zero. This simplifies equation C.4 to

$$y_j = \sum_{k=0}^M c_k x_{j-k} \quad (\text{C.12})$$

and gives a frequency response of

$$H(i\omega) = \sum_{k=0}^M c_k \exp(-i\omega k). \quad (\text{C.13})$$

As only input samples  $x_j$  are used to calculate the output of the filter, the  $y_j$  samples are zero  $M$  samples after the input time series has decayed to zero. This fact guarantees the stability of the filter and is the reason for the name finite impulse response (FIR) filter.

In order to apply the filter to the data, the  $c_k$  coefficients need to be obtained for the desired transfer function  $H$ . The right side of expression C.12 is a Fourier transform of the transfer function  $H(i\omega)$  which can easily be inverted. Most methods to obtain the  $c_k$  coefficients from the transfer function  $H(i\omega)$  are based on this inversion [46].

### C.2.2. Infinite Impulse Response (IIR) Filter

Equation C.4 with at least one  $d_l \neq 0$  is called an infinite impulse response (IIR) filter. As past output samples  $y_{j-l}$  are used to calculate the current output sample  $y_j$  the output can remain non-zero for an infinitely long time after the input time  $x_j$  series has decayed to zero. In contrast to FIR filters the design of IIR filters has to take stability considerations into account. Badly designed IIR filters can be unstable giving exponentially growing output even after the input series has decayed to zero. Still, IIR filters are preferred over FIR filters for most applications because of their efficiency: Approximating a given transfer function with an IIR filter requires a much smaller number of coefficients compared to an FIR filter.

There is a number of methods available for obtaining the set of coefficients  $c_k$  and  $d_l$  for an IIR filter. One of the most popular methods is the bilinear transform [44] that converts an analog filter to a digital representation.

An analog filter is usually given by the transfer function  $H_a(s)$  where  $s = iu = i2\pi f$ .

$$H_a(s) = A_0 \frac{\prod_f (s - z_f)}{\prod_g (s - p_g)} \quad H_a(iu) = A_0 \frac{\prod_f (iu - z_f)}{\prod_g (iu - p_g)} \quad (\text{C.14})$$



The goal of the bilinear transform is to convert the analog filter function  $H_a(s)$  into a digital transfer function  $H_d(z)$  with a similar frequency dependence. From  $H_d(z)$  the coefficients  $c_k$  and  $d_l$  can be read off by comparing it to equation C.10.

The bilinear transform converts  $H_a(s)$  to  $H_d(z)$  by substituting

$$s = 2 \frac{z - 1}{z + 1}. \quad (\text{C.15})$$

This transformation maps the positive frequency axis of the analog filter  $u = (0, \infty)$  to the finite frequency interval  $\omega = (0, \pi)$  of the digital filter. This transformation is not linear, but it is possible to match one frequency  $u_0$  of the analog filter with a frequency  $\omega_0$  of the digital filter by employing a technique called prewarping [40]. Using the following expression for the bilinear transform the frequency responses of the analog filter at  $u_0$  matches the normalized frequency of the digital filter at  $\omega_0$ :

$$s = \frac{u_0}{\tan(\omega_0/2)} \frac{z - 1}{z + 1} \quad (\text{C.16})$$

The GEO 600 DAQS uses 6-pole Butterworth filters to low-pass filter the data stream before the data are decimated. The design process of such a filter is described below.

An  $n^{\text{th}}$  order Butterworth filter with a cutoff frequency of  $u = 1$  has  $n$  poles spaced around the unit circle. The location of the  $k^{\text{th}}$  pole is given by

$$p_k = -\cos\left(\frac{2k\pi}{2n}\right) + i \sin\left(\frac{2k\pi}{2n}\right) \quad (\text{C.17})$$

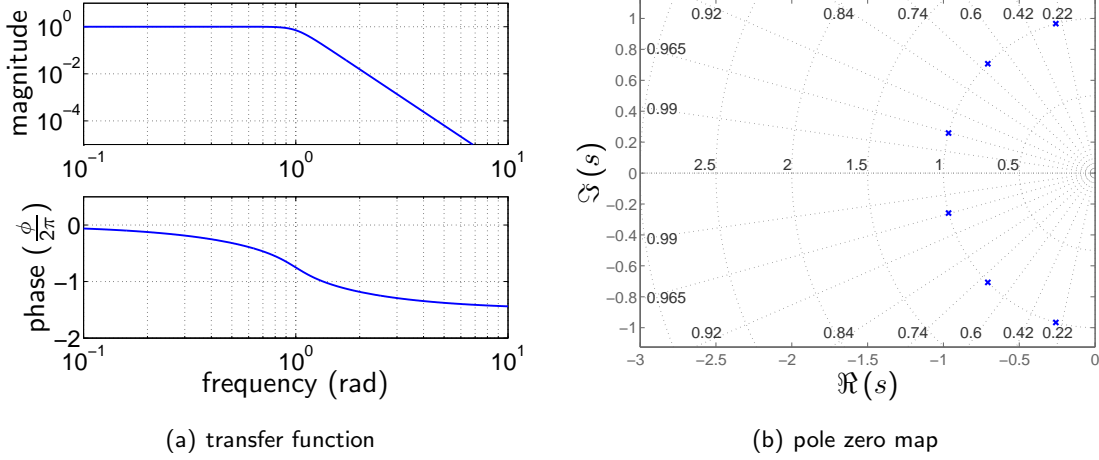
$$\left(k = -\frac{n-1}{2}, -\frac{n-1}{2} + 1, \dots, \frac{n-1}{2} - 1, \frac{n-1}{2}\right)$$

The transfer function is

$$H_{BW}(s) = \frac{1}{\prod_{k=-n/2+1}^{n/2} \left(s - \left(-\cos\left(\frac{2k\pi}{2n}\right) + i \sin\left(\frac{2k\pi}{2n}\right)\right)\right)} \quad (\text{C.18})$$

A plot of the resulting transfer function and a pole-zero-map showing the location of the poles can be seen in figure C.1.

A 6<sup>th</sup> order Butterworth anti-aliasing filter for processing the data before they are decimated from 16 384 Hz to 8192 Hz is designed in the following way. The cutoff frequency of the analog Butterworth filter at  $u = 1$  should be mapped to the desired cutoff frequency for the analog filter which is  $0.3 \times 8192$  Hz at a sampling frequency of 16 384 Hz. This gives a normalized cutoff frequency of  $\omega_0 = 0.3 \times 8192 \text{ Hz} / 16384 \text{ Hz} = 0.15$ .


 Figure C.1.: 6<sup>th</sup> order Butterworth filter with cutoff frequency of  $\omega = 1$ .

$c_0$	$c_1$	$c_2$	$c_3$	$c_4$	$c_5$	$c_6$
0.0026	0.0155	0.0388	0.0517	0.0388	0.0155	0.0026
	$d_1$	$d_2$	$d_3$	$d_4$	$d_5$	$d_6$
	-2.3797	2.9104	-2.0551	0.8779	-0.2099	0.0218

 Table C.1.: Coefficients for 6<sup>th</sup> Butterworth filter used in GEO 600 DAQS for anti-aliasing low pass filtering.

With  $u_0 = 1$  and  $\omega_0 = 0.15$  the bilinear transform C.16 is

$$s = \frac{1}{\tan(0.15/2)} \frac{z-1}{z+1} \approx 13.308 \frac{z-1}{z+1}. \quad (\text{C.19})$$

Substituting this into the transfer function of the analog filter (equation C.18) and converting the result into a quotient of two polynomials in  $z^{-1}$  gives the desired form of equation C.10 so that the  $c$  and  $d$  coefficients can be read off:

$$H(z) = \frac{0.0026 + 0.0155z^{-1} + 0.0388z^{-2} + 0.0517z^{-3} + 0.0388z^{-4} + 0.0155z^{-5} + 0.0026z^{-6}}{1.0000 - 2.3797z^{-1} + 2.9104z^{-2} - 2.0551z^{-3} + 0.8779z^{-4} - 0.2099z^{-5} + 0.0218z^{-6}} \quad (\text{C.20})$$

The obtained coefficients are listed in table C.1.

Figure C.2 shows a comparison between the analog filter and the digital filter obtained using the bilinear transform. Both amplitude and phase show a good agreement.

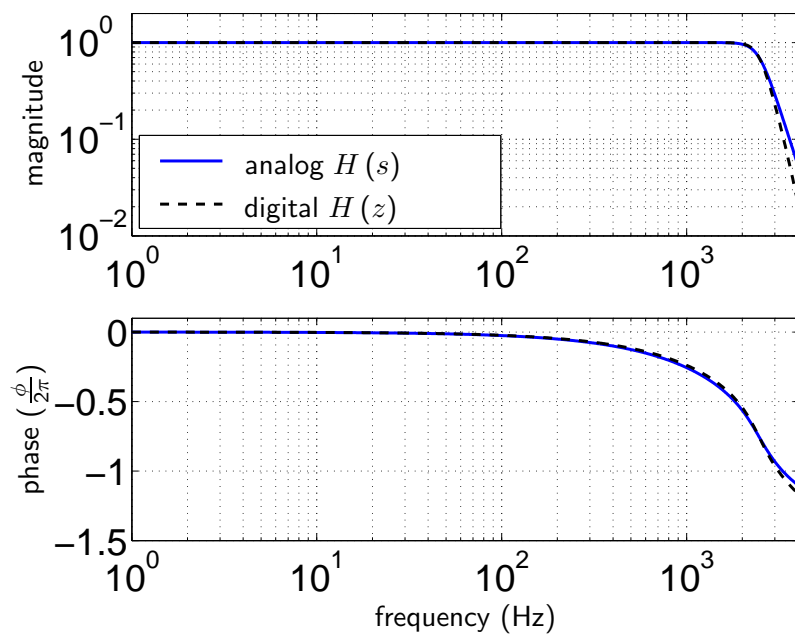


Figure C.2.: Comparison between the analog Butterworth filter and the digital one obtained by applying the bilinear transform.



## Appendix D.

### Active vibration-isolation

GEO 600 employs an active vibration-isolation system to reduce the motion of the suspended optical components which eases lock acquisition and reduces the required actuator forces to keep the interferometer in the locked state.

The active vibration-isolation system is a feedforward control system that measures the horizontal seismic motion of the ground and counteracts the disturbances by moving a piezo actuator that is installed in the support structure of the optical components. A schematic of the control system can be seen in figure D.1.

The sensor used in the setup is a commercial geophone [35] manufactured by the company *MARK* [69]. The output signal is generated by a coil and a magnet. The magnet is rigidly connected to the housing while the coil located around the magnet is connected by a mechanical spring. Any acceleration acting on the housing will lead to a relative motion of the coil and the magnet. This motion induces a voltage in the coil which is the output signal of the sensor. A schematic of the device can be seen in figure D.3.

The signal for the geophone is amplified and fed into a digital signal processor (DSP) to apply the control filter. A *Digisonix* board based on the TMS320C40 processor is used in the setup. The DSP is programmed to implement a transfer function with the parameters given in table D.1.

As actuators piezo elements manufactured by the company *marco* [75] are employed. They have three axes so that the top of the actuator can be moved in all three dimensions by up to 25  $\mu\text{m}$ . To achieve the large dynamic range a special configuration of the piezo elements inside the actuator is used. This can be seen in figure D.4. By elongating and respectively contracting two adjacent piezo elements a sideways movement can be generated that has a larger dynamic range than an individual piezo element.

The setup of the components of the active vibration-isolation system is shown in figure D.5. A set of geophones for the two horizontal axes is attached to the ground next to the tank. After the signal is passed through the DSP it is amplified and fed to the piezo actuators. The structure that is used for suspending the optics is supported by three legs that are called stacks. Each stack contains a piezo actuator that is moved in common mode to displace the suspension point of the optics. Since the actuators contain components which are not ultra-high vacuum compatible, they need to be sealed from the vacuum inside the tank. Metal bellows around the interior of the stacks prevent that outgassing of the stack components

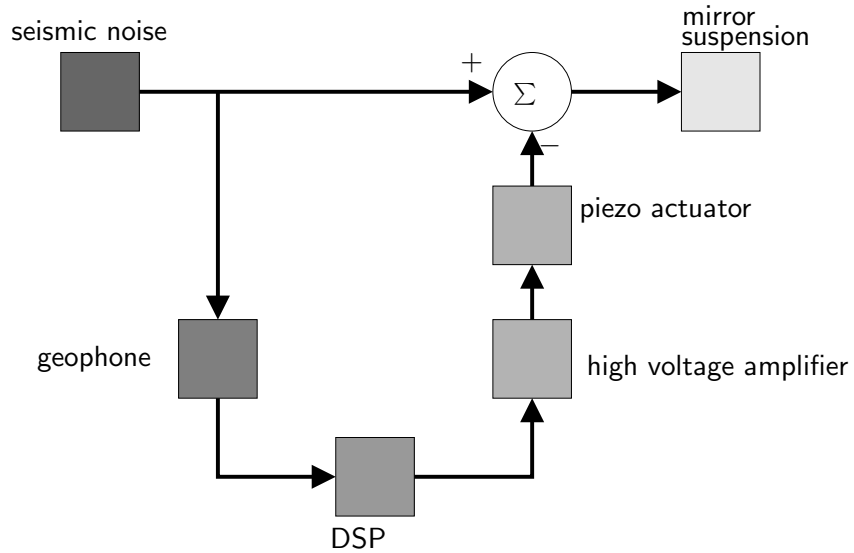


Figure D.1.: Schematic of the feedforward control system.

real poles	real zeros
f=-.17 Hz	f=-4.6 Hz
f=-.17 Hz	f=-2.779 Hz
f=-.17 Hz	-
f=-40 Hz	-
complex poles	complex zeros
f=-.01 Hz, Q=0.7071	f=-1.038 Hz, Q=0.6856
-	f=-.0001 Hz, Q=0.7071

Table D.1.: Poles and zeros of the transfer function used for the feedforward system.

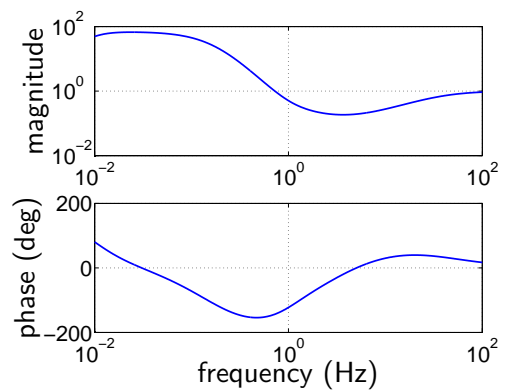


Figure D.2.: Plot of transfer function.

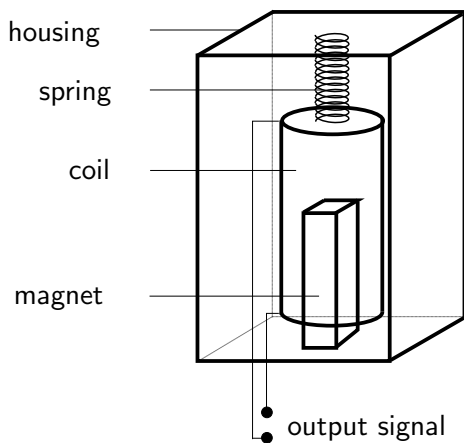


Figure D.3.: Schematic of the *MARK* geophone sensor used to measure the seismic motion.

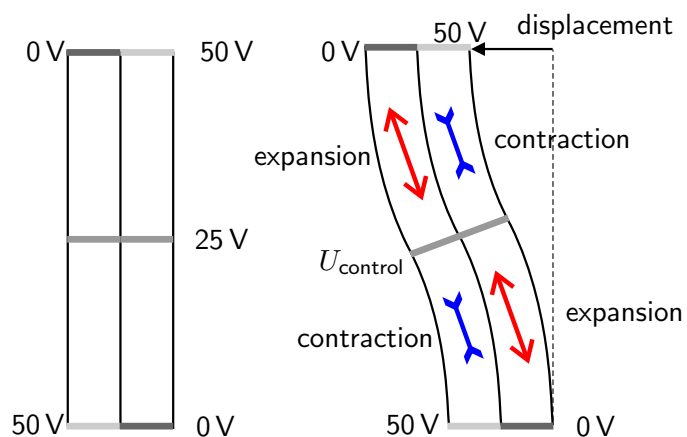


Figure D.4.: Schematic of the piezo actuator employed for the active vibration-isolation system.

contaminates the ultra-high vacuum in the tank. The volume inside the stacks is pumped down to a rough vacuum in the  $10^{-2}$  mbar range so that the pressure difference between the inside of the stack and the surrounding high vacuum of the tank is negligible.

Figure D shows the noise suppression that was obtained using the system described above. The measurements were done on the TFN tank which is located in the north end station. The data were recorded from geophones installed on top of the piezo actuator. By measuring the noise on the floor and on top of the piezo the transfer function of the active vibration-isolation system can be obtained. It can be seen that the seismic noise was suppressed in the frequency range from 1 Hz to 10 Hz. The maximum performance was obtained around 4 Hz with a noise reduction of about 20 dB.

Problems with excess tilt motion of the interferometer mirrors made it necessary to upgrade the active vibration-isolation system recently. The monolithic suspensions showed a stronger conversion from longitudinal mirror motion into tilt than it was expected. The excess low-frequency tilt motion prevented reliable lock acquisition and operation of the interferometer in the dual recycling configuration. Therefore a reduction of the seismic noise in the frequency band from 0.1 Hz to 1 Hz was required to reduce the longitudinal motion of the mirrors. The active vibration-isolation system is now using seismometers manufactured by *Streckeisen* and a DSP system from *dSPACE* [73]. The sensors from *MARK* did not provide a sufficient signal to noise ratio in the required frequency range so that they needed to be replaced with the ones from *Streckeisen* that have a superior performance at low frequencies.

The upgraded system was successfully tested recently and it allows reliable operation of the interferometer over long periods.

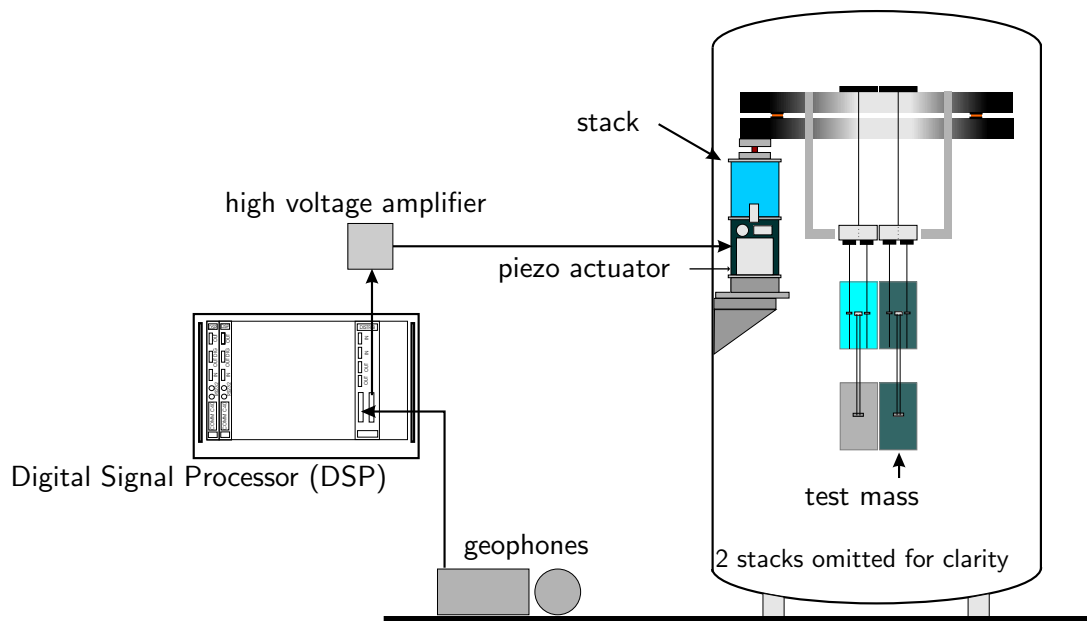


Figure D.5.: Setup of the active vibration-isolation system. A set of geophones measures the horizontal motion of the ground and sends the signal to a DSP where a control filter is applied. The amplified signal is fed to a PZT actuator which cancels part of the seismic excitation acting on the stack.

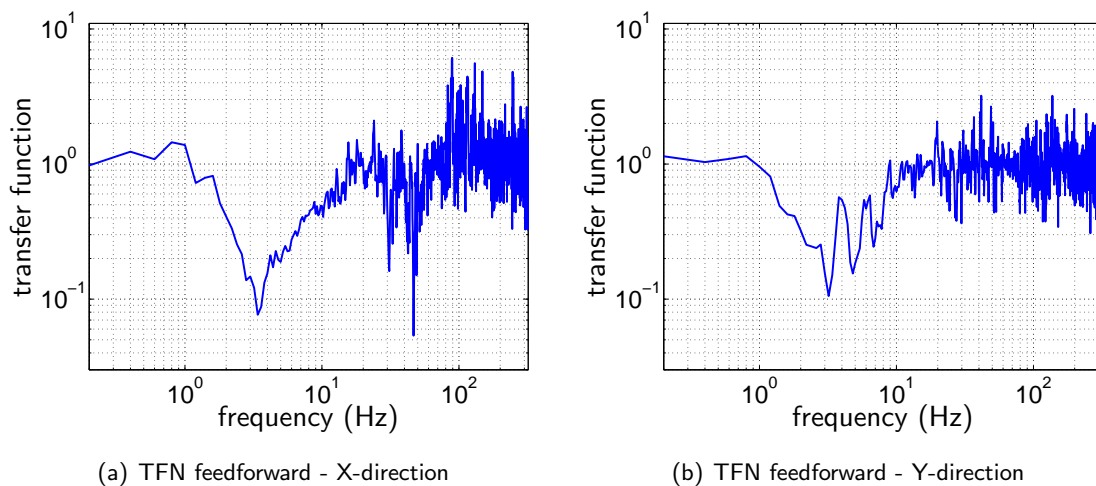


Figure D.6.: Results obtained with the feedforward active vibration-isolation system.



# Bibliography

- [1] Abbott B *et al* 2003 Setting Upper Limits on the Strength of Periodic Gravitational Waves Using the First Science Data from the GEO600 and LIGO Detectors [*in preparation*] 47
- [2] Abbott B *et al* 2003 Analysis of LIGO Data for Gravitational Waves from Binary Neutron Stars [*in preparation*] 47
- [3] Abbott B *et al* 2003 First upper limits on gravitational wave bursts from LIGO [*in preparation*] 47
- [4] Abbott B *et al* 2003 Analysis of First LIGO Science Data for Stochastic Gravitational Waves [*in preparation*] 47
- [5] Abbott B *et al* 2003 Detector Description and Performance for the First Coincidence Observations Between LIGO and GEO gr-qc/0308043 47
- [6] Abramovici A *et al* 1992 LIGO - The laser interferometric gravitational-wave observatory *Science* **256** 325 2
- [7] Allen B 2003 private communication 19
- [8] Anderson W G *et al* 2001 An excess power statistic for detection of burst sources of gravitational radiation *Phys. Rev. D* **63** 042003 59
- [9] Ando M *et al* 2002 Current status of TAMA *Class. Quantum Grav.* **19** 1409–19. 2
- [10] Astone P *et al* 1993 Long-term operation of the Rome “Explorer” cryogenic gravitational wave detector *Phys. Rev. D* **47** 362 1
- [11] Astone P *et al* 1997 The gravitational wave detector NAUTILUS operating at  $T = 0.1$  K *Astroparticle Physics* **7** 231 1
- [12] Astone P *et al* 2003 Methods and results of the IGEC search for burst gravitational waves in the years 1997-2000 *Phys. Rev. D* **68** 022001 15
- [13] Barr B W *et al* 2002 Silica Research in Glasgow *Class. Quantum Grav.* **19** 1655–1662 10
- [14] Bradaschia C *et al* 1990 The VIRGO Project: A wide band antenna for gravitational wave detection *Nucl. Instrum. Methods A* **289** 518–25 2
- [15] Brozek O S 1999 *Frequenzstabilisierung eines Nd:YAG-Hochleistungs-Laser-Systems für den Gravitationswellendetektor GEO 600* (Ph.D. Thesis, University of Hannover) 9

- [16] Casey M M *et al* 2000 Computer monitoring and control of the GEO 600 gravitational wave detector *Rev. Sci. Instrum.* **71** 3910 10, 20
- [17] Cerdonio M *et al* 1997 The Ultracryogenic Gravitational Wave Detector AURIGA *Class. Quantum Grav.* **14** 1491 1
- [18] Cutler C and Thorne K 2002 An Overview of Gravitational-Wave Sources gr-qc/0204090 5
- [19] Danzmann K *et al* 1994 *First Edoardo Amaldi Conference on Gravitational Wave Experiments* (World Scientific, Singapore) p 100–111 2, 8
- [20] Danzmann K *et al* 1994 *GEO 600 – Proposal for a 600m laser-interferometric gravitational wave antenna* (MPQ Garching) 2
- [21] Di Fiore L *et al* 2002 The present status of the VIRGO Central Interferometer *Class. Quantum Grav.* **19** 1421–28. 2, 8
- [22] Drever R W P *et al* 1983 Laser Phase and Frequency Stabilization Using an Optical Resonator *Appl. Phys.* **B 31** 97–105 9
- [23] Freise A *et al* 2000 Demonstration of detuned dual recycling at the Garching 30 m laser interferometer *Phys. Lett.* **A 277** 135–42. 8
- [24] Freise A 2003 *The Next Generation of Interferometry: Multi-Frequency Optical Modelling, Control Concepts and Implementations* (Ph.D. Thesis, University of Hannover) 10
- [25] Goßler S *et al* 2002 The modecleaner system and suspension aspects of GEO 600 *Class. Quantum Grav.* **19** 1835–42. 9, 10
- [26] Goßler S *et al* 2003 Mode-cleaning and injection optics of the gravitational-wave detector GEO 600 *Rev. Sci. Instrum.* **74** 3787 9
- [27] Goßler S *et al* 2003 Damping and tuning of the fiber violin modes in monolithic silica suspension *Class. Quantum Grav.* [in press] 10
- [28] Goßler S 2004 *The GEO 600 suspension systems*, (Ph.D. Thesis, University of Hannover) 10
- [29] Grote H *et al* 2002 The automatic alignment system of GEO 600 *Class. Quantum Grav.* **19** 1849–55 10
- [30] Heinzl G *et al* 1998 Experimental Demonstration of a Suspended Dual Recycling Interferometer for Gravitational Wave Detection *Phys. Rev. Lett.* **81** 5493–6. 8
- [31] Heinzl G 1999 *Advanced optical techniques for laser-interferometric gravitational-wave detectors*, Ph.D. Thesis, University of Hannover, 1999. 8, 89
- [32] Heinzl G *et al* 2002 Dual recycling for GEO 600 *Class. Quantum Grav.* **19** 1547–53 8
- [33] Hewitson M *et al* 2003 Calibration of GEO 600 for the S1 science run *Class. Quantum Grav.* **20** S885–S893 29, 48, 62

- 
- [34] Hewitson M *et al* 2002 A report on the status of the GEO 600 gravitational wave detector *Class. Quantum Grav.* **20** S581–S591 2, 8
- [35] Kötter K 1999 *Aktive seismische Isolation eines Experiments zum Standardquantenlimit der Interferometrie* (Diploma Thesis, University of Hannover) 83
- [36] Kötter K *et al* 2002 Data acquisition and detector characterization of GEO 600 *Class. Quantum Grav.* **19** 1399–407 8
- [37] Kötter K *et al* 2003 PQMon: a powerful veto for burst events *Class. Quantum Grav.* **20** S895–S902
- [38] LIGO Data Group and VIRGO Data Acquisition Group 2000 *Specification of a Common Data Frame Format for Interferometric gravitational wave Detectors* (LIGO-T970130-C-E, VIRGO-SPE-LAP-5400-102) 32
- [39] Heinzl G *Liso: Linear Simulation and optimisation of analog circuits* see Appendix C of [31] 32
- [40] Lyons R G 1997 *Understanding Digital Signal Processing* (Addison Wesley) 79
- [41] Mauceli E *et al* 1997 A search for continuous gravitational waves using the Allegro detector 1997APS..APR.C1103M 1
- [42] Misner C W 1973 *Gravitation* (W. H. Freeman and Company, New York) 3
- [43] Nelder J A, Mead R 1965 A Simplex Method for Function Minimization *Comput. J.* **7** 308–13 55
- [44] Parks T W and Burrus C S 1987 *Digital Filter Design* (John Wiley & Sons) 78
- [45] Plissi M V *et al* 2000 GEO 600 triple pendulum suspension system: Seismic isolation and control *Rev. Sci. Instrum.* **71** 2539 10
- [46] Press W H *et al* 1995 *Numerical Recipes in C* (Cambridge University Press) 78
- [47] Quetschke V 2003 *Korrelationen von Rauschquellen bei Nd:YAG Lasersystemen* (Ph.D. Thesis, University of Hannover) 9
- [48] Saulson P R 1994 *Fundamentals of Interferometric Gravitational Wave Detectors* (World Scientific, Singapore) 3, 4
- [49] Seifert F 2002 *Entwicklung einer quantenrauschbegrenzten Leistungsstabilisierung für ein Präzisionslasersystem* (Diploma Thesis, University of Hannover) 9
- [50] Siegman A E 1986 *Lasers* (University Science Books, Mill Valley) 9
- [51] Sigg D *et al* 2002 Commissioning of the LIGO detectors *Class. Quantum Grav.* **19** 1429–35 2, 8
- [52] Stief F 2000 *Environmental Monitoring am Gravitationswellendetektor GEO 600* (Diploma Thesis, University of Hannover) 8

- [53] Sylvestre J 2002 Time-frequency detection algorithm for gravitational wave bursts *Phys. Rev. D* **66** 102004 59
- [54] Tsubono K 1995 *Gravitational Wave Experiments* Proceedings of the E. Amaldi Conference, edited by E. Coccia, G. Pizzella, and F. Ronga (World Scientific, Singapore, 1995), p 112
- [55] Veitch P J *et al* 1993 Active control of a balanced two-stage pendulum vibration isolation system and its application to laser interferometric gravity wave detectors *Rev. Sci. Instrum.* **64** 1330 10
- [56] Weisberg J M and Taylor J H 1984 Observations of Post-Newtonian Timing Effects in the Binary Pulsar PSR 1913+16 *Phys. Rev. Lett.* **52** 1348–50 1
- [57] Willke B *et al* 2000 Frequency stabilisation of a monolithic Nd:YAG ring laser by controlling the power of the laser-diode pump source *Opt. Lett.* **25** 1019–21. 9
- [58] Willke B *et al* 2002 The GEO 600 gravitational wave detector *Class. Quantum Grav.* **19** 1377–87 2, 8
  
- [59] Artesyn Webpage <http://www.artesyn.com/> 25
- [60] Brandywine Communications Webpage <http://www.brandywinecomm.com/> 25
- [61] Cirrus Logic Webpage <http://www.cirrus.com/> 24
- [62] DCF77 Webpage <http://www.dcf77.de/> 37
- [63] FFTW Webpage <http://www.fftw.org/> 75
- [64] FrameLibrary Webpage <http://www.lapp.in2p3.fr/virgo/FrameL/> 20, 32
- [65] GEO++ Webpage <http://www.astro.cf.ac.uk/pub/R.Balasubramanian/geo++> 47, 67
- [66] Global Positioning System Webpage <http://tycho.usno.navy.mil/gpsinfo.html> 24
- [67] ICS - Interactive Circuits and Systems Webpage <http://www.ics-ltd.com/> 21
- [68] LSC Webpage <http://www.ligo.org/> 47
- [69] Mark Products Inc., 10 502 Fallstone Rd., Houston, Texas 77 099 83
- [70] National Instruments, LabVIEW Webpage <http://www.ni.com/labview/> 10
- [71] Ptolemy Project Webpage <http://ptolemy.berkeley.edu/> 35
- [72] VMIC Webpage <http://www.vmic.com/> 24
- [73] dSPACE Inc. Webpage <http://www.dspaceinc.com/> 85
- [74] geotools Webpage <http://www.astro.gla.ac.uk/users/hewitson/downloads.html> 35
- [75] marco Systemanalyse und Entwicklung GmbH Webpage <http://www.marco.de/> 83

## Acknowledgments

It is my pleasure to thank all the people that contributed to this work:

First of all I would like to thank Karsten Danzmann for giving me the opportunity to participate in the GEO 600 project.

During my time as a PhD student I enjoyed working with the people at the GEO 600 site: Andreas Freise, Stefan Goßler, Hartmut Grote, Ik Siong Heng, Martin Hewitson, Harald Lück, Michaela Malec, Kasem Mossavi, Josh Smith, Ken Strain, Uta Weiland, Benno Willke and all the others created a unique spirit of teamwork and cooperation that allowed to successfully tackle the numerous problems that emerged in the course of the GEO 600 construction.

I would also like to thank the people from the Garching group: Many times Albrecht Rüdiger, Roland Schilling and Walter Winkler provided valuable information and advice.

The GEO 600 data analysis work was done in conjunction with the people at the the Albert-Einstein-Institut in Golm, the University of Birmingham, the University of Cardiff and the University of Glasgow. R. Balasubramanian, Stas Babak, David Churches and others deserve credit for providing the GEO++ data analysis environment that was used to generate results presented in this work.

Much of the work described in this thesis was done in close collaboration with people from the University of Glasgow. During the development and implementation of the GEO 600 DAQS I enjoyed working with Martin Hewitson. With his high motivation and his exceptional skills he was always a great help. Additional contributions to the work on the DAQS came from David Robertson, Harry Ward and Ken Strain. I would like to thank all those people for supporting my work and for the hospitality during the various periods that I worked in Glasgow.

Special thanks go to Carlo Nicola Collacino, Gerhard Heinzl, Ik Siong Heng, Jan Harms, Martin Hewitson, Michèle Heurs, Michaela Malec, Stefan Goßler, Josh Smith, Uta Weiland and Benno Willke for proof-reading parts of this work and providing many helpful comments and corrections.

I would also like to thank my family for their support.



# Curriculum vitae

Karsten Kötter  
An der Bismarckschule 2  
30173 Hannover

## Personal Details

Date of Birth: 1973-07-19  
Place of Birth: Hannover, Germany  
Nationality: German

## Education

1980-08 to 1984-07:  
*Ernst-Reuter-Schule, Egestorf*

1984-08 to 1986-07:  
Orientierungsstufe *Am Spalterhals, Barsinghausen*

1986-08 to 1993-05:  
*Ganztagsgymnasium Barsinghausen*

1993-05:  
*Abitur, Ganztagsgymnasium Barsinghausen*

1993-10 to 1994-09:  
Wehrdienst (military service), *Lufttransportgeschwader 62, Wunstorf*

1994-10 to 1999-10:  
Diploma Studies in Physics, *Universität Hannover*

1999-10-28:  
Physik-Diplom (Master of Physics), *Universität Hannover*

1999-12 to present  
Doctoral Studies in Physics, *Max-Planck-Institut für Gravitationsphysik  
- Albert-Einstein-Institut Hannover*





# Publications

Kötter K *et al* 2002

*Data acquisition and detector characterization of GEO 600*  
*Class. Quantum Grav.* **19** , 1399–1407

Willke B, . . . , Kötter K, . . . 2002

*The GEO 600 gravitational wave detector*  
*Class. Quantum Grav.* **19** , 1377–1387

Hough J, . . . , Kötter K, . . . 2002

*GEO 600 - Research, progress and prospects* The Ninth Marcel Grossman Meeting on Recent Developments in Theoretical and Experimental General Relativity, Gravitation and Relativistic Field Theories, World Scientific Publishing Co., Singapore 1845–1846, ISBN 981-238-010-8

Woan G, . . . , Kötter K, . . . 2003

*The GEO 600 Gravitational Wave Detector – Pulsar Prospects*  
M. Bailes, D. Nice, S. Thorsett (eds.) Radio Pulsars. ASP Conference Series, Vol. CS-302, 351–355

Goßler S, . . . , Kötter K, . . . 2003

*Mode-cleaning and injection optics of the gravitational wave detector GEO 600*  
*Rev. Sci. Instr.* **74** 3787

Kötter K *et al* 2003

*PQMon: A powerful veto for burst events*  
*Class. Quantum Grav.* **20** S895–S902

Sintes A M, . . . , Kötter K, . . . 2003

*Detector characterization in GEO 600*  
*Class. Quantum Grav.* **20** S731–S739

Hewitson M, . . . , Kötter K, . . . 2003

*A report on the status of the GEO 600 gravitational wave detector*  
*Class. Quantum Grav.* **20** S581–S591

Abbott B, . . . , Kötter K, . . . 2003

*Detector Description and Performance for the First Coincidence Observations between LIGO and GEO*  
gr-qc/0308043

Abbott B, . . . , Kötter K, . . . 2003

*Analysis of LIGO data for gravitational waves from binary neutron stars*  
[in preparation]

Abbott B, . . . , Kötter K, . . . 2003

*First upper limits on gravitational wave bursts from LIGO*  
[in preparation]

Abbott B, . . . , Kötter K, . . . 2003

*Setting upper limits on the strength of periodic gravitational waves using the first science data from the GEO600 and LIGO detectors*  
[in preparation]

Abbott B, . . . , Kötter K, . . . 2003

*Analysis of First LIGO Science Data for Stochastic Gravitational Waves*  
[in preparation]

Köttter K *et al* 2003

*Timing Accuracy of the GEO 600 Data Acquisition System*  
*Class. Quantum Grav.* **21** S493–S500